TÉCNICO LISBOA

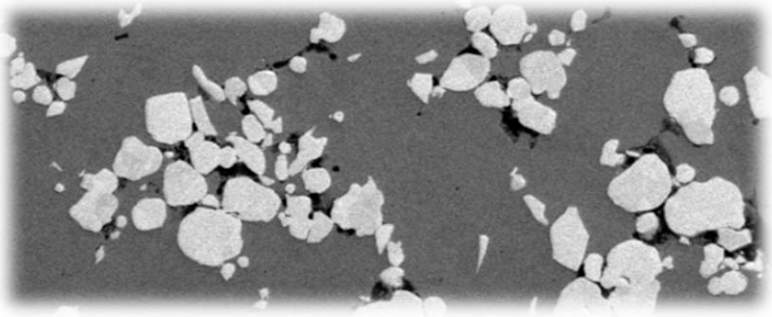

Production, characterization and modelling of WC-Cu cermets

Rita Fonseca Faustino

Thesis to obtain the Master of Science Degree in

Materials Engineering

Supervisors: Doctor Marta Sofia Rosado Silva Dias

Doctor Nuno Rombert Pinhão

Examination Commitee

Chairperson: Professor Pedro Miguel Gomes Abrunhosa Amaral

Supervisor: Doctor Marta Sofia Rosado Silva Dias

Members of the Committee:

Professor Alberto Eduardo Morão Cabral Ferro

Professor Augusto Manuel Moura Moita de Deus

November of 2017

This page was intentionally left blank

Acknowledgments

I would like to thank my supervisor Doctor Marta Dias in the first place, for putting such effort in my education and the continuous support during the entire research time. I thank her also for making me part of her project in IPFN, funded by EUROfusion.Consortium.

I would also like to express my gratitude to my supervisor Doctor Nuno Pinhão, whose guidance through this project has strongly helped to mould my understanding of computational sciences.

To my both supervisors, I would like to thank their willingness to help, that is greatly appreciated as well as their patience and motivation.

I am very thankful to the engineers João Teixeira and Miguel Coelho from DIAPOR– Diamantes de Portugal, S.A, where the materials were processed, to Doctor Umesh Vinaica from IST, who provided the thermal diffusivity data, Doctors Luís Ferreira and Helena Casimiro from CTN, that provided the specific heat measurements, to Doctor Katarina Lorenz and Norberto Catarino for the help with the X-ray diffractometer, Doctor Ana Sofia Ramos from CEMMPRE - UC, for the particles sputtering and Professor Rui Silva for the use of the hardness tester in CENIMAT-FCT. These were essential experimental data for the accomplishment of this work.

I would also like to thank my friends, who accompanied me and offered me a lot of joyful moments.

To my mother, father, sister and close friend Oleksandra, I thank their love, care and dedication, but also the provided means by my parents, that made my academic life easier.

Finally, I thank my boyfriend, Pedro, for the always wise words, love and companionship.

Resumo

Materiais compósitos com matriz de cobre reforçados com carboneto de tungsténio foram estudados para aplicação como camada de transição no diversor de reatores de fusão nuclear. Compósitos com 25, 50 e 75% em volume de WC e o restante em Cu, foram produzidos pelo método de sinterização de prensagem a quente. Três tipos de amostras foram produzidas: (i) mistura de dois tamanhos de partícula de WC (1+18μm, distribuição bimodal), (ii) partículas de WC cobertas com uma camada de Cu pela técnica de *sputtering* (18 μm, distribuição monomodal) e (iii) um sistema multicamada com composição gradual em WC (1 μm, distribuição monomodal). A densidade relativa, difusividade térmica e a dureza foram avaliadas e as microestruturas foram analisadas por microscopia eletrónica de varrimento. Os resultados indicam que compósitos produzidos com partículas de WC revestidas têm maiores difusividades térmicas que aqueles com partículas não revestidas. Além disso o revestimento de Cu reduz a porosidade na área interfacial entre as partículas grandes e a matriz, melhorando a ligação WC/Cu. Todavia, partículas grandes de WC enfraquecem o comportamento mecânico do compósito WC-Cu. Finalmente, modelos de elementos finitos foram usados para analisar o comportamento térmico de um material com as propriedades térmicas do compósito com 75% em volume de WC, com distribuição bimodal. Os efeitos da porosidade e perdas de radiação no comportamento térmico do material foram também analisados. Os resultados mostram que a localização dos poros tem uma influência maior que o tamanho. Ambos os efeitos levam a um decréscimo na difusividade térmica.

Palavras-Chave: compósitos WC-Cu, prensagem a quente, difusividade térmica, efeito de tamanho, modelação

Abstract

Copper-matrix composites reinforced with tungsten carbide have been studied for application as transition layer in the divertor of nuclear fusion reactors. Composites with 25, 50 and 75% by volume of WC and the remain in Cu have been produced by the hot-pressing sintering method. Three types of samples were produced: (i) mixture of two particle sizes of WC (1+18 μm, bimodal distribution), (ii) particles of WC coated with a Cu layer using sputtering technique (18 μm, monomodal distribution) and (iii) a multi-layer system with gradual composition in WC (1 μm, monomodal distribution). The relative density, thermal diffusivity and hardness of the consolidated materials were evaluated, and the microstructures were analysed by scanning electron microscopy. The results indicate that composites produced with coated WC particles have higher thermal diffusivity values than those with uncoated particles. Moreover, the presence of Cu coating reduces porosity in the interfacial area between large particles and matrix, improving WC/Cu bonding. However, large particles of WC weaken the mechanical behaviour of the WC-Cu composite. Finally, finite element models were used to analyse the thermal behaviour of a material with the thermal properties of the composite with 75% by volume of WC, with bimodal distribution. The effects of porosity and radiation losses in the thermal response of the material were also analysed. The results show that the location of the pores has a greater influence than their size. Both effects lead to a decrease in the thermal diffusivity.

Keywords: WC-Cu composites, hot pressing, thermal diffusivity, size effect, modelling

This page was intentionally left blank

Table of Contents

List of Figures

List of Tables

List of acronyms

A	Atomic mass
BDF	Backward differentiation formula
BSE	Backscattered electrons
cermet	Ceramic-metallic
CTE	Coefficient of thermal expansion
OFHC	Oxygen free high conductivity
DBTT	Ductile-to-brittle transition temperature
DC	Direct current
DEMO	Demonstration power station
DT	Deuterium-tritium
EDS	Energy dispersive spectroscopy
EMT	Effective medium theory
FEA	Finite element analysis
FE	Finite elements
FEM	Finite elements method
FGM	Functionally graded materials
HHF	High heat flux
HSM	Heat sink material
HP	Hot pressing
I	Relative intensity
ITER	International tokamak experimental reactor
LFT	Laser flash technique
LI	Liquid infiltration
NIST	National Institute of Standards and Technology
PDE	Partial differential equations
PFC	Plasma facing component
PRMMC	Particle-reinforced metal matrix composites
RT	Room temperature
SE	Secondary electrons
SEM	Scanning electron microscopy
SI	International system
SIF	Solver input file
TT	Time-temperature
vol%	Volume percent
WC	Tungsten carbide
ZAF	Atomic number - absorption -fluorescence

List of symbols

25WC_bi	Composition of 25WC-75Cu in volume percent for the bimodal mixture
50WC_bi	Composition of 50WC-50Cu in volume percent for the bimodal mixture
75WC_bi	Composition of 75WC-25Cu in volume percent for the bimodal mixture
25WC_mono	Composition of 25WC-75Cu in volume percent for the monomodal mixture
50WC_mono	Composition of 50WC-50Cu in volume percent for the monomodal mixture
75WC_mono	Composition of 75WC-25Cu in volume percent for the monomodal mixture
A_c	Contact area
A_s	Surface area
$\mathrm{C_p}$	Heat capacity
c_p	Specific heat
d	Grain size
f	Volume fraction
f_{Co}	Volume fraction of cobalt
f_{WC}	Volume fraction of the WC phase
g	Gravitational acceleration
k	Thermal conductivity
k_A	Thermal conductivity given by the weighted arithmetic mean
k_g	Thermal conductivity of the gas phase
k_H	Thermal conductivity given by the weighted harmonic mean
k_s	Thermal conductivity of the solid phase
L	Sample thickness
Q	Energy of the laser beam
R	Interfacial resistance
r	Radius of the laser beam
r	Radius of the disc specimen
r_c	Capillary radius
r_m	Meniscus radius
t	Time
s	Second
T	Surface tension
T_i	Initial temperature
T_{max}	Maximum temperature
T_m	Melting temperature
T_m^{Cu}	Melting temperature of copper
T_m^{WC}	Melting temperature of tungsten carbide
T_s	Sintering temperature
T_x	Temperature at point x
WC	(higher) tungsten carbide δ-WC

W_2C	(lower) tungsten carbide β-W_2C
$V(L,t)$	Percent rise in the rear face temperature of the disk
α	Thermal diffusivity
ε	Emissivity
ρ	Density
ρ_{cermet}	Density of the cermet
ρ_{Cu}	Density of Cu
ρ_{real}	Real density
ρ_{WC}	Density of WC
θ	Temperature constant
τ	Time constant
ω	Dimensionless time parameter

This page was intentionally left blank

Chapter 1 Introduction

This chapter presents an overview of the context subject as well as the motivation of the present study. Moreover, this chapter also evidences the previous work and the main objectives of the current work. Finally, the outline of this document is presented.

1.1 Context

A fusion power plant demands such extreme and hostile working conditions that the design and selection of materials to withstand them has been addressed as the biggest challenge in materials science in contemporary history [1].

The most promising nuclear fusion reaction is the deuterium-tritium (DT) reaction, in equation (1). When two isotopes of hydrogen fuse, deuterium (${}_1^2H$) and tritium (${}_1^3H$), it releases a helium (${}_2^4He$), the α-particle, and a neutron (${}_0^1n$), along with large amounts of energy. The DT reaction is illustrated in Figure 1.

$$ {}_1^2H + {}_1^3H \rightarrow {}_2^4He + {}_0^1n + 17.6\,Mev \tag{1} $$

Figure 1 Illustration of the DT reaction

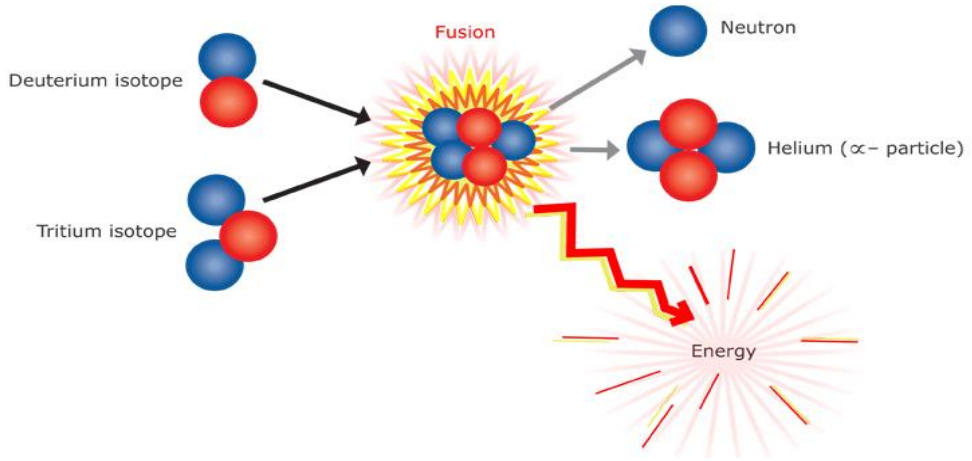

The energetic α-particles will heat the plasma and result in a self-sustained reaction [2]. This phenomenon takes place in a fusion reactor. The international tokamak experimental reactor (ITER) is the fusion device under construction and the DEMOnstration Power Station (DEMO) will be the next fusion station to built. Both of them are *tokamaks.* A tokamak fusion reactor is a doughnut-shaped vacuum chamber, composed of superconducting magnets, vacuum vessel, the blanket, cryostat and the divertor, showed in Figure 2. The magnets produce the magnetic field, responsible to initiate and confine the plasma away from the reactor walls since its temperature is around 100 million degrees Celsius. The plasma circulates in the vacuum vessel, which is surrounded by a giant cryostat, ensuring an ultra-cool, vacuum environment. The cryostat also englobes the magnets. The vessel acts as the primary confinement barrier. The water which

circulates through the walls of the vessel will remove the heat generated during the operation. The blanket and the divertor cover the inner walls of the vessel, respectively the sides and the bottom. The blanket will provide shielding from the high-energy neutrons produced by the fusion reactions. They are slowed in the blanket, decreasing their kinetic energy which is transformed into thermal energy and collected by the water coolant, to produce electric energy. The divertor is situated at the bottom of the vacuum vessel [3]. About 15% of the total generated thermal power and the most of the α-particles produced are extracted by the divertor, that would be harmful to the plasma quality [4].

Figure 2 The main components of a tokamak fusion reactor [3]

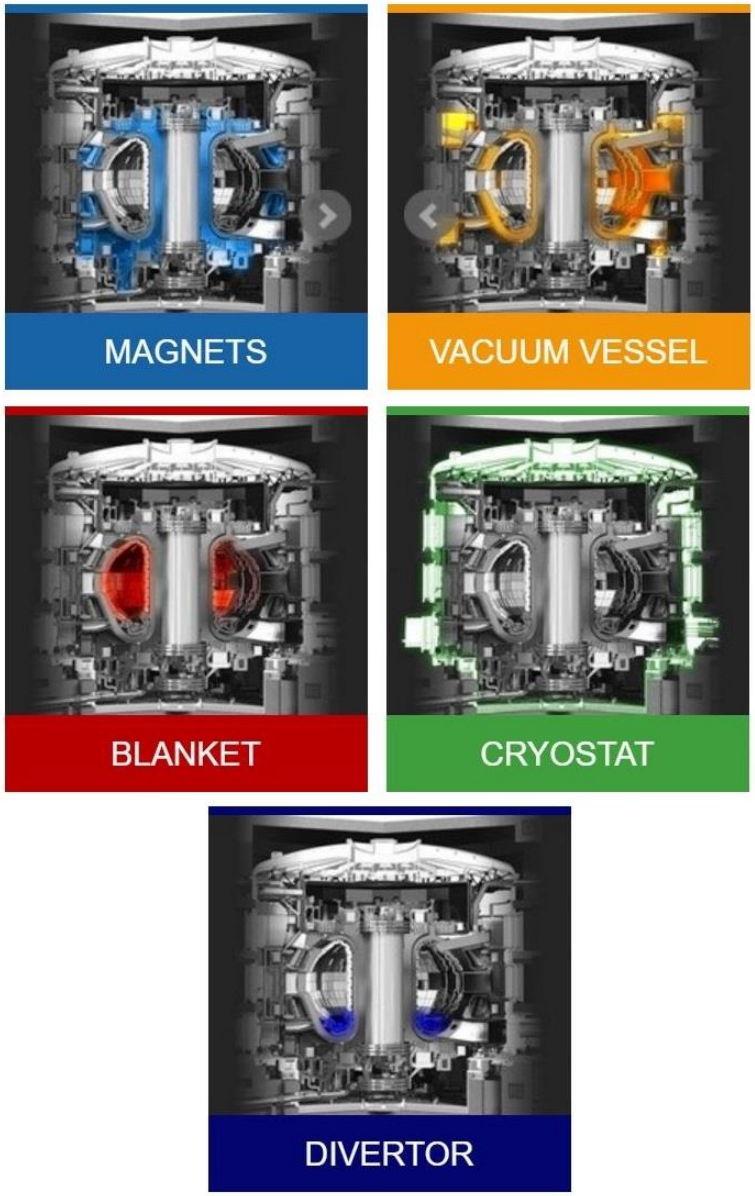

1.2 Addressed issue

The heat generated in fusion reactors will be extracted by the first wall of the blanket and in the divertor. It is intended to perform a heat collection without losses, which requires materials that can withstand very high heat fluxes, without compromising their physical integrity. These are expected to reach up to 20 MW/m^2 for ITER and even larger for DEMO [5].

Tungsten, W, was chosen to be the plasma facing component (PFC) as the armour in ITER and, currently, still is the most suitable candidate as PCF in DEMO. The main reasons are its low or negligible sputtering occurrence [6], to have the higher melting point within metallic materials, a small tritium (T) retention at high temperatures, which is one of the fuels of the DT reaction, and a good thermal conductivity that is not strongly temperature dependent [7, 8]. Also, it has low production rates of transmutation elements, as hydrogen and helium, comparing to others candidates to PFC [9].

Nevertheless, the tungsten application has drawbacks, namely its embrittlement at temperatures lower than 150 to 400ºC [10][11].

There is a heat sink material (HSM) next to the PFC, with the task of draining the heat generated in the W armour. To play this role, a precipitation-hardened CuCrZr alloy is the most promising applicant, due to its high conductivity and ductility, allied to high strength and microstructural stability [5]. It has a high fracture toughness, up to 1.5 dPa, when submitted to irradiation, namely under a fluence of 2×10^{25} neutron.m^{-2} [12]. However, the service temperature of CuCrZr is relatively low, limited to the 150 to 350 ºC interval, due to irradiation creep and thermal softening [13][14].

1.2.1 Motivation

The motivation of this study relies on the existing thermal operation gap between PFC and HSM. In the limit, the W armour must operate above the 400ºC, and the CuCrZr structural compound between 150 and 350ºC. A thermal strain mismatch between PFC and HSM [8][15] is also reported, induced due to the dissimilar values of coefficient of thermal expansion (CTE).

Therefore, an interlayer between the PFC of tungsten tiles and the CuCrZr heat sink is necessary to guarantee a gradual thermal transition, as illustrated in Figure 3 (b). The purpose of the interlayer would be to alleviate the heat flux by diverting it around the tube through the armour [15], in a way that the maximum temperature in the tube is reduced.

For ITER, the chosen interlayer consists of pure soft-annealed copper. However, its high thermal conductivity does not allow a satisfactory temperature gradient generation between the neighbouring layers [16]. Figure 3 shows an illustration of a typical plasma-facing unit of the ITER and DEMO-type divertor target and a corresponding cross-section representation.

Figure 3 (a) Schematic illustration of a typical plasma-facing unit of the ITER and DEMO-type divertor target [15]*; (b) half cross section model(adapted from [8])*

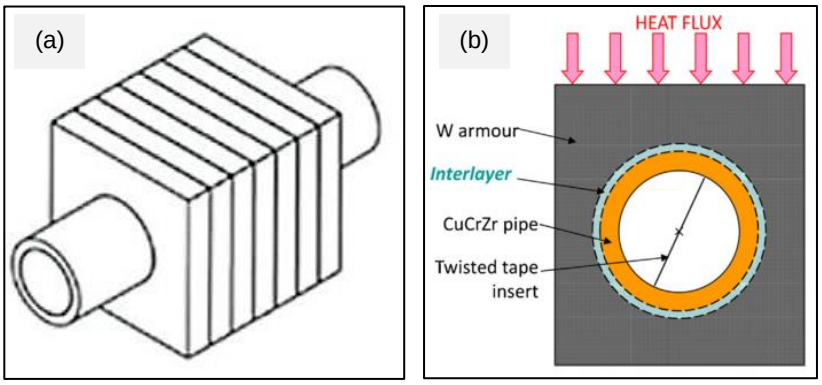

Metal matrix composite (MMC) materials are expected to be an attractive transition material, due to their hybrid characteristics as a composite, by introducing a gentle transition from the brittle behaviour of W to the ductile behaviour of CuCrZr. Particle reinforced metal matrix composites (PRMMC) have been studied in a previous work, namely copper-matrix composites reinforced with tungsten carbide particles.

The aim of the current work is to obtain denser samples of WC-Cu composites and a better mechanical fit. The previous work is presented in the point 1.3 *Previous work* and the objectives of the current work and corresponding approaches to achieve them are indicated in point 1.4 *Objectives.*

There is also motivation to do a computational study of the thermal transport response of this composite since simulation studies allow to achieve a simplified representation of the predictable response of an object or system, which is more expensive and time-consuming. Moreover, it can be done without the user having a deep knowledge of the theory of FEM. FEM presents a wide field of applications, as heat transfer in solids and liquid materials, convection and diffusion of chemical species, elastic deformation of solids, etc, having quite complex geometries and external factors (pressure, forces, radiation losses, etc) that can be applied to the entire body or as boundary conditions [17].

1.3 Previous work

The current work has its foundations on the previous work done by M. Dias *et al.* [18] and F. Guerreiro [19], within the same investigation project, launched in the framework of the EUROfusion Consortium.

A copper matrix composite (Cu grain size of 37 μm) with dispersed ceramic particles of WC (WC grain size of 1 μm) was proposed to perform as the interlayer, between the tungsten armour and the CuCrZr alloy, due to the similar thermal expansion coefficient between tungsten and tungsten carbide, and copper and CuCrZr. Moreover, tungsten carbide detains a lower thermal conductivity, comparing to tungsten, making it a better thermal adapter, as reinforcing phase [19].

The composition, in volume percent, were 25WC-75Cu, 50WC-50Cu and 75WC-25Cu. Its main objective was to optimize the process parameters of sintering, done by hot pressing, to obtain, ideally, no porosity. The chosen compositions and the optimized sintering parameters of the previous work were adopted to produce the current cermets. These are fixed parameters for the current work.

1.4 Objectives

For the current work, WC-Cu cermets are also produced and characterized, but considering new approaches:

- To improve the densification of the WC-Cu cermets, illustrated in Figure 4 (a) and (b), respectively:
  - Bimodal particle size distribution of the reinforcing phase (1+18 μm of WC), to maximize the packing of the latter, assuming that the smaller particles would be accommodated in the free space between the bigger ones [20];
  - Coated particles with a nanolayer of matrix material, to decrease the interfacial thermal resistance between particles-matrix, limiting formation of pores in their interface [21];
- To improve the mechanical matching between W and CuCrZr, illustrated in Figure 4 (d):
  - Functionally graded material (FGM), to improve the mechanical fit, from the most fragile (W) to the ductile one (CuCrZr) [22][13], having three sub-layers with increasing copper content: 25, 50 and 75 volume percent of Cu and the remain of WC.

Figure 4 Schematic illustration of the (a) bimodal particle size distribution and (b) particle coated with a copper layer, (c) interlayer with a unique composition; (d) interlayer with graded composition

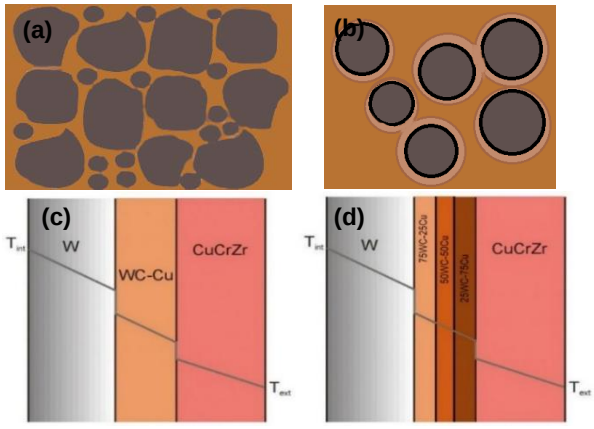

Table 1 summarizes the different features aimed for the cermets.

Table 1 Resume of the used WC particles for each of the seven produced segments and their respective structure

Material composition (%V/V)	WC Grain size distribution	WC Coverage	Segment structure
25WC-75Cu	Monomodal 18 µm	Covered	Unique layer
	Bimodal 1+18 µm	Non-covered	
50WC-50Cu	Monomodal 18 µm	Covered	
	Bimodal 1+18 µm	Non-covered	
75WC-25Cu	Monomodal 18 µm	Covered	
	Bimodal 1+18 µm	Non-covered	
Graded composition	Monomodal 1 µm	Non-covered	Three sub-layers

Finally, finite element (FE) models are generated for transient thermal analysis of the specimens. The aim is to achieve a thermal behaviour that is a perfect representation of the experimental one, given by the laser flash method, in order to have a representative model of the interlayer, to be used in future studies. Next, the effect of porosity on the thermal behaviour is studied by adding pores to the model, with different size and location in the matrix. The effect of radiation losses is also studied, and both imply a decrease in thermal diffusivity, comparing to the model representing the experimental material.

1.5 Outline

The present thesis has two core parts. The first one focuses on the microstructural, thermal and mechanical characterization of WC-Cu cermet materials, along with the effects that result from varying the physical parameters, enunciated in point 1.4 *Objectives*. The second part encloses the development of a model to simulate the thermal behaviour of the WC-Cu cermet and the influence of porosity and radiation losses.

The document is divided into six chapters. Chapter 1 is the current introduction, where the context, the addressed issue and the objectives are described and also the outline of the document is presented. Chapter 2 presents the study of the interaction between the constituents of the composites, a research on common materials proposed for interlayers and their processing techniques, ending with a study of modelled systems of the part of interest - the monoblock of the divertor. In Chapter 3 are presented the experimental and numerical techniques with a brief theoretical framework and the experimental procedure. Results and discussion are presented in chapter 4 for the WC-Cu composites and in chapter 5 for the modelling work. The latter includes the development and validation of the model conditions. In chapter 6, the conclusions derived from the experimental and modelling data are summarized and suggestions for future work are made. In this final chapter, also the challenges faced while doing this study are discussed.

Chapter 2 State of the Art

This chapter evidence the interaction between the constituents of the composites, presents a brief research on the most common materials proposed for interlayers and on particle reinforced copper-matrix composites and their processing techniques. Moreover, modelled systems for the aimed applications are presented.

2.1 WC – Cu system

2.1.1 Tungsten – carbon system

Tungsten and carbon can form two compounds: higher tungsten carbide, δ-WC (WC), and lower tungsten carbide, β-W_2C (W_2C), which have several polymorphic modifications, stable in different temperature and composition ranges. WC has hexagonal structure with a c-a ratio of 0,976, where W and C atoms form simple hexagonal sub-lattices. This transition metal/carbide is the most stable form of carbide in the W-C system, between 300 and 1200 K. W_2C exists in three W_2C polymorphic structures, β-W_2C, β'-W_2C, β''-W_2C, depending on the temperature interval. WC has a unique structural variation. The latter retains the hardness of room temperature (RT) up to 1400°C without any phase change [23].

Figure 5 Phase diagram of the W – C system [23]

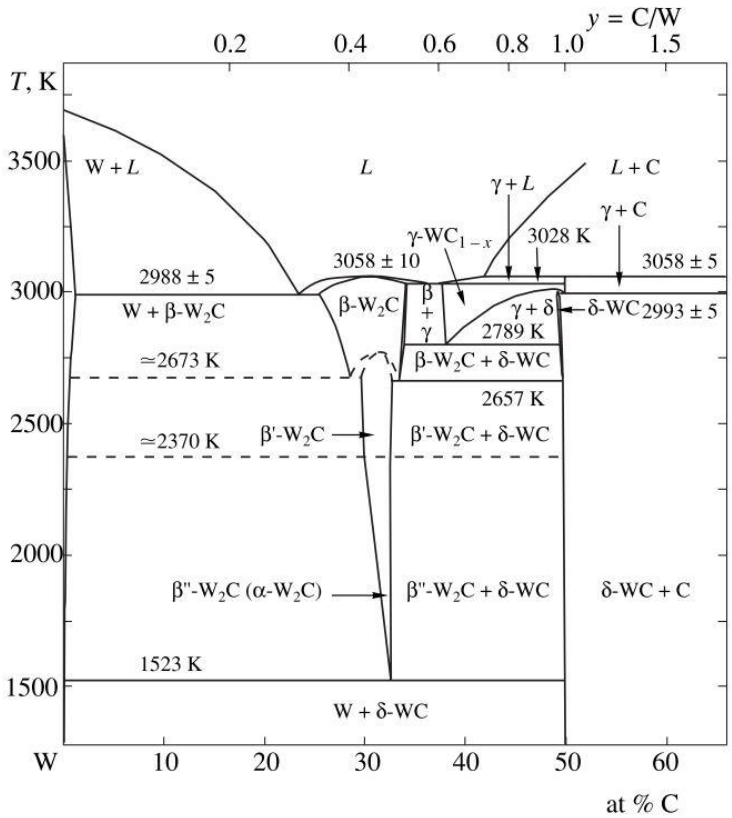

2.1.2 Tungsten - Copper system

The W-Cu equilibrium phase diagram presented in Figure 6, is related to pressures higher than 100 atm, though the W-Cu relation is assumed to be similar at 1 atm. The equilibrium phase diagram shows that W has a very low solubility in Cu which hinders intermetallic compounds formation [24].

Figure 6 Phase diagram of the Cu – W system (adapted from [24]*)*

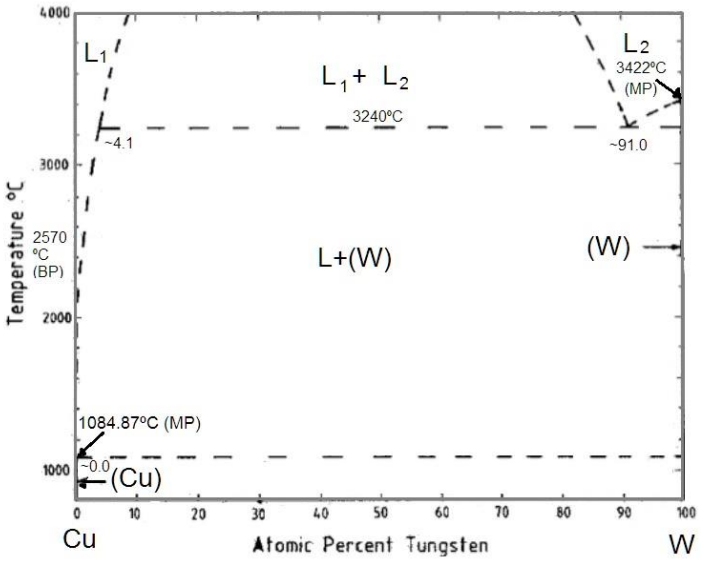

2.1.3 Copper – carbon system

Figure 7 presents the Cu-C equilibrium phase diagram. The solubility of C in solid Cu is very small (maximum of 0.0078 wt.% C before the Cu melting point).

Figure 7 Phase diagram of the Cu – C system (adapted from [25]*)*

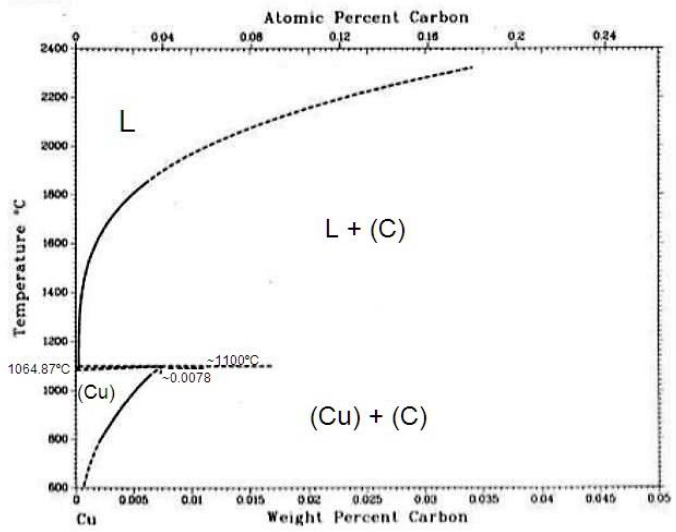

2.1.4 WC - Cu interaction

WC and Cu do not have a relevant solubility in each other, in this way, only physical bonding takes place. This is generated by the formation of a meniscus, when a liquid wet the particle. In the liquid-solid interface, there are intermolecular forces. Hence, an inter-particle capillary force is developed [26]. Therefore, the WC-Cu wetting system is of major importance, since the liquid should instantaneously wet the ceramic particles, as reported by A. Kennedy *et al.* [27]. Otherwise, the consolidation process will be hindered.

A good wetting angle, under 45º, will facilitate a complete infiltration of the metallic liquid phase in the existing voids [28], when the forming elements of the material are submitted to high-temperatures. Some authors studied the WC wettability by copper. Chrysanthou and Erbaccio [29], states a wetting angle of 7º at 1200ºC, Silva *et al.* [30] obtained an angle of 25º and Kennedy *et al.* [27] an angle of 30º, measures took close to 1100ºC. Despite the distant values, they are both under 45º, that should promote good wetting characteristics of the matrix to the reinforcing phase.

The capillary action, which is the magnitude of the standard capillary effect, depends upon the weight of liquid that the surface tension will have to lift, related by equation (2)

$$h = \frac{2\gamma_{LV}\cos\theta}{\rho r_c g} \tag{2}$$

where h is the height to which capillary will take the liquid,γ_{LV} γ_{LV} the surface tension in the liquid-vapor interface that makes a θ angle with the solid surface, ρ the density of the liquid, related with its weight, r the capillary radius and g the gravitational acceleration [31].

In sintering, the capillary effect is resembling. The latter is related to the induced pressure and the mass of the liquid that depends both on the density and the meniscus radius formed between two particles [26].

According to Martins *et al.* [28], when the matrix material is at the liquid state, the relevant properties for the infiltration can be related in the following way

$$\Phi = \frac{r_m\gamma_{LV}\cos\theta}{2\mu} \tag{3}$$

where Φ is considered to be the intrinsic infiltration rate parameter of the liquid/gaseous system, r_m the radius of curvature of the meniscus formed between two particles (equivalent to capillary radius), and μ the viscosity of the liquid. An increasing value of Φ requires less time for infiltration to a given height, and thus is an indication of improved infiltration kinetics [28]. The relevant system properties are therefore γ_{LV}, the radius of the capillary tube, taken to be the same as r_m, and the viscosity of the liquid, μ.

2.2 Proposed materials as interlayer

2.2.1 W-CuCrZr

W-CuCrZr is a commonly study composite for application on fusion reactors as the interlayer of the divertor, since it binds two walls made of the same materials – W and CuCrZr. They are studied as materials with a fixed composition, among 30 to 70 vol.% of W, and also as functionally graded materials (FGM), to allow a gradual mechanical transition.

The composites are typically produced by melt infiltration of the metallic phase with the lower melting temperature (T_m), the copper alloy, into a tungsten skeleton [13, 32] since the components have a low mutual solubility. This step is usually followed by an ageing treatment, for precipitation hardening. This allows the material to be nearly fully dense and have a good mechanical response, with a maximum hardness of 300 HV. The thermal conductivity does not have a relevant dependence on the temperature until 600º C, being close to 200 W/mk, which reveals a stable thermal behaviour. However, when producing FGM, the coefficient of thermal expansion (CTE) exhibits a direct linear dependence on the increasing content of CuCrZr and increasing temperature, which indicates that there will be a strong CTE mismatch, in other words, a strong mechanical misfit [22]. The authors also studied the material response to high heat fluxes (until 15 $MW.m^{-2}$), in a W/W-CuCrZr mock-up, not showing indication of damage in the interlayer.

The reinforcing phase is metallic (W), so the latter provides high values of thermal properties, as thermal conductivity and heat capacity, which might not be desired for a transition layer that should keep the temperatures of the armour of W and the heat sink part of CuCrZr in the corresponding operating windows.

2.2.2 W-Cu

The tungsten–copper (W–Cu) system [26] are also under study for application as interlayer, due to the resemblance of the original components with the neighbouring walls. However, one of the critical drawbacks of a W/Cu is the rapid loss of plastic strength at elevated temperatures associated to the thermal softening of pure Cu, depending on the vol% used of W.

2.2.3 C_D-Cu

Diamond-Cu composites have been also proposed as interlayer [33]. Mock-ups of W/C_D-Cu/CuCrZr and the parts were joined by ultra-precision resistance welding. Analysis by finite element analysis they found that the C_D-Cu interlayer relaxes the stresses from welding interface, avoiding cracks at the welding interface, between W and CuCrZr. However, the thermal conductivity of diamond-Cu composite is expected to increase in a fusion reactor due to the formation of a carbon phase of corrugated graphite-like layers connected by strong diamond-like sp^3 bonds between graphite and diamond, which was found after neutron irradiation of natural diamond.

2.2.4 Nickel coating

Q. Li *et al.* [34] suggested a Ni coating between CuCrZr and the Cu layer, to improve their bonding, employing the oxidation free encapsulation (OFE) technique. OFE technique prevents the oxidation of pure Cu during hot isostatic pressing, which plays a key role in improving the bonding quality of Cu/CuCrZr interface.

2.2.5 Functionally graded materials

Functionally graded materials are composites characterized by a gradual variation in composition and structure over the volume of the material, which results in a gradual change in the material properties. Typically, FGMs are composite materials with a graded microstructure, to better adapt the limiting microstructures from one material to the other, with a specific gradient [35].

Despite the several techniques available to produce FGMs, their final properties may vary according to the chosen consolidation technique. Powder metallurgical processes [36], plasma spraying [6], infiltration techniques [6][32] and laser sintering [6] are the methods used to produce FGMs.

2.3 Particle reinforced copper-matrix composites

Metal matrix composites (MMC) is a class of composite materials where the matrix is a continuous metallic phase, combined with the second phase, that can be solid, called the reinforcement phase, or gaseous, as in the metal foams [37]. Considering the second phase as solid, metallic or ceramic, it can have varied shapes, as continuous fibres, discontinuous fibres and spherical to irregularly shaped particulates. Since the two phases in a composite can have vastly different properties (physical, thermal, electrical and mechanical), the composite properties can vary over a broad range when managing the matrix material and the reinforcement material, volume fraction, morphology and distribution. In general, the best fracture properties are achieved for the PRMMC with a volume percentage under 25% combined with a more uniform distribution and finer particulate sizes [38]. In this way, PRMMC with fine reinforcement phase are envisioned for the current work to attain the best and uniform mechanical behaviour.

MMC are indicated for thermal management applications, where a high specific thermal conductivity (thermal conductivity divided by density) are desired.

Copper is a common material chosen as matrix in this family of composites due to its high ductility, thermal and electrical conductivity, high corrosion and oxidation resistance allied to its high melting point and temperature resistance [21].

Copper matrix composites are usually reinforced with alumina and silicon carbide facing tungsten carbide. They all present high hardness and wear resistance, refractory nature, but alumina and silicon carbide detain relevant cost advantage comparing to WC, which is the reason for the less common use of WC as reinforcing phase [39].

The term “cermet” is used to designate MMC with ceramic reinforcement content [40]. In this way, “cermet” will be the term used for the composites produced in the current work, as in “WC-Cu cermet”.

2.3.1 Hardmetals

Hardmetals or cemented carbides are composites that consist of micrometric or smaller sized particles of hard carbides dispersed through a metal binder. The hard carbides can be titanium carbide (TiC), tantalum carbide (TaC) or, the most common, tungsten carbide (WC). The metal matrix is usually cobalt (Co). They present high wear resistance due to this combination of hard ceramics and good fracture toughness of the matrix phase. Hence, hardmetals are extensively used in activities demanding high service temperatures (below 600°C) and wear resistance, as high-speed steel cutting or wire drawing, depending on the binder content. The most common system is WC-Co, due to Co favourable solubility in WC, good wetting behaviour and good mechanical properties [41].

2.3.2 PRMMC with bimodal distribution size of the reinforcing particles

According to Molina et al. [7], a denser material is obtained with two particle size mixtures. They concluded that higher densifications were obtained for a mixture having between 50 and 67% of coarse particles. Also, under a sintering process with a liquid phase present, the capillarity effect is more effective for copper infiltration among finer particles and particles that have acute contact angles [27],[28]. Hence, this feature is thought to be an added value to increase the densification of the present cermets.

2.3.3 PRMMC with coated reinforcing particles

J. Li *et al.* [42] demonstrated that pre-coating diamond particles with a titanium film to be dispersed in a copper matrix improve the interfacial bonding between the particles and the metal matrix, yielding “dramatically” the thermal properties of the composite. The particles were covered by vacuum vapour deposition. Such characteristic could strongly increase the physical bonding between the copper matrix and WC dispersed particles.

In conclusion, copper is a more available material than CuCrZr. In this way, introducing a reinforcement external phase, would improve the mechanical resistance of the pure copper, roughly substituting the function of hardening precipitates in CuCrZr. Also, the addition of a more thermally insulated reinforcing phase than W would more easily adapt the thermal response, to keep the temperatures of both the armour

of W and the heat sink part of CuCrZr in the corresponding operating windows. This could be provided using WC as the reinforcing material.

2.4 Consolidation methods of copper matrix composites

2.4.1 Liquid phase sintering

Liquid-phase sintering (LPS) is a simple process, where the matrix phase melts and involves the reinforcement phase. Systems where elements diffuse between the solid and liquid phases achieve a more dense microstructure since this solubility causes the liquid to wet the solid, providing a capillary force that pulls the grains together [30][43].

LPS of systems such as WC–Cu, in which the solid base ceramic has little solubility in the liquid phase, results in lower densifications (bellow 80 to 90%), unless the WC particles have a submicrometric size [26]. In this way, the production via liquid state sintering is difficult to achieve. On the other hand, the combination of LPS with liquid infiltration (LI) methods [26] lead to nearly fully dense materials. LI vary from LPS in the simple fact of applying a high vacuum in the rear side of the specimen, generating a driving force for the liquid metal to move and fill the porosity with a much higher intensity [44]. Having such equipment available, the LI method would be a promising choice for WC-Cu consolidation.

2.4.2 Activated liquid phase sintering

“Activated” liquid phase sintering was developed by Su and Johnson to obtain a single apparent activation energy for densification of a given ceramic system. Later, this work was further used for the calculation of the apparent activation energy for sintering, densification function, and work of sintering for W–Ni–Fe,W–Ni–Cu, and W–Cu systems [45], to create a master sintering surface for different solubilities of W in the liquid phase. This process makes use of activators, as cobalt or iron, that influence the apparent activation energies for the densification. However, these elements cannot be present for the aimed application, since their interaction with the plasma in the divertor has not been studied or is not viable.

2.4.3 In situ processing

Chrysanthou [29] studied WC-Cu cermets processed *in situ*. Here, W was lead to react with carbon black forming WC after W_2C, injecting the ceramic particles in a molten copper medium. The particles did not fully react, in a way that some portion of W_2C cores is still present in the system, enclosed by WC phase. W_2C can assume three polymorphic structures that might induce mechanical stresses due to the difference in crystal packing, if the service temperature has maximum peaks higher than 1500 ºC.

2.4.4 Hot pressing

In hot pressing (HP) the raw powders are sintered at a temperature lower than the T_m of all the composing elements. HP is not a commonly adopted process to sinter WC-Cu cermets. However, HP is economically more viable than the competitor processes stated above [46] and is commonly used in an industrial scale, which is a determinant factor for the current project.

2.5 Previous work

The production by of WC-Cu cermets have been proposed in the previous work by M. Dias *et al.* [18] and F. Guerreiro [19] to perform as interlayer of the divertor.

Copper (Cu) was selected as matrix material, since it has a similar CTE to the one of Cu alloy (17 m.m-1.ºC-1 for Cu and 18,6 m.m-1.ºC-1 for CuCrZr) aimed to be annexed to the latter. WC was selected since it is more thermally insulating than W, and the theoretical CTE of both materials are close (4.3 and 4.3 to 5.9 for W and WC, respectively). In this way, the proposed interlayer materials are expected to maintain the temperatures of the neighbouring parts, armour and heat sink, in their working windows.

In the previous work, WC-Cu cermets were produced by the powder-metallurgy route. HP was the selected process. Composites were produced with three compositions: 25WC-75Cu, 50WC-50Cu and 75WC-25Cu vol.%, where the average size of powders was 1 µm for WC and 37 µm for Cu. Optimized sintering cycles were obtained for each composition, indicated in Chapter 3, Table 5. The optimized sintering cycles correspond to the produced samples with the highest densification, indicated in Table 2.

Table 2 Densifications of the produced WC-Cu cermets in the previous work

Material composition (%V/V)	Densification (%)
25WC-75Cu	91
50WC-50Cu	92
75WC-25Cu	95

The densest sample with 75 vol% of WC content was sintered at 1150ºC, approximately 70º C above the melting temperature of Cu, T_m^{Cu} of 1083 ºC. The Cu matrix melted, which allowed the liquid Cu to infiltrate into the pores, increasing the densification of the material. The densest samples with the composition of 25 and 50 vol% WC were obtained at temperatures lower than T_m^{Cu}, respectively 185 and 20 ºC bellow it. However, for the sample with the highest Cu content, the Cu melted and drained out of the mould, as showed in Figure 8. The Cu melting occurrence indicates that the applied sintering temperature was equal or higher than T_m^{Cu}, resulting in liquid-state sintering instead of solid state sintering.

Figure 8 Sample of composition 25 vol% WC resulting from hot pressing [19]

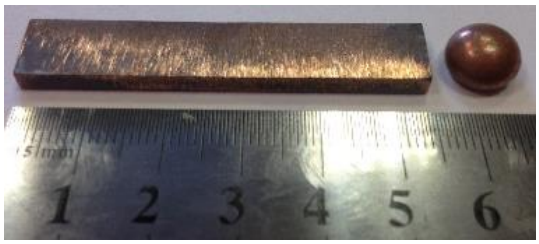

The microstructure analysis confirmed a good adhesion between the matrix and the reinforcement phase, showing the coalescence of WC particles for the compositions with higher WC content (50 and 75 vol%) and the formation of regions rich in Cu, in consequence of short mixing time, for the composition of 25 vol% of WC. Thermal diffusivity (α) data exhibit lower values than the original components, WC and Cu, and the lowest value is for the sample with the highest content in WC. In conclusion, the results indicate that the WC-Cu cermets can be good candidates for transition layer.

2.6 Modelling of thermal behaviour

2.6.1 Modelled systems of the divertor

Several authors simulate the thermal behaviour of the multi-material monoblock of the divertor system used to predict the most fitted geometrical and structural (material selection) parameters [7, 13, 14], to introduce in its composing sections and consequentially determine the structural and geometrical limitations. Figure 9 is a finite element (FE) mesh of the model of the monoblock divertor, indicating the materials and the proportions considered for the monoblock of the divertor of ITER: W as PFC, Cu as interlayer and CuCrZr as HSM [7].

The effect of the W/CuCrZr FGM interlayer on temperature, stress and strain distribution in a W/WCuCrZr and FGM/CuCrZr components, among others, were studied using FEM. The results show that a thicker interlayer leads to a long heat transfer and thus, more heat accumulates at the surface, leading to high

Figure 9 FE mesh o one half of the monoblock divertor model due to symmetry [7]

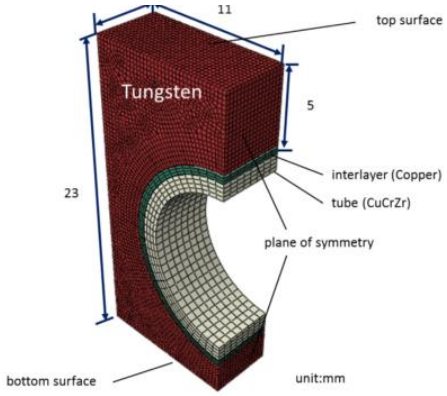

heating of the material at the surface. On the other hand, the studies reveal that the temperature distribution along the heat sink material, CuCrZr, shows no significant difference of the used material as interlayer, Cu [13, 47].

2.6.2 Modelling of methods to obtain thermal transport behaviour

A. Zivelonghi *et al.* [47] generated FEM models of microstructures of heterogeneous materials typically used for fusion applications, W/CuCrZr, through high-resolution SEM 2D images analysed with the open-source software OOF2 [48], created at the National Institute of Standards and Technology (NIST). This technique calculates the thermal (and mechanical) responses of the material through its real microstructure. The latter analyses one micrograph at the time and the varying temperatures within in, for a fixed and known external temperature. The software attributes the respective thermal conductivities to the different identified materials, generating a representative model, and finally α values are obtained for a temperature range of interest.

M Sheikt *et al.* [49] proceeded to the modelling of the laser flash technique, to validate experimental α results, whose theory and governing equations are indicated in point 3.1.5 *Laser flash technique*. Models of the specimens were generated to simulate the laser flash experiments. Only a quarter of the specimen was modelled, due to symmetry. For each specimen, two different mesh gradings were used to study the effect of mesh size on the convergence behaviour of the solutions. In addition, for these problems, the time-step chosen for the analysis is important to obtain a converged solution. The models were generated using FEMGEN, that defines the geometry, material properties, boundary and initial conditions. Finite element solver was ABAQUS. The results of α obtained by modelling are in agreement with the experimental ones.

The work of the latter author and co-workers enhance that obtaining a modelling curve of the laser flash method, that is representative of the thermal behaviour of the WC-Cu material, ensures that the corresponding model would be a representative model of the interlayer. Therefore, it would allow studying the thermal effectiveness of the present material as interlayer, by including it in the model of the divertor monoblock and also study the effect of its thickness in its thermal response.

Chapter 3 Techniques and experimental procedure

This chapter details the techniques (experimental and numerical methods) and the experimental procedures used to obtain samples and data for this dissertation. Firstly, the equipment and methods are described, followed by the experimental procedure. The procedure of developing models and the considered modelling conditions are gathered in Chapter 5 *Modelling.*

3.1 Experimental techniques

The laboratory and industrial equipment and their respective experimental techniques and working conditions are briefly described.

3.1.1 Hot pressing

Hot pressing is a technique of powder metallurgy which combines unidirectional pressure, mechanically applied, and heat application, promoting powder pressing and sintering. This technique originates near-net shape or net shape parts during a single operation, having the advantages of the pressure and heating systems to be independent and that HP is a fast method [46]. Produced samples typically achieve densifications near to 100% in a wide range of materials, for optimized sintering and pre-sintering parameters – added minor elements, milling time, temperature, pressure and holding time [50].

Usually, HP occurs under an inert gas atmosphere, to avoid the powder from being oxidized. The temperature is raised by induction or resistance methods, during compaction at a determined rate, for several steps, heading to a plateau, at the maximum temperature and pressure for a certain holding time of a few minutes. The sintered specimen is then cooled within the same logic, under pressure, till room temperature (RT). The temperature in the camera can be controlled by an infrared pyrometer attached at the surface of the mould [51] or by a thermocouple. The latter is more reliable. Since the applied temperatures can be high, HP does not require very high pressures to achieve the desired consolidation, in a way that the powdered materials will not suffer a great plastic deformation during the sintering process, making the resulting piece more resistant, comparing to RT resembling processes. The pressure applied by a uniaxial press can range from 20 to 50 MPa for a graphite die. The parameters affecting directly the quality of a hot-pressed material are pressure, temperature, time and atmosphere composition. The ability of HP achieving nearly theoretical density strongly depends on the mould aspect ratio H/L, where H is the height and L the length diameter of a cylindrical section of the specimen [1]. Pressing becomes difficult as the value of the ratio H/D increases; for ratios between 1 and 3 can cause problems with die wall friction, ram motion, and pressure distribution which can affect the microstructure homogeneity (density) of the specimen [46].

3.1.2 Direct current magnetron sputtering

Direct current (DC) magnetron sputtering is a thin film physical vapour deposition coating technique. The target is bombarded with ionized gas molecules, which causes the atoms to be *sputtered* off into the plasma. These atoms condense as a thin film on the substrate to be coated. The process is done under an inert atmosphere [52]. Typical sputter pressures range from 0.5 mTorr to 100 mTorr and regarding the DC current, a range of -2 to -5kV is applied. This is applied to the target material, which is the cathode, and a positive charge is applied to the substrate to be coated, the anode. Magnets are placed strategically to trap the electron over the target, so they cannot bombard the substrate, to a higher process efficiency. DC Sputtering is commonly used since DC power is easier to adjust and a continuous film is easy to obtain. This technique allows a continuous coverage of particles if their smaller diameter is of 10 µm, for simple metal deposition for coating [53].

3.1.3 Scanning electron microscopy and energy dispersive spectroscopy

Scanning electron microscopy (SEM) provides information on the surface aspects of the submitted sample, through the surface scanning with an electron beam, which interacts with the specimen's exposed fine layer. The interaction results in the emission of different types of the signal by the specimen, each one responsible for returning different surface information: topographic contrast, particles size and dispersion are obtained with secondary electrons (SE) signal, chemical composition contrast, based on the atomic number of the scanned elements, can be exploited with backscattered electrons (BSE) signal. The latter can be diffracted by the atomic layer in crystalline materials, and form a pattern of the incident crystal structure orientation, by the electron backscatter diffraction (EBSD) technique [54].

Images resulting from SE and BSE have a very good resolution on a scale from a few millimetres to hundreds of nanometres. Some of the disadvantages of SEM is the need of high-vacuum environment, that can damage biological samples and increase the operation time very much when analysing porous materials. Also, the samples need to be conductive to avoid bad signal detection.

Energy dispersive spectroscopy (EDS) is coupled to SEM and is the technique responsible for detecting the emitted X-rays that are characteristic of the elements present in the chosen small areas of the specimen's surface. The latter is used to determine the elemental composition of individually specified points of the different material's phases. The X-rays are generated when a "hole" in an inner shell is occupied by an electron of an outer shell, caused by the electron beam impact. There are three inner shells: M (with 5 subshells), L (with 3 subshells) and K (unitary shell), where the K shell is the closest to the nucleus, having the most characteristic energy line of the atom. In this way, the necessary beam energy has to be related to the K-L3 transition energy, being slightly greater, to efficiently excite the X-ray line, called "overvoltage". Every energy line has different groups, represented by letters of the Greek alphabet (α is the most important)

and intensities within the group, indicated by numbers (1 is the most important). In this way, the most indicated energy line to be detected will be the highest $K_{\alpha 1}$ among the analysed elements [54].

There are three main corrections, done according to theoretical models that together are known as ZAF correction method. They are the atomic number (Z) correction, absorption (A) correction and Fluorescence (F) correction. The ZAF correction method is iterative, so the first results are fed back to the following until a limit statistically satisfactory is reached. The X-ray relative intensities are measured against a control standard specimen, allowing the conversion of apparent concentrations (raw peak intensity) into corrected concentrations. For the Z correction, Incident electrons lose energy by interacting with bound electrons in the target. The number of the latter is equal to Z, per atom. The atomic mass (*A*) per electron is proportional to *A*/Z which increases with increasing Z. The energy lost by incident electrons per unit mass penetrated, the stopping power, follows this trend, so it increases with existing tightly bound inner electrons of atoms of high Z. The A correction mitigates the effect of heavier elements absorbing less energetic X-rays emitted by the lighter elements. The F correction minimizes the effect of a more energetic X-ray leaving the sample fluorescing the less energetic ones [55].

3.1.4 Vickers hardness

Hardness is defined as the measure of the resistance of a solid material to plastic deformation when a compressive force is applied. Hardness values are obtained by analysing the indentation left by an indenter with known geometry, that penetrated the sample into the surface. Vickers test is one possible method. It has an inverse pyramidal shaped indenter and is the most commonly used, since the returned number, Vickers Pyramid Number (HV), is independent of the size of the indenter. Before each indentation, the load and dwell time must be specified. Then, the surface area made by the indenter is evaluated. The angle of the indenter has a standard value of 136º, so the surface area (A_s) of the indentation is

$$A = \frac{D^2}{2 * \sin\left(\frac{136}{2}\right)} \tag{4}$$

where D is the arithmetic mean of the two diagonals of the indentation. HV is then the pressure of the applied load (F) on the surface area left by the indenter, given by

$$HV = \frac{F}{A_s} = \frac{2\sin\left(\frac{136}{2}\right)F}{D^2} \approx 1.8544\,\frac{F}{D^2} \tag{5}$$

Usually the diagonals are measured by the user and the HV is returned by the apparatus, in $kgf.mm^{-2}$ [56]. Macrohardness is commonly referred when the applied load on the indenter is higher than 1 kg, whereas in microhardness testing, applied loads are 1 kg and below. Some instruments are capable of conducting tests with loads in the order of 10 mg, referred as nanoindentation testers. The typical values of dwell time are from 10 to 15 seconds [57].

3.1.5 Laser flash technique

The thermal conductivity, k, of a material is a very important property to evaluate its thermal behaviour. However, the direct method to determine k requires the heat flux that gives rise to a measured temperature difference to be known, which is difficult to measure and control with accuracy [58]. On the other hand, k can be obtained through equation (6), relating thermophysical properties

$$k(T) = \alpha(T)\rho(T)\, c_p(T) \tag{6}$$

where α is the thermal diffusivity, ρ is the density and c_p the heat capacity at constant pressure. Thermal diffusivity, heat capacity and density experiments can be experimentally obtained by means of simple tests which are short and reliable. Moreover, data of the first two can be obtained in a large range of temperatures where the required sample's shape is easy to obtain. This is not verified for methods to obtain thermal conductivity; therefore, their combination is a more attractive method to obtain thermal conductivity values.

The physical principle of LFT was simulated using FEM and the extracted data was manipulated to obtain the thermal diffusivity value. Hence, a solid understanding of the theory behind this technique is necessary, where the mathematical model is studied in detail. The results of the modelling work are in Chapter 5 *Modelling*.

The method

Thermal diffusivity is obtained by the laser flash technique (LFT). The latter describes how rapidly does a material react to a temperature change [49].

LFT is a transient method where a short laser pulse irradiates the front surface of a sample with a disk format [49], that is adiabatically insulated. The time evolution of the temperature on the opposite face of the disk is measured by a pyrometer. This time-dependency of the temperature is registered until the temperature stabilizes. The thermal diffusivity is computed from the value of the half-rise time on the temperature-time plot(*) [49, 59].

Before each laser pulse, the initial temperature must be stable, to obtain accurate values of α. Several measures are done for the same initial temperature to obtain an accurate mean value. Also, the procedure is done for different initial temperatures, to find the temperature-dependency of thermal diffusivity.

(*) thermal diffusivity is obtained from the equation (26)

The ideal conditions for LFT are indicated in Table 3. However, usually there are deviations to these conditions. In this way, corrections during data processing are necessary to introduce [59], in particular the heat-loss models of Cowan, Clark and Taylor, and Degiovanni [60].

Table 3 Ideal conditions for practising the laser flash technique. Adapted from [59].

Assumptions	Consequence
Pulse absorption and its uniform distribution in a very thin layer of the specimen	Heat pulse travels only through the direction parallel to the beam
Radius of the laser beam equal to the radius of the sample	
Adiabatic conditions	Minimize the facial heat loss by radiation
Homogeneous material	Minimize thermal boundary resistance
Fully dense material	Minimize the results scatter - gases in existing porosity have very large diffusivity values but quite small conductivity values - strongly affected diffusivity values

Governing equations

LFT is based on the heat equation, which describes the spatial evolution of the temperature field in a body. The incompressible heat equation is expressed as

$$\rho c_p \left(\frac{\partial T}{\partial t} + (\vec{u} \cdot \nabla)T\right) - \nabla \cdot (k \nabla T) = \bar{\bar{\tau}} : \bar{\bar{\varepsilon}} + \rho h \tag{7}$$

where $\vec{u}$ is the convection velocity, h the heat source and the term $\bar{\bar{\tau}} : \bar{\bar{\varepsilon}}$ is the frictional viscous heating, being negligible in most cases [17].

For LFT the exposure time of the sample to the laser is so short that is admitted the material does not change from the solid state to the liquid state. Hence, the equation applies to a solid body and equation (7) simplifies to

$$\rho c_p \left(\frac{\partial T}{\partial t}\right) - \nabla \cdot (k \nabla T) = \rho h \tag{8}$$

The pulse emitted for a short time Δt of energy Q is absorbed by the sample in its superficial area, A_c, across a thin surface layer with a thickness g. This energy can be treated as an internal heat source $h(x, t)$, given by

$$\rho h(x,t) = \begin{cases} \dfrac{Q}{A_c g}\delta(t), 0 \le x \le g \\ 0, \qquad g < x < L \end{cases} \tag{9}$$

where $\delta(t)$ is the Dirac delta function, that limits the heat source for the time $t = 0$.

For homogeneous materials, k can be considered constant. If the heat conduction takes place in only one direction, equation (8) simplifies to

$$\rho c_p \left(\frac{\partial T}{\partial t}\right) = k\left(\frac{\partial^2 T}{\partial x^2}\right) + \rho h(x,t) \tag{10}$$

Using equation (6) in (10), one has

$$\left(\frac{\partial T}{\partial t}\right) = \alpha\left(\frac{\partial^2 T}{\partial x^2}\right) + \frac{1}{c_p}h(x,t) \tag{11}$$

This equation has to be solved assuming the following adiabatic boundary conditions

$$\frac{\partial T(0,t)}{\partial x} = \frac{\partial T(L,t)}{\partial x} = 0, \quad t > 0 \tag{12}$$

where L is the thickness of the sample. The latter conditions state that the heat fluxes between the disk faces and the surroundings are null.

The solution of equation (11), defining the temperature (T) at a given time and position, within the plate, is given by equation (13), where T_i is the initial temperature.

$$T(x,t) = T_i + C_0 + \sum\nolimits_{n=1}^{\infty} C_n \, exp\left(\frac{-n^2\pi^2\alpha t}{L^2}\right) \times \cos\left(\frac{n\pi x}{L}\right) \tag{13}$$

where the constants C_0 and C_n are

$$C_0 = \frac{1}{L}\int_0^L h(x')\,dx' = \frac{1}{L}\left[\int_0^g \frac{Q}{\rho c_p A_c g}dx + \int_g^L 0\,dx\right] = \frac{1}{L}.\frac{Q}{\rho c_p A_c} \tag{14}$$

$$\begin{aligned} C_n = \frac{2}{L}\int_0^L h(x')\cos\left(\frac{n\pi x}{L}\right)dx' = \frac{2}{L}\left[\int_0^g \frac{Q}{\rho c_p A_c g}\cos\left(\frac{n\pi x}{L}\right)dx + \int_g^L 0\,dx\right] = \\ = \frac{2}{L}\frac{Q}{\rho c_p A_c g}\frac{L}{n\pi}\sin\left(\frac{\pi n g}{L}\right) = \frac{2}{L}.\frac{Q}{\rho c_p A_c} \end{aligned} \tag{15}$$

As it is assumed that the energy pulse q is absorbed at a very thin layer, in the last step of equation (15) the ratio g/L is sufficiently small and the approximation $\sin(\pi n g/L) \approx \pi n g/L$ is valid.

Substituting the expressions obtained for C_0 and C_n in equation (13), and considering that the temperature increase is expressed by $\Delta T = T + T_i$, the latter becomes

$$\Delta T(x,t) = \frac{Q}{\rho c_p A_c L}\left[1 + 2\sum_{n=1}^{\infty} exp\left(\frac{-n^2\pi^2\alpha t}{L^2}\right) \times \cos\left(\frac{n\pi x}{L}\right)\right] \quad (16)$$

Knowing that thermal diffusivity is determined by measuring the temperature in the rear face of the disk at a given time t, the equation of interest is $T(L,t)$. Here, the cosine term becomes $\cos(n\pi L/L) = \cos(n\pi) = (-1)^n$ and the resulting equation for the temperature increase is

$$\Delta T(L,t) = \frac{Q}{\rho C_p A_c L}\left[1 + 2\sum_{n=1}^{\infty} (-1)^n exp\left(\frac{-n^2\pi^2\alpha t}{L^2}\right)\right] \quad (17)$$

The latter reveals that when $t \to \infty$, the ΔT at the rear face will approximate to the maximum temperature increase, so

$$\Delta T\ (L,\ t \to \infty) = \frac{Q}{\rho C_p A_c L} = \Delta T_{L,max} \quad (18)$$

Equation (17) can be used to determine α through the relationship between α and the time to reach 50% of the maximum temperature increase at the rear face, $\Delta T_{L,max}$.

This time parameter is called the half-time rise ($t_{1/2}$) and is obtained through a dimensionless temperature-time equation. To visualize the curve behaviour, the parameters in the axes are normalized.

To normalize the time, the term in equation (17) related to time is analysed

$$\exp(x) \leftrightarrow x = -n^2\ \frac{\pi^2\alpha}{L^2}\ t \quad (19)$$

where the characteristic time taken from the expression (19) is τ:

$$\tau = \frac{L^2\ (m^2)}{\pi^2\alpha\ \ (m^2.s^{-1})}\ \rightarrow\ \tau\ (s) \quad (20)$$

The dimensionless time parameter is obtained dividing the real-time, t, by the characteristic time, τ

$$\omega = {}^{t}/_{\tau} = {}^{\pi^2\alpha t}/_{L^2} \quad (21)$$

The temperature parameter is normalized to the maximum temperature, which expression is (18). Its resulting units are detailed below

$$\Delta T_{L,max} = \frac{Q(J)}{\rho(kg.m^{-3})C_p(J.kg^{-1}.K^{-1})A_c(m^2)L(m)} \rightarrow \Delta T_{L,max}(K) \quad (22)$$

The latter will be the transformation variable that normalises the instant temperature to obtain a percent rise $V(L,t)$

$$V(L,t) = \frac{\Delta T(L,t)}{\Delta T_{L,max}} \tag{23}$$

The adimensional form of equation (17) is

$$V(\omega) = 1 + 2\sum_{n=1}^{\infty}(-1)^n exp\,(-n^2\omega) \tag{24}$$

Computing the half-rise $V = 0.5$, the corresponding value for ω is $\omega = 1.37$, being now possible to relate α to $t_{1/2}$

$$\omega = 1.37 \leftrightarrow \frac{\pi^2 \alpha t_{1/2}}{L^2} = 1.37 \tag{25}$$

or

$$\alpha = 0.1388\frac{L^2}{t_{1/2}} \tag{26}$$

where 0.1388 is the corresponding value for a 50% rise of T (L,max) [49, 59, 61]. Other constants correspond to other percent rises, but the latter is the most used and will be always the chosen in the forward study. Thus, in LFT, the variables needed to be determined are L and $t_{1/2}$(*Adapted from* [49, 59, 61]).

Figure 10 is a representation of the analytical solution of $V(\omega)$, corresponding to the percent temperature rise versus the dimensionless time. The dimensionless time, $\omega_{1/2}$, corresponding to the real time $t_{1/2}$ is also indicated.

Figure 10 (a) Plot of the analytical solution represented by equation (24) where V = ΔT/ ΔTmax and ω = t/τ

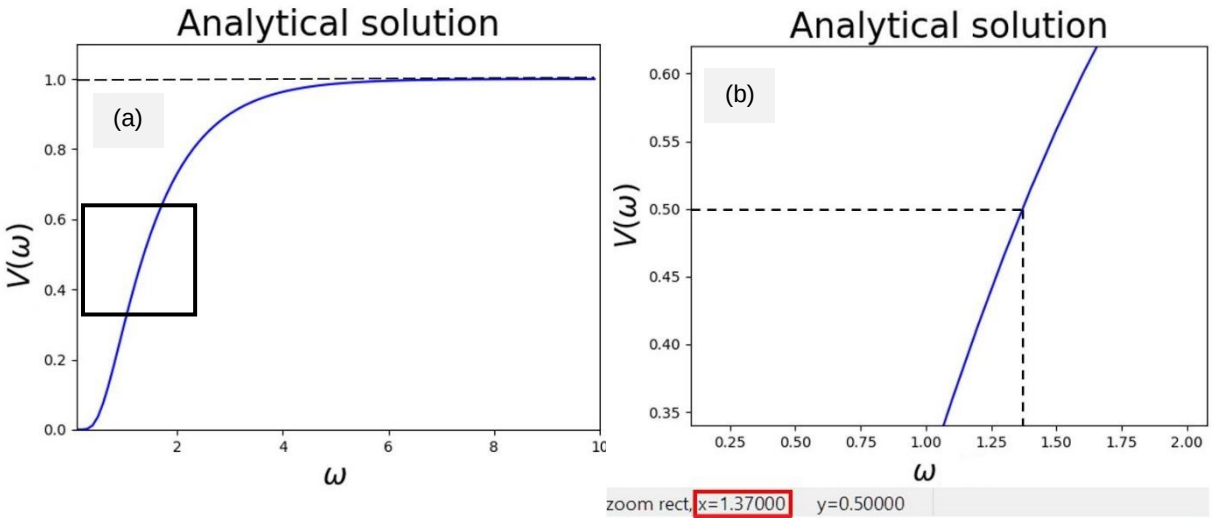

3.1.6 Modulated differential scanning calorimetry

This technique is a developed extension of differential scanning calorimetry (DSC). DSC is a technique that measures temperatures and heat flows associated with transitions in materials as a function of time and temperature. Such measurements provide quantitative and qualitative information, such as glass transitions, reaction kinetics, melting behaviour, thermal history, the degree of crystallinity and other properties. For DSC, the same signal contains all these thermal events that occur at the sample, whereas in MDSC, they can be separated by a mathematical treatment into reversing and non-reversing heat flow, and heat capacity. This feature enhances the sensitivity of the apparatus and its results [62].

For a given sample, the rate of heat flow, $^{\partial H}/_{\partial t}$ is linearly proportional to heating rate, $^{\partial T}/_{\partial t}$, due to heat capacity, $\mathrm{C_p}$.

$$\frac{\partial H}{\partial t} = \mathrm{C_p}\frac{\partial T}{\partial t} + f(T,t) \tag{27}$$

MDSC separates the total heat flow into the part that responds to a heating rate and the one responding to absolute temperature, where any heat flow detected at a null heating rate is attributed to kinetic processes $f(T,t)$ in the sample. Hence, the reversing heat flow (rev HF) is calculated from reversing heat capacity signal (rev $\mathrm{C_p}$) through the relation $rev\ Heat\ Flow = rev\ \mathrm{C_p} \times avg\ Heat\ Rate$, and the non-reversing heat flow (n-rev HF) is, logically, $n - rev\ Heat\ Flow = total\ Heat\ Flow - rev\ Heat\ Flow$. The value of specific heat comes from the relation $c_p = rev\ \mathrm{C_p}\ /m_{sample}$.

The ideal conditions for MDSC are indicated in Table 4, as well as the respective consequences.

Table 4 Ideal conditions for the modulated differential scanning calorimetry (adapted from [62]*)*

Assumptions	Consequence
Sample is sufficiently thin	Any significant temperature gradients are avoided occurring within it as the sample is heated and cooled
Rate at which heat is supplied to the sample is measured by a perfect device that responds instantaneously	No data shift in the time axis
Homogeneous material	Minimize thermal boundary resistance
Fully dense material	Minimize the results adulteration - gases in existing porosity affect the value of heat capacity

3.1.7 X-ray diffraction

X-ray diffraction data is the result of relative intensity (I) for each reflection with a set of plane Miller indices, along with the corresponding scattering angle (2θ) for that reflection. Radiation incident upon a crystal is diffracted in different ways. When the wavelength of the incident radiation (λ) is on the same scale as the atom spacing in a crystal, the diffraction gives rise to a set of well-defined beams arranged with a characteristic geometry, thus forming a diffraction pattern. Hence, the intensities of the diffracted beams are a function of the arrangements of the atoms, where a beam of radiation will only be diffracted when it strikes a set of planes in a crystal, if the geometry of the situation fulfils quite specific conditions, defined by Bragg's law, given by

$$n\lambda = 2d \cdot \sin\theta \tag{28}$$

where, n is an integer determined by the order given, d is the interplanar spacing in the atomic lattice of the structure, and θ is the angle between the incident ray and the scattering planes - the Bragg angle.

X-ray diffraction is used to phase identification, determination of crystallite size and lattice parameters of the unit cell dimension [63].

3.2 Numerical techniques

3.2.1 Finite element method

FEM is a numerical tool for solving partial differential and nonlinear equations, where the majority cannot be solved with analytical methods. Instead, a discrete approximation of the equation is provided, which is then solved exactly. In this way, FEM is widely used in engineering to reinforce the design process by predicting the structural behaviour of components [64]. FEM involves the decomposition of space domain into a discrete number of "tiles" called "finite elements", with simple geometries and linear or non-linear edges, that when united approximates a geometric domain, named "mesh". These elements are connected by points called "nodes", where the function runs and return a finite number of values that later are all "stitched" together.

The number of nodes determines the matrix size to be solved, where a bigger matrix implies a more accurate approximation to the real geometry. More nodes should be concentrated in the more critical regions, generating a more refined mesh.

Constitutive equations

Simulations are usually done to study the thermal and/or mechanical behaviour, mainly the fracture occurrence in the simulation studies of the mechanical conditions of the monoblock of the divertor in fusion reactors [7, 47].

For simulations of the thermal behaviour, the constitutive equation is the heat equation, which describes the spatial evolution of the temperature field in a body. The heat equation for an incompressible material is expressed in equation (7). For the present case, the simulation of simplified LFT considers the model to be a solid body without phase transition for liquid state and equation (7) simplifies to equation (8).

Space and time algorithms are specified in point Chapter 5 *Modelling.*

3.3 Experimental Procedures

Here is outlined the experimental work on the synthesis of the WC-Cu cermets. Detailed information is given on the used raw materials and the procedures and respective conditions to prepare and characterize the samples.

3.3.1 Raw materials

The WC-Cu cermets were produced by hot pressing, at different percentages by volume: 25, 50 and 75% of WC, and the remainder of Cu.

The raw materials were in powder form. Cu spherical powders were used as the matrix material (average size: 37 µm, purity: >99.9%, Alfa Aesar) and WC particles (average size: 18 and <1 µm, purity: >99.5%, Sigma-Aldrich and Alfa-Aesar, respectively) as particulate reinforcement, with an irregular shape. A share of WC particles was coated with Cu by D.C. magnetron sputtering deposition, using pure copper targets. The powders were placed in a vibrating container before the deposition. The deposition took place under argon atmosphere. The initial pressure was set at 5×10^{-6} mbar to avoid target contamination and the deposition pressure at 5×10^{-3} mbar, to avoid Cu scattering due to collision with Ar atoms. The applied power in the target was of 600W and the deposition lasted for 4h30 m. The magnetron sputtering technique took place in the facilities of CEMMPRE, at *Universidade de Coimbra.*

Bimodal particle size

For the bimodal particle size (18 + 1 µm), the volume fraction of WC is constituted by 50% of each size.

Monomodal particle size

This category has simple WC particles and WC particles coated with a nanolayer of Cu. The systems are addressed as *uncoated* and *coated*, respectively.

The mass of Cu from the coats is determined facing the total required Cu mass, in order to add the remaining Cu mass in virgin powder form, until accomplishing the tabled volume fractions of this component: 25, 50 and 75 %. This was achieved determining the average value for the diameter of the WC particle as well as for the thickness of the Cu coating layer through SEM-BSE imaging. Ten covered particles were analyzed and for each fifteen measures were taken to calculate the thickness of the layer and two measures for the sizes (the arithmetic mean of the larger and the smaller size). For the calculations, the particles were considered spherical and the coating layer with a constant thickness. The average values obtained for the size and thickness were of 11.58 ± 0.76 µm and 0.56 ± 0.19 µm, respectively. The average size of the WC pre-sintered powders did not differ from the sintered, with relevance (see Annex A). Other important measures to determine the mass of Cu from the coats are in Annex A.

Graded composition

The produced WC-Cu cermet with graded composition has three sublayers, where the WC particles have a monomodal size distribution of 1 µm. Here, the three powder mixtures have a gradual composition, as seen in Figure 11, where the mixtures were deposited simply on top of the other, in the mould cavity.

Figure 11 Scheme of the graded composition

3.3.2 Synthesis

The powders were mixed by turbula blending for one hour, after being weighted inside a glove box, to avoid copper oxidation and then submitted to unidirectional hot pressing. The sintering process consisted in heating the material till a temperature varying from 850 to 1150ºC, under pressures from to 22 to 47 MPa, during 15 to 25 minutes, in an Idea Vulcan 70 VP heating furnace. The submitted material was heated by induction phenomena in an atmosphere of nitrogen, to avoid further oxide formation. The estimated heating rate is approximately 120 °C/min and is the same for all the cycles. The powder mixture was consolidated in a graphite die of 55x10x5 mm in size (cavity volume of 2.75 cm^3). The graphite mould is, to a certain extent, a *blackbody,* meaning that, in thermal equilibrium, it has an emissivity ε=1 and thus the radiation

losses are negligible, not affecting the measured value of temperature. The pyrometer that measures the sintering temperature is attached to the graphite mould and is calibrated once per month.

The chosen compositions and respective sintering conditions were adopted from the previously done work [18], indicated in Table 5. The sintering parameters considered for the segment with graded composition is also in this table.

Table 5 Parameters for the sintering cycle corresponding to the densest samples: temperature, pressure and holding time

Material composition (%V/V)	Sintering cycle		
	Temperature (°C)	Pressure (MPa)	Holding time (min)
25WC-75Cu	900	22	5
50WC-50Cu	1060	37	5
75WC-25Cu	1150	47	6
Graded composition	850	28	3

3.3.3 Thermal, physical and mechanical properties

The following properties of the cermets were studied: density, thermal diffusivity, hardness and heat capacity.

The theoretical density of the cermets was calculated by

$$\rho_{cermet} = f_{WC}\rho_{WC} + (1 - f_{WC})\rho_{Cu} \tag{29}$$

where ρ_{cermet}, ρ_{WC} and ρ_{Cu} represent the theoretical density of the cermet, WC and Cu, and f_{WC} the volume fraction of the WC phase. The real density of the produced cermet, ρ_{real}, was obtained by the method of Archimedes, based on the water displacement method, through the following relation

$$\rho_{real} = \rho_{water} \times \frac{specimen\ mass}{specimen\ mass - immersed\ mass} \tag{30}$$

where ρ_{water} is the water density at RT.

The ratio of the densities returned the densification and porosity of the experimental material, by

$$Densification = 1 - Porosity = \frac{\rho_{real}}{\rho_{cermet}} \times 100 \tag{31}$$

Thermal diffusivity values were measured by the laser flash technique on the apparatus *FL-5000* from Anter Corporation, for samples with a densification higher than 95%, due to the porosity [59]. A high-power neodymium laser is used as a heat source, with an energy of approximately 35 J, in about 1 ms. The laser beam is strong and uniform in a cross-section area, and the front surface of the sample is covered with a very thin graphite layer, allowing the heat to dissipate rapidly and uniformly through this surface. The sample

is heated in a graphite furnace in argon atmosphere and the test is carried out in a temperature range from 100 to 400ºC. Samples have a disk format with a 10 mm of diameter. The manufacturer states that the α values have an accuracy of 5% using this equipment.

The heat capacity was measured using modulated differential scanning calorimetry, in a Q2000 apparatus, from TA Instruments. A sapphire sample was used to calibrate the heat capacity, through K, the obtained ratio of the theoretical heat capacity of a sapphire (standard material), to the measured heat capacity of the sample material, at multiple temperatures, in the MDSC apparatus. The value of K was introduced into the "Cell Calibration" table. The test was run within the same temperature range as LFT - from 100 to 400ºC. The heat capacity was only measured for the material to be modelled, to obtain its thermal conductivity. The sample weighted 100 mg, to cover the bottom of the crucible. The accuracy of the data from this equipment is 0.05%, according to the manufacturer.

Thermal conductivity was calculated for the only material with all the necessary properties experimentally obtained: α, ρ and c_p, which was 75 vol% WC with bimodal WC particle size distribution. This study was necessary for the modelling work, in Chapter 5 *Modelling.*

Vickers hardness of the WC-Cu cermets was measured on a ZHVμ Micro Vickers hardness tester. The test conditions were the applied load of 2 and 20 N and a dwell time of fifteen seconds. The average and standard deviation values were obtained for each sample from five indentation tests, spaced of three diagonals in length away. The apparatus was validated by matching measures on a certified test block of 200 grams.

3.3.4 Metallography and composition

All the produced segments were cut and mounted. The surfaces of the samples were polished down to 0.04 μm colloidal silica suspension, followed by ultrasonic cleaning.

SEM images were used with the goal of studying the grain size and shape, the amount of surface area covered after sputtering, the average thickness of the cover of the sputtered powders and finally the overall structure and interfaces of the produced materials. For the last point, the homogeneity of the dispersed phase and its adhesion to the matrix were analysed. SEM images were also used to evaluate the accuracy of the Archimedes method, which measures the materials' real density and porosity.

Backscattered electron (BSE) imaging was used to distinguish the dissimilar phases and also to detect existing compounds or impurities, as BSE respond to the mean atomic number, which easily differentiates the present phases [54].

The used equipment is the SEM with field emission gun (FEG), FEG-SEM JEOL 7001F, in the following conditions: working distance (WD) WD = 10 mm for compact and powder samples and voltage of 20 kV. The instrument is equipped with an Oxford EDS system that was used for point analysis.

XRD measurements were carried out to assist in identifying the present phases. The apparatus is a Bruker D8 AXS diffractometer that produces characteristic radiation from an anode made of copper (Cu $K\alpha_1$ and $K\alpha_2$ lines). The voltage was set at 40kV and the current at 40mA. The ICDD Database was used for phase identification. The Powder Cell software package was employed to simulate diffractograms for comparison with experimental data. The 2θ for the diffractogram was set from 25 to 100º, the steptime was set as 0.02s and the stepsize as 5 times. The X-ray diffraction was performed only at the samples of the bimodal system, due to time limitation.

The richest samples in Cu were chemically etched by a solution with 5 g of ferric chloride ($FeCl_3$) concentration, 100 ml of water or ethanol and 20-50 ml of hydrochloric acid [65], followed by an immediate wash.

The indentation marks resulting from the Vickers hardness measurements were observed with SEM in order to evaluate the interfacial cohesion between the matrix and dispersed phase and the spot mechanical strength in both phases. These observations allow a qualitative discussion on the dependence of the phase and interfacial strength of the WC-Cu cermets, regarding their particle size, type of bonding or matrix volume fraction.

3.3.5 Computational analysis

The models were generated using the FE modeller ElmerGUI, which defines the geometry and mesh parameters of the model, along with the respective material properties, boundary conditions, initial conditions and solving equation [66]. The used FE solver that implement FEM was ElmerSolver. The effect of thermal transport was measured through time and special variations, detailed in Chapter 5 *Modelling.* The output data from ElmerSolver is visualized with Paraview. This program allows the study of the time progression on an animated model and on the plot at the same time, what eases the comparison among different simulations.

The time and temperature data are analysed with the programming language Python 3.5, namely the Anaconda distribution. Python detains *libraries* that are very used in data science, to manipulate datasets or construct and edit plots. The library Numpy is called to import mathematical functions (*e.g.* exponential function) constants (*e.g.* π) and multidimensional arrays (*e.g.* as a set of points); and Matplotlib is the plotting library, where the manipulated data is viewed, and the plot details are easy to add and edit (*e.g.* the axes titles, the line styles and the legends). Also, the library Scipy is used to import an optimization algorithm that is required in point 5.3.1 *Experimental curve*.

This page was intentionally left blank

Chapter 4 WC-Cu cermets:

The present chapter comprehends five sections, namely the consolidation, microstructure, X-ray diffraction, thermal analysis and hardness. The first three sections allow a general visualization and comparison of the resulting densifications, microstructures and phase fractions of all the produced cermets. The following sections present results regarding thermal and mechanical properties.

4.1 Consolidation

Consolidation was performed by HP sintering, where the sintering temperature (Ts), pressure and holding time are indicated in Table 5, in Chapter 3 Techniques and experimental procedure for each composition (25, 50 and 75 vol.% of WC and the remain of Cu). Also, Ts is plotted versus time, for the three different compositions, in Figure 12. The pyrometer reads Ts at the surface of the graphite mould and not directly at the surface of the green body. Thus, there is a temperature increment and the linear cooling rate represented is an approximation of the real cooling rate of the materials, that is the behaviour that is usually reported during cooling

Figure 12 Temperature versus time of sintering of the cermets with compositions of 75WC-25Cu, 50WC-50Cu and 25WC-75Cu, with the indication of the melting temperature of Cu. Heating rate of 2ºC for the three compositions.

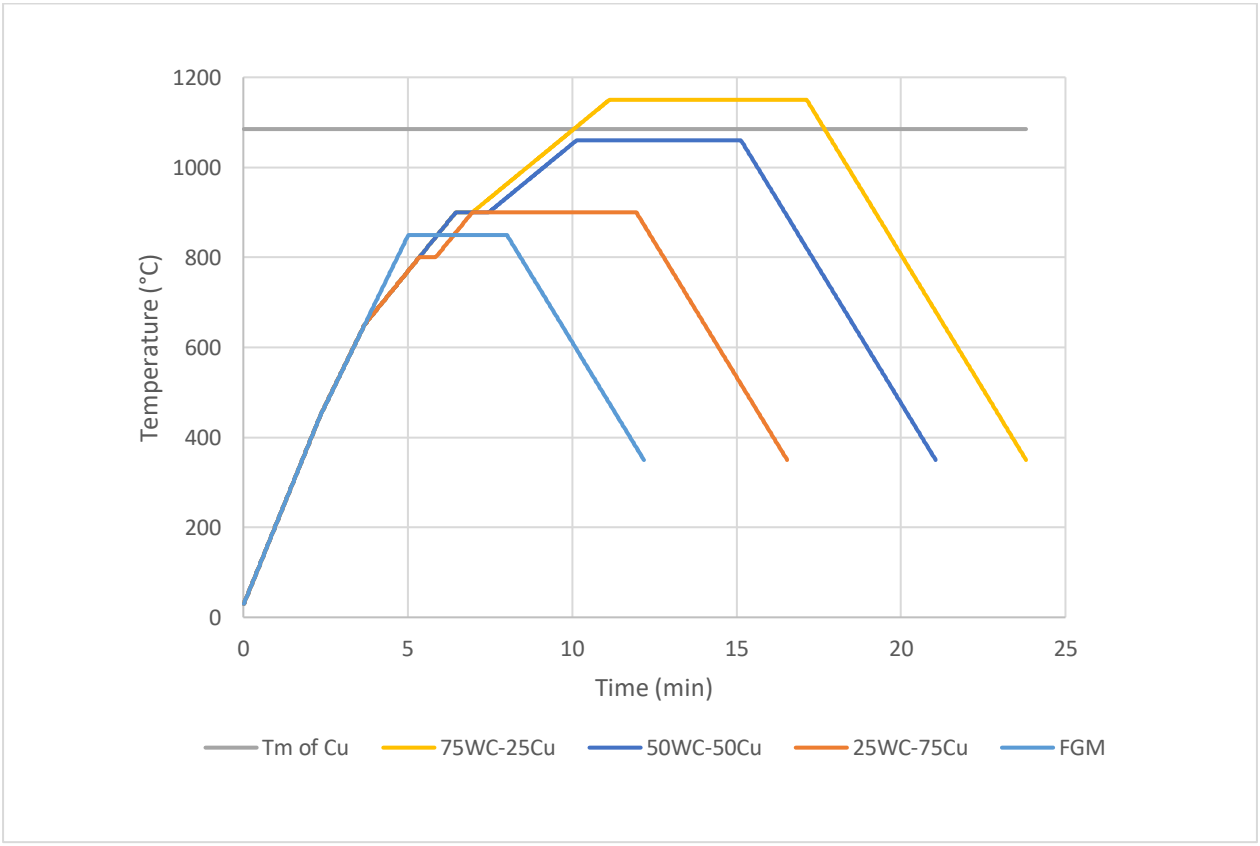

A code is attributed to each produced WC-Cu cermet, according to with their WC volume content and type of dispersion system (bimodal or monomodal) and use of coated particles or not. The names regarding the materials having a bimodal mixture of particles are indicated in Table 6, those with a monomodal size are in Table 7 and the material with a graded composition in Table 8. The obtained densifications are also indicated in the respective tables. For the bimodal mixture of particles, a weight ratio of 1 to 1 of fine and coarse particles was used.

Table 6 Densification obtained for the WC-Cu cermets with a bimodal WC particle size distribution

Material composition (%V/V)	Material code	Densification (%)
25WC-75Cu	25WC_bi	83
50WC-50Cu	50WC_bi	76
75WC-25Cu	75WC_bi	95

Table 7 Densification obtained for the WC-Cu cermets with a monomodal WC particle size distribution

Material composition (%V/V)	Coating	Sample name	Densification (%)
25WC-75Cu	Coated	25WC_*coated*	95
	Uncoated	25WC_*mono*	81
50WC-50Cu	Coated	50WC_*coated*	98
	Uncoated	50WC_*mono*	No consolidation
75WC-25Cu	Coated	75WC_*coated*	No consolidation
	Uncoated	75WC_*mono*	84

Table 8 Densification obtained for the WC-Cu cermet with a graded structure of sublayers with the compositions of 25WC, 50WC and 75WC in volume percentage, and the remainder of Cu

Material composition (%V/V)	Sample name	Densification (%)
Sub-layers with gradual variation in composition	Graded composition	79

According to Figure 33, sample 25WC_bi was sintered at 900ºC. Knowing that T_m^{Cu} is 1085º C, solid-state sintering should have taken place. However, the Cu melted in the 25WC_bi cermet, since it spread out from the graphite mould as shown in Figure 13. The phenomenon is recurrent, minding the previous work.

Figure 13 Sample 25WC_bi resulting from hot pressing

The material melting at such low temperature could have happened due to either the presence of impurities or the misleading values read by the pyrometer in the sintering machine. Their presence is studied by X-ray diffraction and EDS.

The high-pressure conditions would logically, promote the T_m to increase, but the hot-pressing machine in use applies a maximum value of 0.047 GPa (47 MPa, 463,8 atm), which is not relevant comparing to the necessary magnitudes of pressure to actually rise the melting point. Figure 14 shows the T_m^{Cu}dependence on the applied pressure, which ranges from the atmospheric pressure to 50 GPa. According to the analytical expression for the T_m^{Cu} dependence on the pressure and the experimental data collected by Hieu et al. [67], an increase of the T_m^{Cu} is not expected at the current experimental conditions.

Figure 14 Melting temperature dependence on the pressure for copper, up to 50 GPa varying the fitting parameters for the same Tm equation (dashed and solid lines), compared to experimental data collected by Hieu et al.[67]

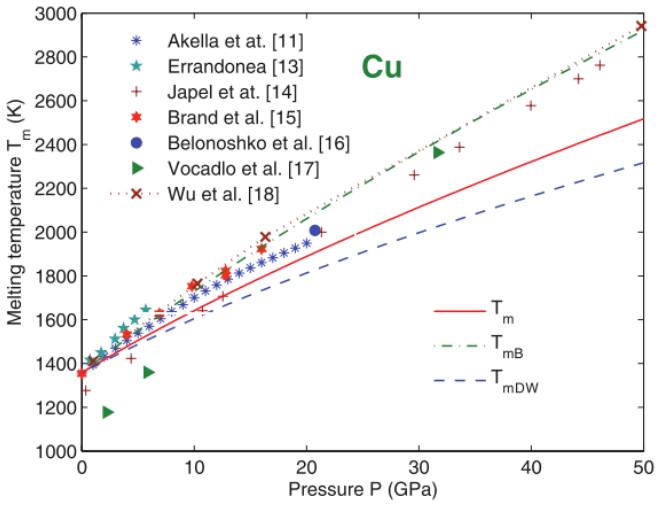

Attending on the possible presence of impurities, the formation of oxides is analysed. Copper corrosion rate is sensitive to the atmosphere relative humidity and reduced sulfur concentrations (H_2S), leading to Cu_2O formation. The rate of copper oxidation is also influenced by the exposure time, measured in hours [68]. The powders were mixed for one hour, and the waiting time for sintering ranged from 30 minutes to four hours, depending on the order of use of the press. The Cu-O phase diagram in shown in Figure 15 [25, 69].

Figure 15 Cu-O phase diagram general in (a) and with detail at lower temperatures and oxygen percentages in (b) [25, 69]

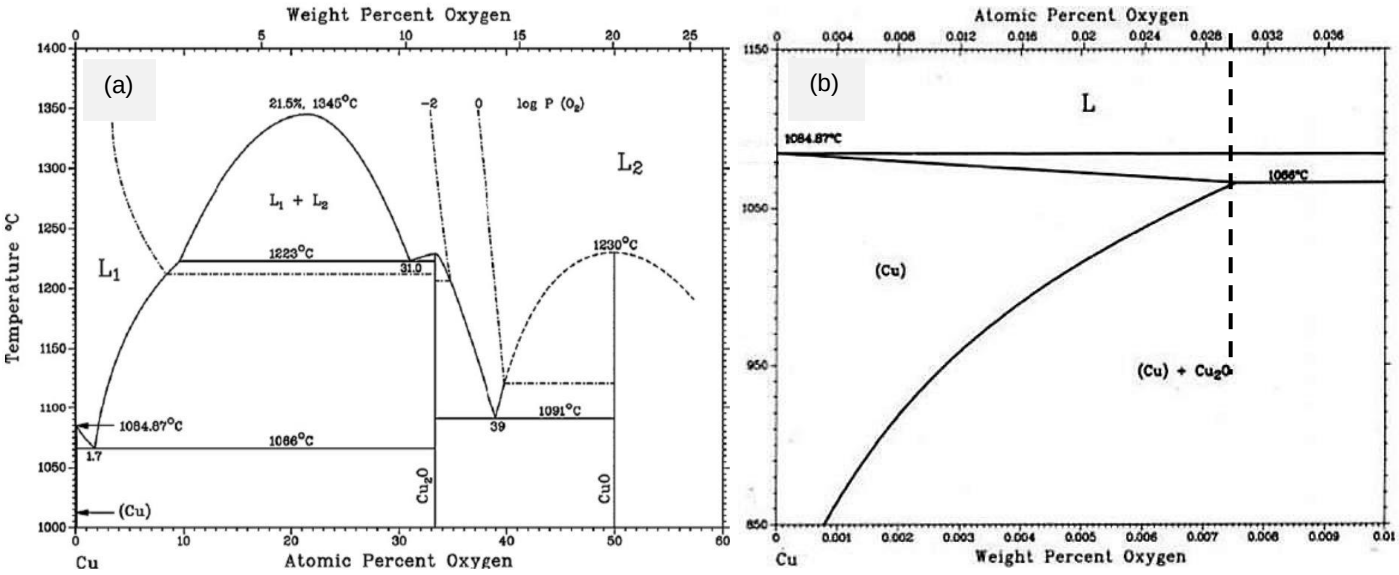

The diagram shows that Cu_2O starts forming at low temperatures, where approximately 8 ppm by weight of O_2 dissolve in Cu at a temperature of 850°C. Also, at 1066ºC, a temperature close to the T_m^{Cu}, there is a eutectic point for 75 ppm of O_2. For a O_2 weight content higher than 75 ppm, oxides will be present in the microstructure.

The produced cermets were submitted to X-ray diffraction and EDS to extensive structural analysis and detect possible impurities. The diffraction study is in point 4.2.2 *X-ray diffraction*.

4.2 Results and discussion

4.2.1 Microstructure

Bimodal mixture of particles

Representative microstructures from the cermets with a bimodal mixture (Table 6) are shown in Figure 16, for the three produced compositions. From the left to the right the magnification increases and from the top to the bottom WC content increases, specifically of 25, 50 and 75 volume percent, and the remain of Cu. The images were obtained by BSE imaging, so they are formed based on compositional contrast, where the darker area corresponds to copper regions, the lighter element, while the brighter area is associated to the WC particles, that has the higher atomic number. The pitch-black zone indicates the existing porosity. The densification results and the sintering temperature and pressure are placed in the right of the produced cermets.

The specimens were cut in the transversal cross-section direction, in the centre.

Figure 16 SEM-BSE of cermets with bimodal particles with compositions of (a), (b), (c) 25%WC-75%Cu; (d), (e), (f) 50%WC-50%Cu; (g), (h), (i) 75%WC-25%Cu and respective sintering temperature and pressure and densification

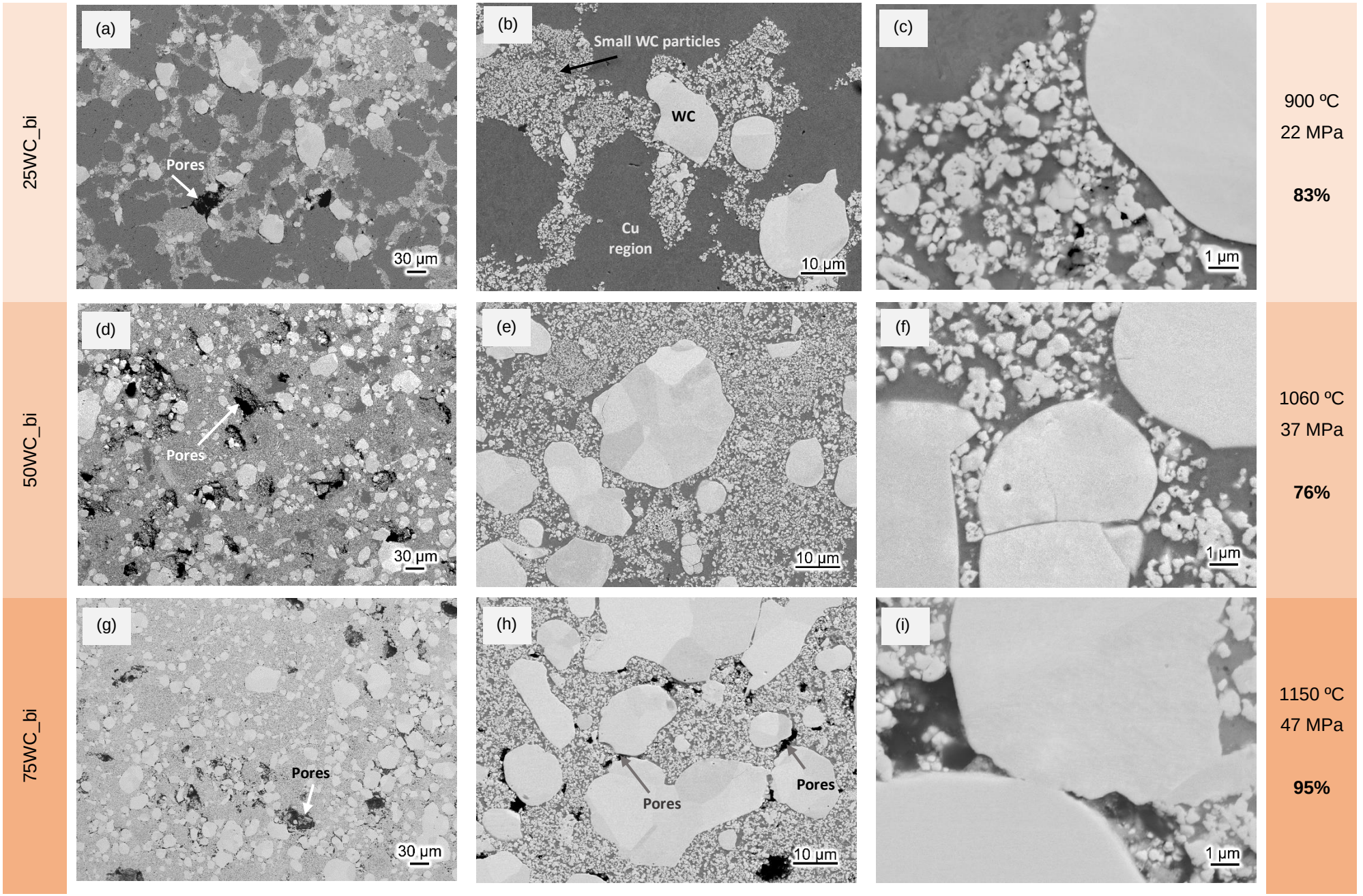

The microstructures in Figure 16 at the lower magnification, (a), (d) and (g), show not very well homogenised ceramic particles in the structure for the three compositions, where the occurrence of clustering of the reinforcing phase is more relevant for the 25WC_bi, mainly for the smaller particles, since there are no sufficient coarse particles for the fines to fill the space and the Cu particles have a larger size (37 μm) than the reinforcing particles (1 and 18 μm).

Cu infiltrates among fine particles by the capillarity effect, where the liquid that wets the particles generates an inter-particle capillary force on grain contacts. Figure 16 (h) shows a not ideal wetting behaviour of Cu on WC, allowing some porosity to install on the ceramic-metal interfaces. The higher resultant porosity is in the periphery, hence the 25WC_bi images do not ideally represent the respective densification value. On the other hand, the dispersion of particles is well represented.

The filling of the spaces is noticeable among the bigger particles by the smaller ones, for the medium and higher content in WC, leading to a high densification for the sample with the highest WC content.

In general, the SEM images collected in Figure 16 show an apparently good adhesion between the two phases. A higher densification was obtained for the 75WC_bi, ($d = 95\%$) as expected, due to the liquid-state sintering under high pressure application, that allowed the Cu to infiltrate in the pores, combining with the large presence of physically and chemically stable particles that contribute in a big extent to the integrity of the specimen. The 25WC_bi specimen is 83% dense, with a big volume of pores in the surroundings. The specimen with intermediate composition, 50WC vol %, presents the highest porosity value. This phenomenon could be explained by a not enough operation time for the Cu to segregate to the existing pores, due to the large quantity of ceramic particles hindering the Cu path, allied to a low pressure.

Figure 17 shows the microstructure of the 25WC_bi sample, that has been etched. The scale bar has a 30 μm size which is close to the original Cu grain size (37 μm). The microstructure shows the inexistence of particle boundaries in the Cu phase and reveals the segregation of the reinforcement particles, which promotes the formation of copper regions. Elements of different nature tend to segregate and join in the same nature cluster to minimize the high energetic Cu-WC interface [70]. The apparent segregation and lack of grain boundaries suggest that liquid phase sintering took place, even for sintering temperatures occurring at 185ºC bellow T_m^{Cu}. This temperature can be achieved during temperature peaks, in the furnace.

Figure 17 Micrograph by SE imaging of the etched 25WC_bi sample

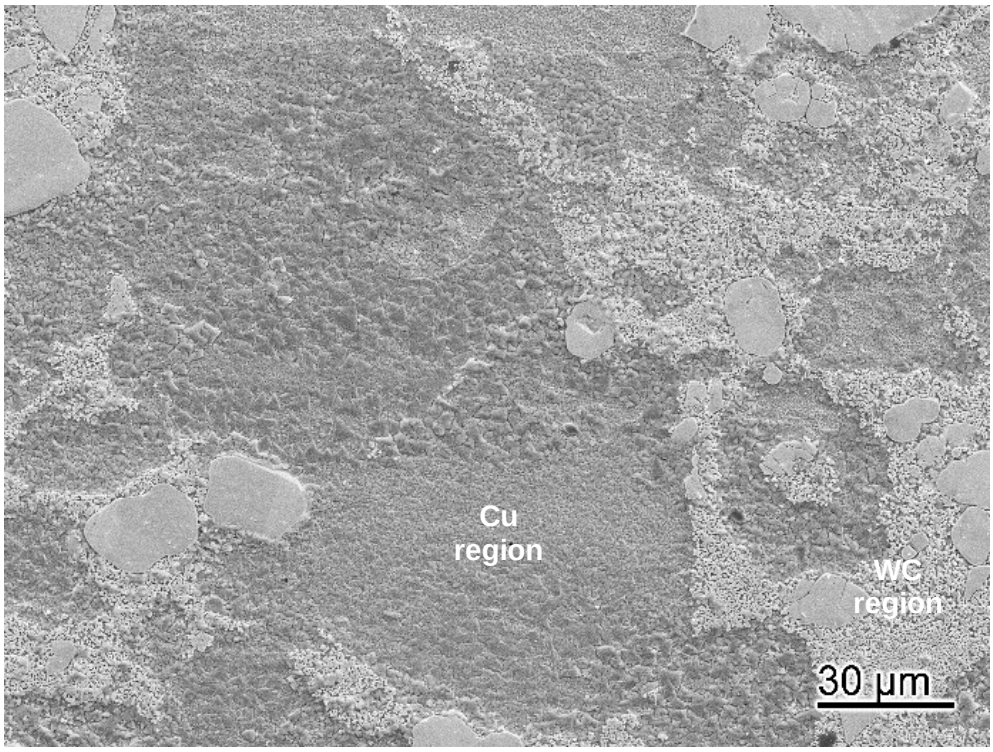

There was no copper draining of the 50 and 75WC_bi specimens, suggesting that a volume increase of the reinforcement phase hinders the escape of liquid Cu.

The average grain size of the sintered WC (14 ± 5 µm) is roughly the same as the initial powder size (12 ± 1 µm), indicative of the absence of grain growth of WC, during sintering. This retention of grain size must be due to the relatively low sintering maximum temperature (1060 ºC) for this material, as it melts at 2870ºC.

Nevertheless, a relevant share of porosity is located in the WC/Cu interfaces. In this way, a new strategy was adopted to produce new WC-Cu cermets – the pre-coating of the dispersed particles.

Monomodal mixture of particles

The new strategy to optimize the densification (higher than 95%) is to cover the ceramic particles (WC) with a thin layer of the same material as the matrix one (Cu), attempting to reduce the interfacial energy between the matrix and dispersed particles and consequentially, reducing the pores presence, heading to denser samples. Once again, the densification results and the sintering temperature and pressure are placed in the right of the produced cermets.

WC particles were covered with Cu by sputtering technology, which is not sensible to particles with an average size less than 10 µm. In this way, the dispersed phase is composed of a monomodal size dispersion of 18 µm, only. Cermets with uncoated 18 µm particles were also synthesized as control samples.

SEM images in Figure 18 show that a Cu layer was quite successfully implemented around the WC particles.

Figure 18 SEM images of coated WC particles, before powder mixing

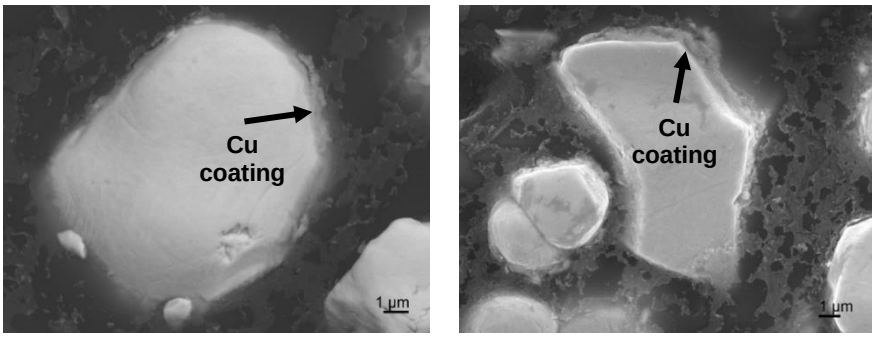

Microstructures corresponding to the monomodal mixture are presented in Figure 19, for the 25 and 50 vol.% WC, and Figure 20 for the 75 vol.% WC (Table 7).

The monomodal composites were sintered under the same conditions as the bimodal ones (see Table 5 in Chapter 3 *Techniques and experimental procedure*). For the present case, the copper has melted in the three compositions, for both the coated and uncoated samples, concluding that liquid-state sintering took place. Once again, there was Cu drainage from the moulds, but it took place for all the specimens except for the uncoated 75WC_mono. Such event could be explained by the use of big sized particles. Due to the mutual insolubility in the W-Cu-C system, the capillarity force is the main effect to obtain high densification. However, the capillary effect is more effective for Cu infiltration among finer particles and having acute angles [27, 28]. In this way, the use of big particles with roundish surfaces resulted in a decrease of the capillarity effect, leading to Cu draining from the mould in all the produced cermets with big sized ceramic particles. This was associated with lack of adhesion of the metal matrix to the particles, due to the non-immediate wetting of WC by Cu.

Figure 19 SEM images of 25WC-75Cu and 50WC-50Cu cermets with coated monomodal 18 µm powders and respective sintering temperature and pressure and densification

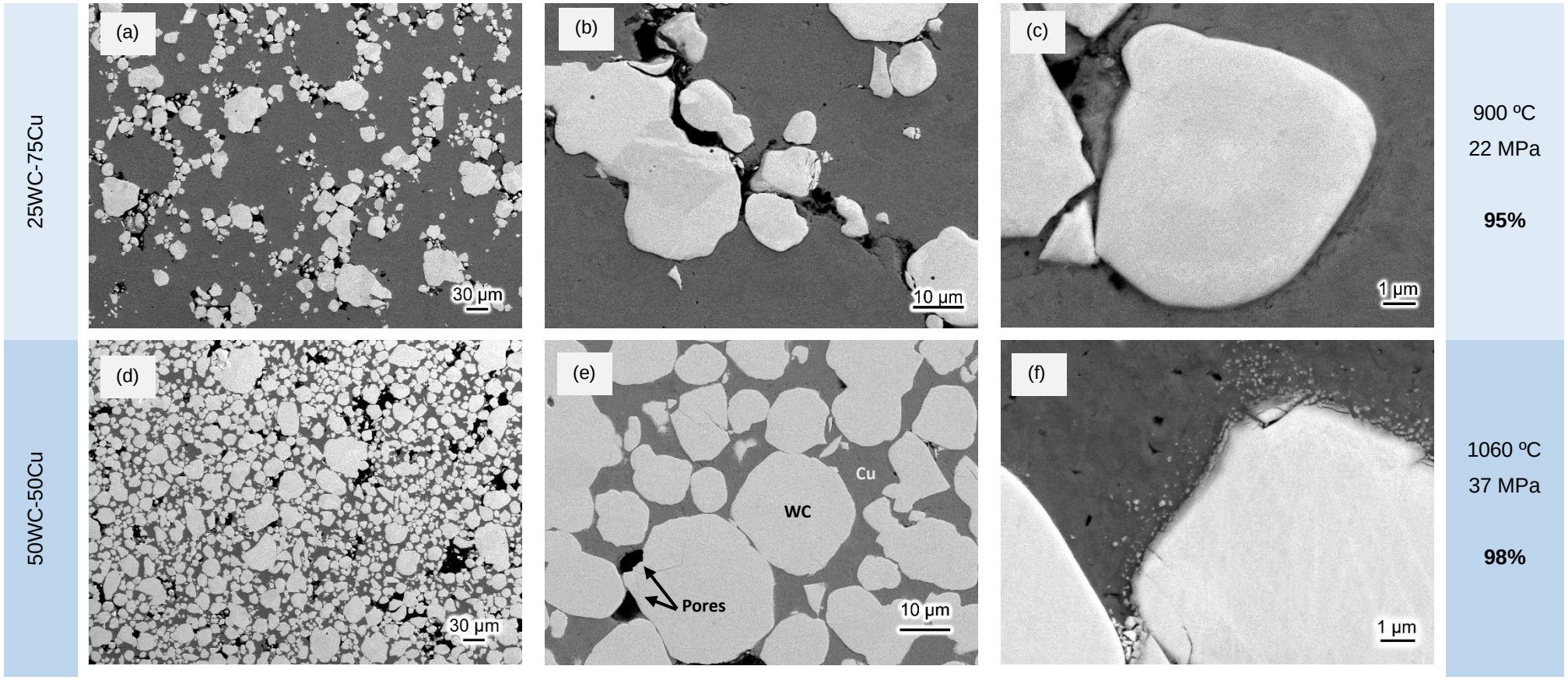

Figure 20 SEM images of 75WC-25Cu cermets with monomodal 18 µm powders, coated (blue) and uncoated (green) and respective sintering temperature and pressure and densification

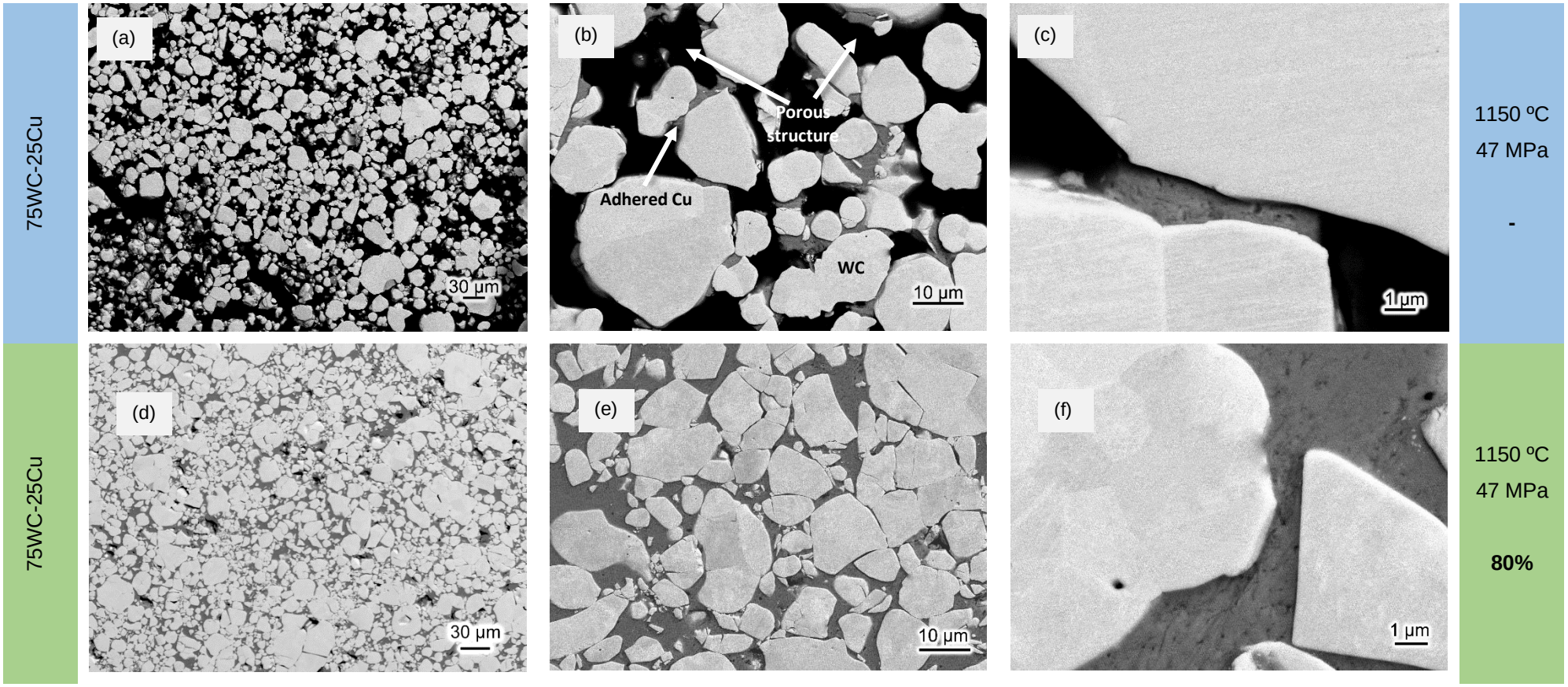

The microstructures of the sintered material wit coated particles in Figure 19 and Figure 20 reveal a big improvement on the adhesion of the WC grains to the Cu matrix for the compositions of 25 and 50 vol% WC, since the presence of pores in the interface between large particles and matrix was mitigated, resulting in higher densifications, 95 and 98% respectively, in comparison to the bimodal mixture, that achieved 83 and 76%. Coating the particle with the same material than the matrix, a less energetic interface between the Cu matrix and coated particles (Cu-Cu instead of Cu-WC interface) is created. Thus, the system promotes more the copper migration to the pores, resulting in less Cu-air interfaces. The decrease in WC-air interfaces is logically prevenient from the pre-coating process.

However, their obtained values for the monomodal system (95 and 98%) are not in agreement with the porosity showed in the micrographs of Figure 20 (a) and (d). This must be connected to the calculation of the share of Cu volume of the coating layers, which is dependent of the particle size, considered to be constant and spherical and the coat was assumed to be continuous. Such assumptions must carry a relevant error that leads to a final Cu volume larger than the real one. In this way, the assumed theoretical density is lower than the real one (equation 29), leading to a higher densification value (equation 31). Also, the Archimedes method to determine the real density is not the most accurate to proceed. However, its procedure is simple and fast.

The bimodal system achieved 83 and 76% of densification. It suggests that a copper coating can significantly decrease the interfacial thermal resistance between Cu and WC by limiting pores formation in their interface. Also, a more homogenized distribution of the ceramic particles is shown for all the compositions that consolidated.

The 50WC_mono and 25WC_mono showed opposite behaviours comparing to the 75WC_mono: for the coating system, the specimens with less WC content obtained almost fully dense structures, whereas the richer in WC did not consolidate. For the non-coating system, the first ones lost a big portion of copper (see Figure 21), while the 75WC_mono was the only one that consolidated.

Figure 21 Samples (a) 25WC_mono and (b) 50WC_mono resulting from hot pressing

Figure 20 (b) shows the poor consolidation of the coated 75WC_mono. The sintering temperature was, at least, 65º above T_m^{Cu}, that must have lead to the decreasing of viscosity, μ, that is inversely related with the infiltration rate, Φ, through the relation $\Phi \propto \frac{r_m}{\mu}$, given by Martins *et al.* [28], where r_m is the meniscus radius which in a sintering system can be associated with the meniscus created by two neighbouring particles, that is larger comparing to the bimodal system. Furthermore, with the particles

being previously lubricated due to the soft Cu coating, the matrix Cu could have flowed more easily. Also, the applied pressure (47 MPa) during the sintering cycle could have been too high, since, under pressure, the accommodation of coarser particles is interrupted sooner than when there are finer particles which are pushed towards the interstices. Larger particles appear to move more easily within the ductile matrix than smaller particles, under the same applied load. Thus, the high sintering temperature and pressure for the latter cermet, allied to powder characteristics might have led to the expel of Cu out of the mould.

The micrographs in Figure 20 with the lower magnification show the broader sizes of WC grains, indicating the broader powder size distribution, which was not considered for the Cu vol% calculations. In this way, the Cu amount might be sufficiently less to affect the values of densification for the coated system. Less Cu in theoretical fully dense material represents a higher ρ_{cermet}, leading to a smaller densification (see equation (31)).

Figure 22 (a) shows reinforcing particles composed of grains of different contrasts. The micrograph in (b) shows the same surface, but with a 5º tilting angle, showing that the contrast has changed. EDS spectra were obtained for the points 1 and 2 in Figure 22, to see if the shadings correspond to a contamination. The resulting X-ray diffractions reveal the same peaks for the same materials, with the same area, meaning that the WC particles are composed of different grains with different orientations.

Figure 22 SEM images of monomodal 25WC-75Cu sample with (a) the surface perpendicular to the electron beam and with a (b) 5º tilt to the normal plan; Spot analysis spectrum of point (c) 1 and (d) 2

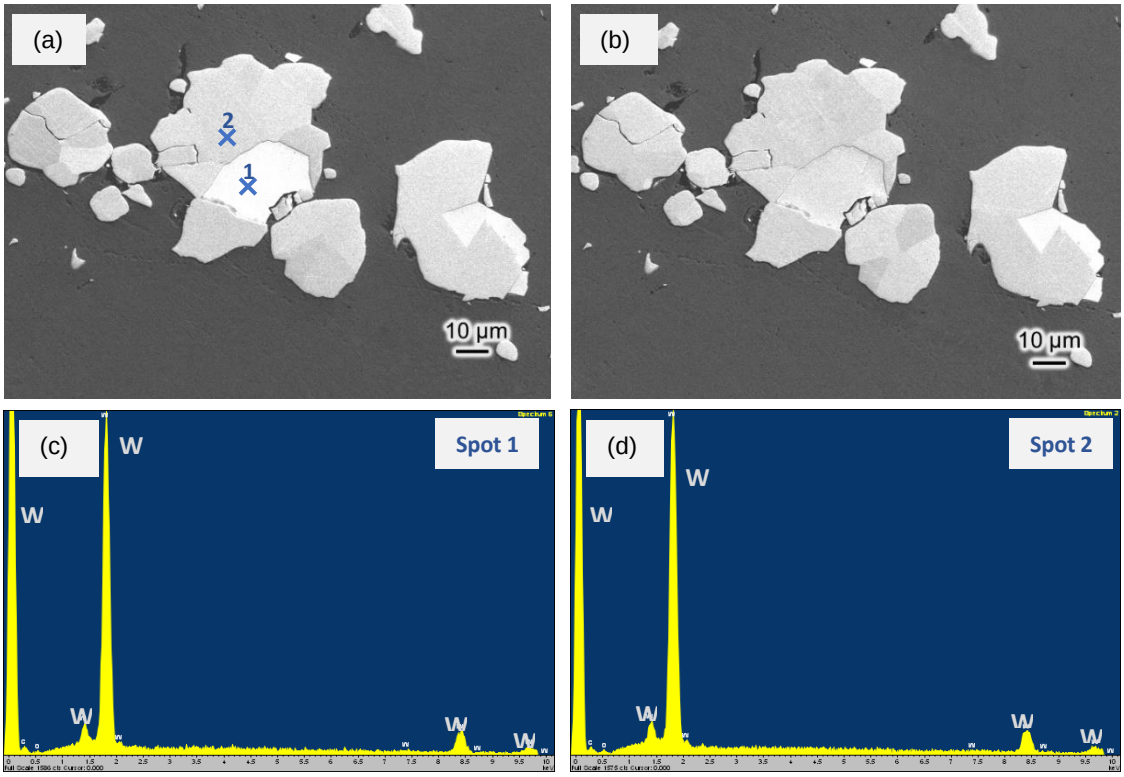

Graded composition

The consolidation of the composite with a graded composition was a preliminary attempt with the goal of understanding the adhesion of the three layers. The densification of the produced FGM is 79%. Figure 23 shows that the three gradient layers are indistinguishable regarding their different composition of 25, 50 and 75 vol% WC.

Figure 23 SEM images of the microstructure of the FGM

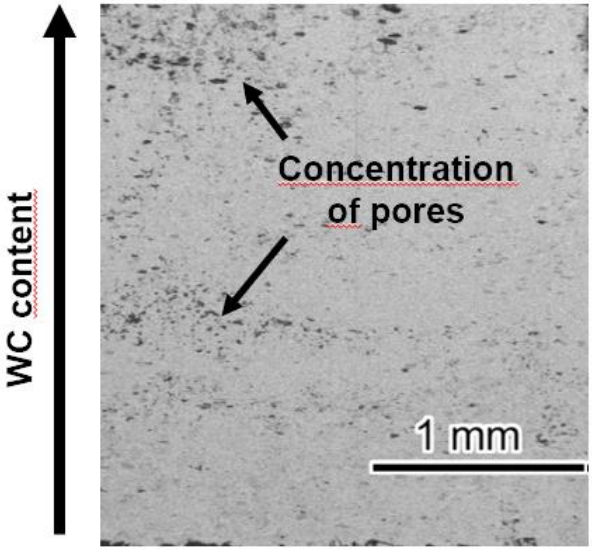

The sintering operation revealed not to be the most indicated, since porosity is mostly located in the diffuse intermediate area. In this way, adding a fine layer of Cu might work to bond the two neighbouring layers [71].

4.2.2 X-ray diffraction

The bimodal class of the consolidated materials were submitted to X-ray diffraction to study the existing components and figure out the possible existence of impurities or compound formation in the structure of the bimodal system composites.

Figure 24 shows the XRD patterns of the experimental diffractograms of the composites with bimodal size dispersion of WC particles with the compositions of 25, 50 and 75 vol% WC, from the top to the bottom. They are plotted together with the theoretical diffractograms of pure Cu and WC.

The crystalline structure of the copper oxide that was more probable to be formed, Cu_2O, was simulated. Finally, taking in consideration that the samples were cold mounted when submitted to X-ray diffraction, the resin alone was also analysed. The mounting material is epoxy resin, a polymeric hardener and a graphite powder.

Figure 24 Merging X-ray experimental diffractograms of the materials 25WC_bi, 50WC_b and 75WC_bi, theoretical diffractograms of pure Cu and WC and the identification of the peaks of the mounting resin (*)

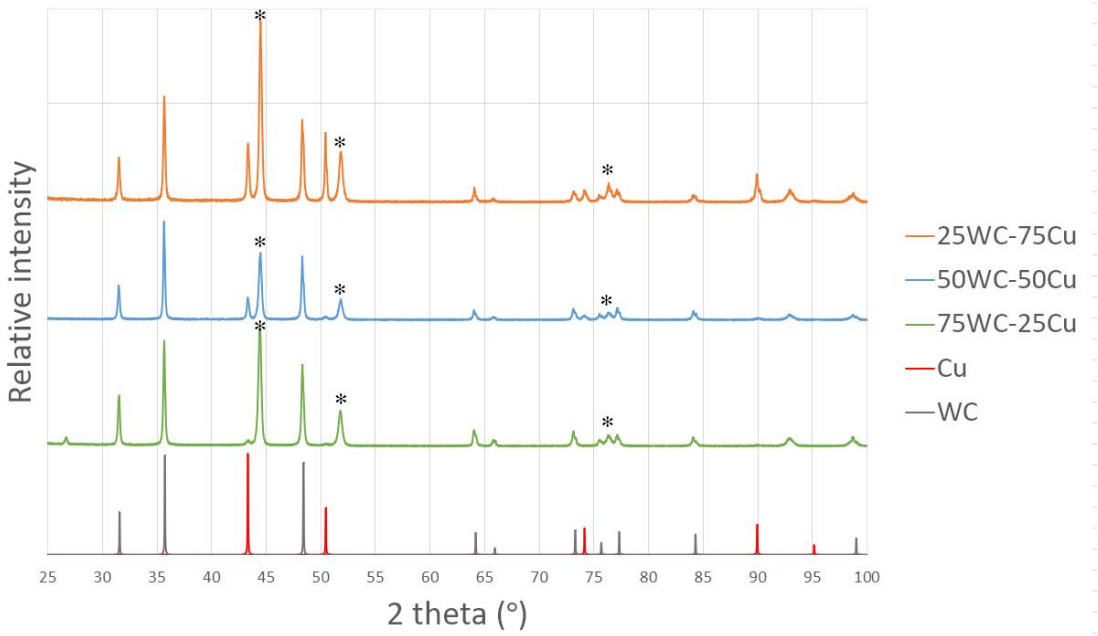

Figure 24 shows the presence of WC and Cu. There are two strong peaks at 2θ = 44 and 52º and other at 2θ = 77º, identified with a * mark. Those are attributed to the graphite powder dispersed in the resin.

4.2.3 Thermal analysis

Given the role of transition layer played by the WC-Cu, the evaluation of their thermal properties and comparison with the neighbouring layers is of major importance.

The temperature dependence of thermal diffusivity was determined for the produced materials. α is dependent upon the processing conditions, as well as microstructural variables, which include the interfaces between materials of different families (ceramic/metal) or between different phases (solid/gas) [41][59]. In this way, α was determined only for samples with a densification above 90%. The samples with an adequate level of densification were, for the bimodal size distribution of WC, the 75WC-25Cu, and for the monomodal one, both 25WC-75Cu and 50WC-50Cu with covered WC particles.

Figure 25 presents the α values of the above mentioned cermets. A higher content of Cu implies a higher α. Their increasing Cu content (25, 50 and 75 vol%) would suggest a similar difference between the thermal diffusivity values. However, the values of α at the same temperature for the three compositions do not vary in the same way. The coated and monomodal system has a α with close values (25 and 50 vol% WC), but the uncoated bimodal system has lower values of α (75 vol% WC). This must be related to the existence of more interfacial area between matrix and reinforcement for the bimodal system, since in the same volume, smaller particles have more surface area than bigger ones, implying a bigger interfacial area when using smaller particles in the system.

These discontinuities exist in a larger quantity for the bimodal system, which is also the composition with the bigger quantity of ceramic particles. Here, the heat flux faces more blocking scenarios: less and thinner copper paths and interceptions with more particles. Meanwhile in the system with coated particles, the presence of large copper regions throughout the microstructure (see Figure 19 (a) and (d)), works as heat flux “high-ways”, easing the heat propagation. The 25WC_mono sample has higher Cu content and lower densification than the 50WC_mono. The heat propagation is faster in the first one, but without a relevant difference.

The α point for the 50 vol% WC at T~300º and 350º was obtain only with one shot, so they are placed only to show the most probable region for the value to be. The plots in detail are in Annex A.

Figure 25 Temperature dependence of thermal diffusivity of the experimental cermets 75WC_bi, and coated 25WC_mono and 50WC_mono obtained by LFT

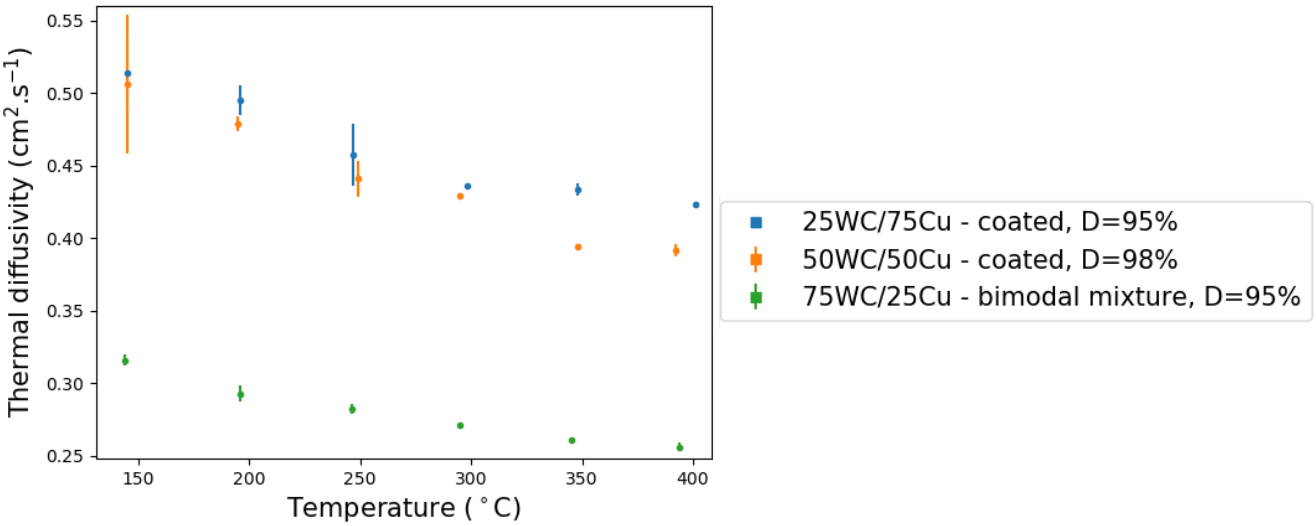

Figure 26 makes the comparison of the thermal diffusivity as function of temperature between the experimental material and the composing materials of the cermets, Cu [72],[73] and WC [74], the materials of the neighbouring layers in the monoblock, W [75] and CuCrZr [76] and the WC-Co [77].

This cermet is the most abundant for engineering applications, having so a broader available data. Its α is presented to refer what thermal behaviour is expected for a cermet.

Figure 26 Thermal diffusivity in function of the temperature for Cu [72],[73]*, CuCrZr* [76]*, W* [75]*, 25 and 50_WC_mono coated, 75WC_bi, WC-Co* [77] *and WC* [74]

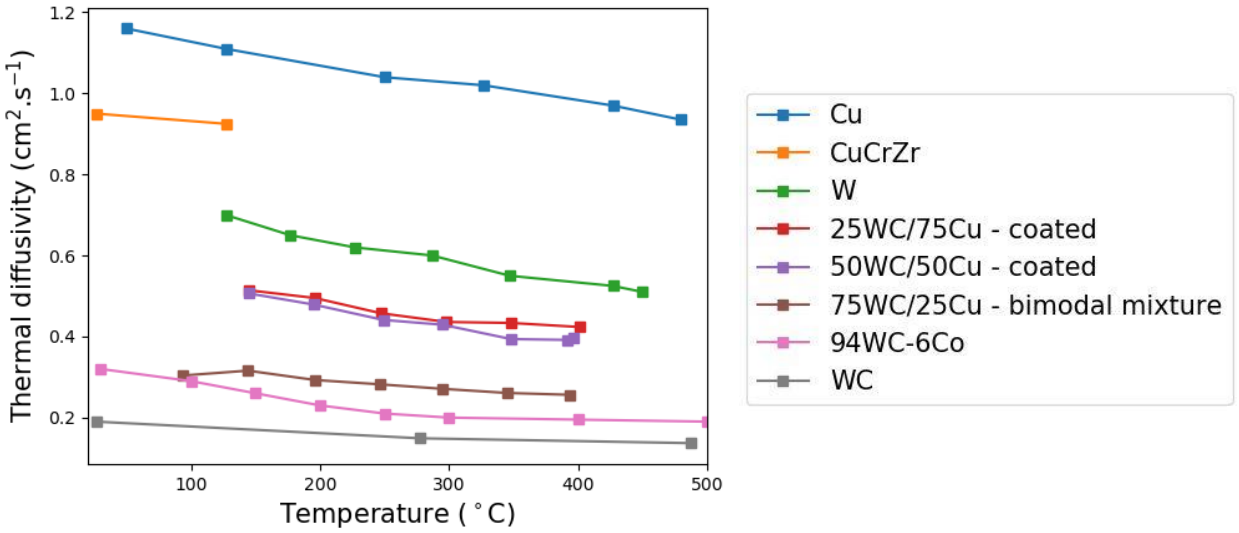

The composition 75WC_bi has the higher content of WC. Hence, its α values are closer to those obtained for WC and WC-Co. They are slightly higher, due to the Cu content, since Cu is a much better thermal conductor than WC and Co.

The slope of the produced cermets is very similar to the WC-Co one: it is steeper until the 350º C and after, the temperature dependence decreases.

For the work presented in Chapter 5 *Modelling*, was necessary to determine the specific heat value for the cermet submitted to the study, which was the 75WC_bi. Values of c_p were obtained for the same temperatures as the α ones: from 100 to 400º C. In this way, is possible to determine the temperature dependence of the thermal conductivity of the same cermet, given by the relation $k(T) = \alpha(T)\rho(T)\, c_p(T)$, mentioned in equation (6) in point 3.1.5 *Laser flash technique*.

Figure 27 (a) presents the thermal dependence of thermal conductivity of the 75WC_bi cermet, Cu [78], CuCrZr [79], W [80] and typical k values of WC-Co [81]. The general tendency is the decreasing of k with increasing temperatures, where the thermal conductivity values for the WC-Cu cermet are slightly lower comparing to similar material: WC-Co. However, the literature [82] shows that k depends on the WC grain size and vol% of Co, where the equation (32) was derived

$$k = 154.989 - 87.7459 * f_{Co} - 65.8092 * \left(\frac{1}{d}\right) \quad (32)$$

where f_{Co} is the cobalt volume fraction and d the grain size. So k for WC-Co is dependent on these factors.

Figure 27 (a) Temperature dependence of thermal conductivity of Cu, CuCrZr, W, WC-Co and produced 75WC-25Cu cermet and; (b) detail of the marked area

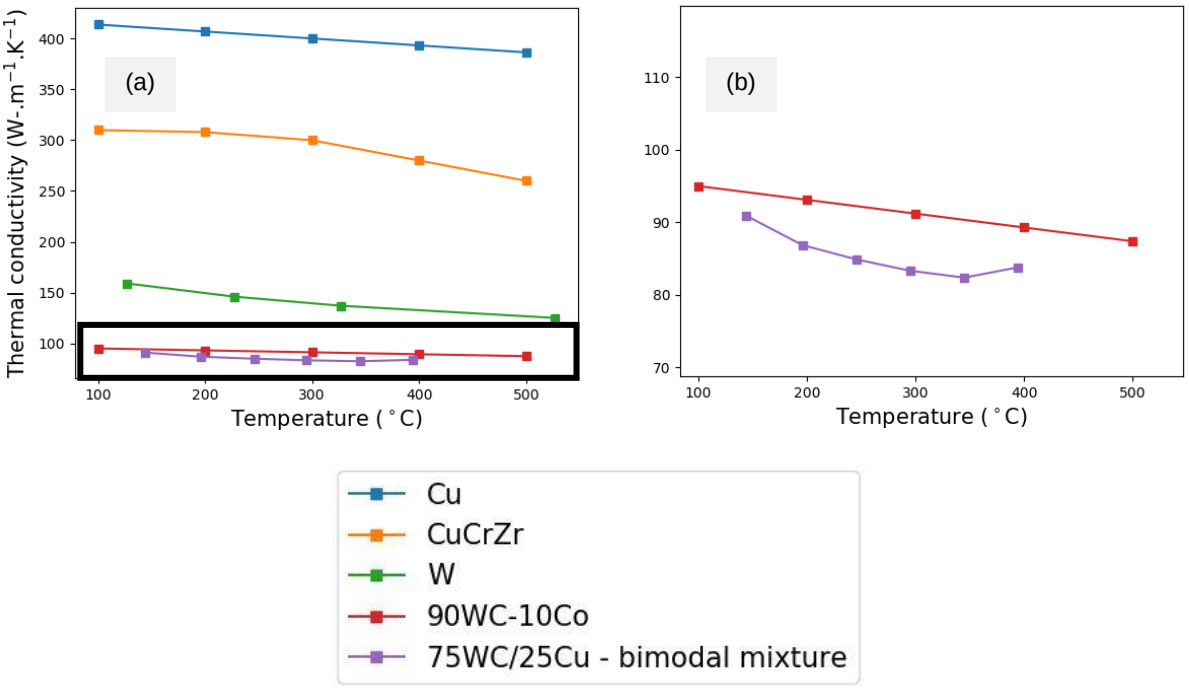

4.2.4 Hardness

Hardness tests were performed in all cermets with the main objective of evaluating the interface bonding strength between reinforcing particles and matrix. Also, the hardness values are presented.

Microindentation marks

Figure 28 shows the material response behaviour when submitted to a Vickers pyramid diamond micro-indenter, applying a force of two kilograms (HV2).

Figure 28 Micrographs of the plastic behaviour resulting from a 2HV indentation in a (a) bimodal cermet with details of (b) of a protruding particle (top) and microploughing (bottom); indentation in a (c) monomodal cermet, with details of (d) a ductile wave (left) and micro-cracking (right)

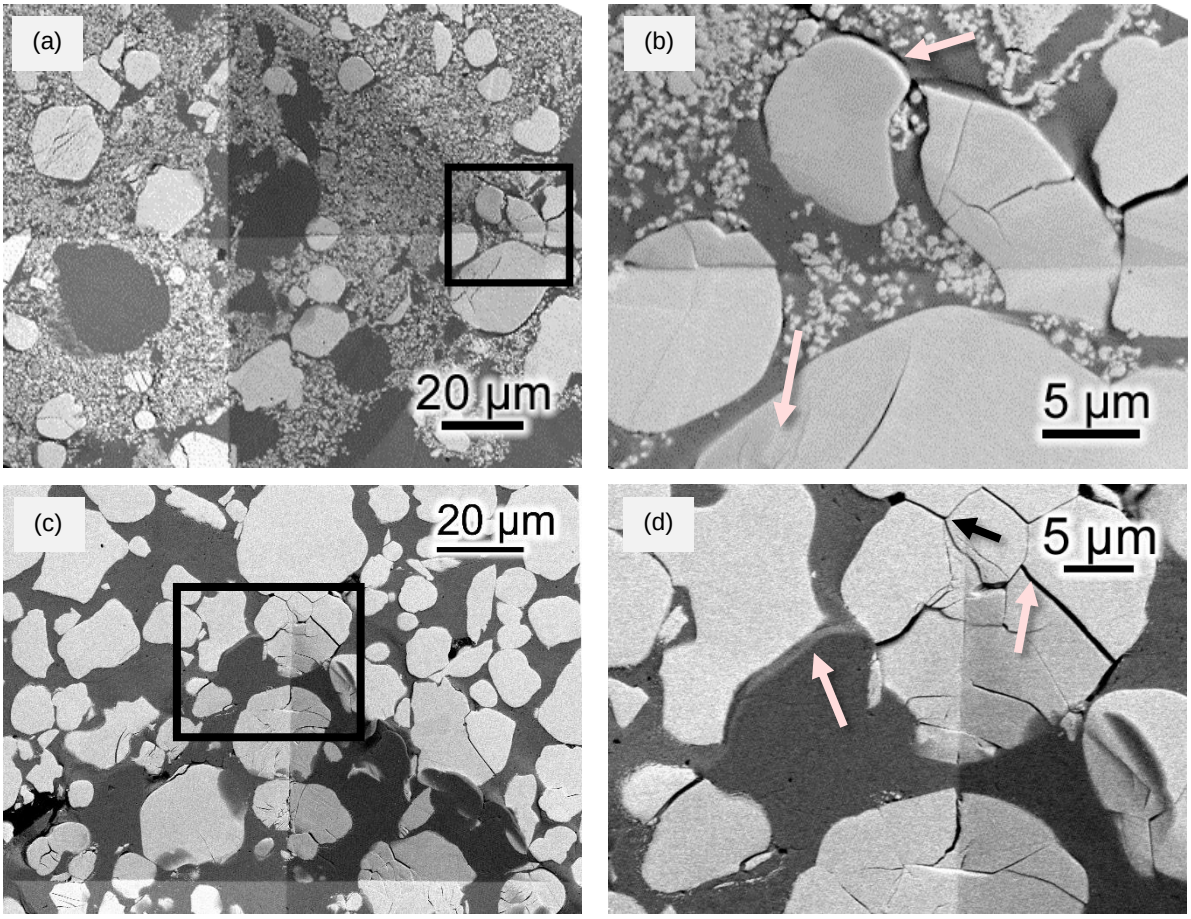

The results indicate that the indentations in the sample with monomodal size dispersion with large particles evidence inter- and intra-granular grain fractures in the brittle phase. Figure 28 (d) shows crack segments that ran along the WC grain boundaries inside a particle (black arrow) and through a WC grain (arrow in the right). Figure 28 (b) shows the occurrence of microploughing in the parallel direction to the applied stress, in the tensile regime (lower pink arrow) and the large particles detachment from the ductile matrix (upper pink arrow).

In the structures having a bimodal distribution (Figure 28 (b)) there are no small particles (1 µm size) detached from the matrix.

The brittle behaviour of the ceramic particles increases with their increasing size, since less ductile material is available to cushion the applied stress. The same phenomenon takes place in the monomodal system, that can be identified in Figure 28.

Hardness measurement

Figure 29 shows Vickers hardness values of the cermets with bimodal and monomodal size distribution, coated or uncoated. This measurement was not proceeded for the poorly consolidated samples (only >75%) since the material absence would compromise the measured hardness [83].

The considered values reflect the hardness of the composites, since the material was indented in representative zones, as the ones in the micrographs with a scale bar of 30 µm, in Figure 16, Figure 19 and Figure 20.

Figure 29 Hardness values of well consolidated cermets as a function of composition in vol% of WC

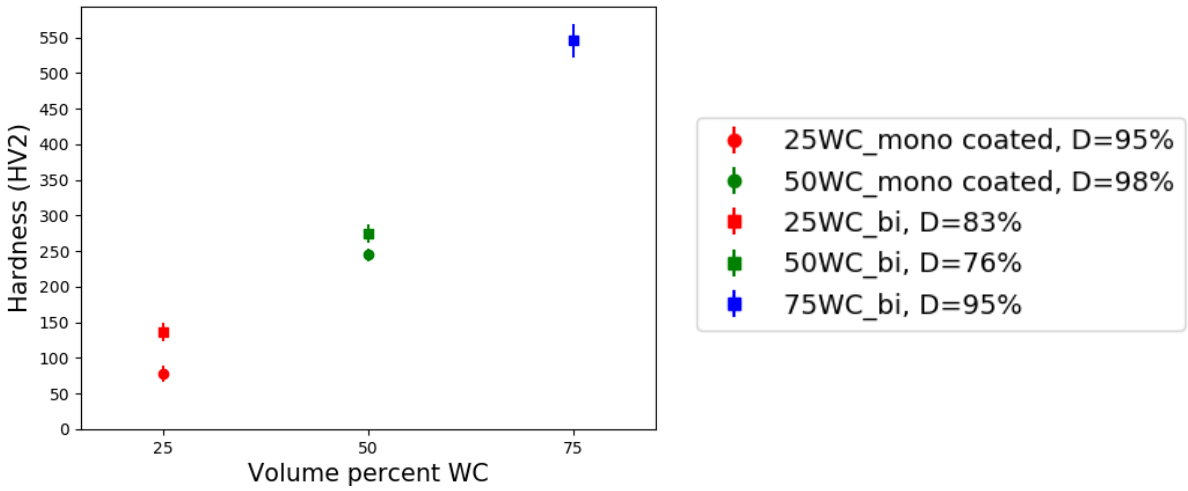

As expected, increasing WC content yields higher hardness values. Comparing the bimodal with the monomodal cermets with the same volume composition, the bimodal system displays higher hardness values for the three compositions. This increase may be due to the stronger pinning effect of reinforcing particles [84], that bear high loads and whose presence obstruct the movement of dislocations, increasing the hardness. This phenomenon might be also related to the wider dispersion of the base material. As the particles distance more from each other in the bimodal system, they hinder the plastic deformation of the overall material in a greater way, comparing to the system having fewer and bigger particles. More interfaces with pores must result in broader hardness values due to the smaller solid volume which is easier to plastically deform. This is reflected in a wider standard deviation, noticed in the hardness values of 75WC_mono uncoated, which is the less dense material.

Chapter 5 Modelling

The modelling work is presented in this chapter.

A representative model of a WC-Cu cermet was developed, with the aim of describing the transient thermal behaviour of this material. Using FEM, the temperature-time (TT) response was obtained on the rear side of the sample and compared to the one obtained in LFT. The effects of adding porosity and radiation emission in the TT behaviour of the mentioned material are also studied.

The study is divided into four sections, which are the following:

1. Model development, where the modelling conditions are defined;
2. Simulation of the temperature evolution of a disk sample subjected to a laser pulse and reproduction of the TT analytical curve. The purpose of this step is to adjust and validate the model and the simulation conditions;
3. Comparison with the LFT experimental results. In this step, the simulation conditions are adjusted in order to fit the experimental results. As a result, a set of modelling conditions are obtained, that represent well the behaviour of the tested materials;
4. Study of the influence of different effects on the behaviour of the curve: porosity and radiation losses. These results allow to understand the importance of these effects on real materials.

5.1 Model development

In this subchapter, the modelling conditions are defined, in order to end up with a simulation of the temperature evolution of a disk sample subjected to a laser pulse. In other words, a simulation of the heat flow in the laser flash test by LFT is done.

The Elmer multi-physics package was the software used in this study. Elmer uses the FEM to solve the equations of interest and comprehends several programs: ElmerMesh, ElmerGUI and ElmerSolver. The input files are the mesh and case files, introduced ahead. The output files are processed to obtain a simple text file containing time and temperature data. Finally, a normalized time-temperature (TT) curve is plotted from data obtained in the central point of the rear side of the sample model.

5.1.1 Mesh file

ElmerGUI imports the mesh file, generating a model with the defined geometry and mesh parameters, that is an approximation of the object to be modelled.

Design

The modelled part has the same dimensions as the sample of 75WC_bi used for the laser flash test. The latter has a shape of a disk, illustrated in Figure 30. Its dimensions are presented in Table 9.

Figure 30 Format of the sample and its radial section

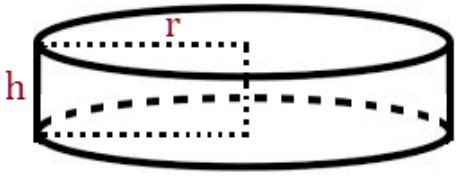

Table 9 Sample structural specifications

Structural specifications		
r (mm)	**h (mm)**	**A_c (mm^2)**
5	2.5	78.54

Model

The resulting 3D model is shown in Figure 31 (a). The heat flow test to be simulated does not require a 3D structure, since the latter is a simple repetition of 2D structures, due to symmetry conditions. Thus, it is possible to obtain the same TT data using a representative 2D model, in a quicker and simpler way. In this way, a 2D model was done, presented in Figure 31 (b). The latter is an infinitesimal slice through the radial direction of the 3D model.

Figure 31 Mesh of the (a) 3D model with the mesh refined in the height direction and (b) 2D model

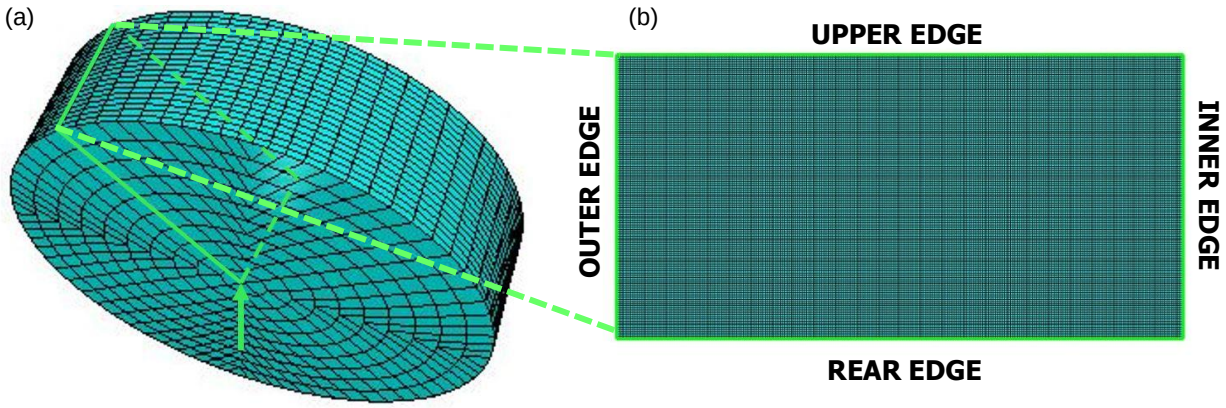

Mesh parameters

Several mesh gradings were used to study the effect of mesh size on the convergence of the solution. The ideal mesh must have a number of surface elements that will guarantee a good solution convergence and a not too long CPU time. Table 10 indicates the parameters used for the meshes

created in two and three dimensions, namely the number of surface elements and nodes, the defined maximum size of an element and the size of the “divisions”. The mesh is divided into subcells called “divisions”. A division is composed of a group of surface elements, and a material is attributed to each division, making it the smallest division object. The user attributes the size of each one. These parameters are entered in the mesh file.

Table 10 Mesh parameters

Parameter	2D	3D
Number of Elements	5000	2800
Nodes	5151	9261
Reference density	0.2 mm	0.5 mm; The density is chosen to be 2x bigger in the heat flux direction, resulting in a more refined grid through this direction*.
Division size	All with the same size; varies from 0.1 x 0.1 to 0.25 x 0.25 mm; depends on the studied case (see Table 18 in point 5.3.3)	1 division with 10 x 10 x 2.5 mm.

* The parameter defining the mesh density ratio between different directions is *Coordinate Ratios*

5.1.2 Solver input file

The software ElmerGUI compiles a solver input file (SIF) that includes the following parameters: the applied equation and its solver method, materials, boundary and initial conditions and the system setup. These will be discussed in the order suggested by the program.

Equation

To obtain a relation between the temperature of a body and time, the heat equation is the equation of interest to activate in the program. Its expression is in equation (8).

ElmerSolver offers different algorithms to solve this, which are discussed in point 5.1.4 *Solver method for the heat equation.*

Initial conditions

The considered initial condition is the initial temperature, T_i. The thermal diffusivity has a representative mean value of T = 667 K, which is the initial temperature of the experimental technique. Thus, the same initial temperature (T_i) was chosen:

- $T_i = 394\,^{o}C\ = 667\ K$.

Material

The domain of simulation is divided, and each division is attributed to one material. New materials can be introduced by the user, with the respective list of properties.

The body material is the produced WC-Cu cermet, designated as 75WC_bi. The choice of this cermet relies on its high level of densification, since the latter was the densest material obtained, at the time of the synthesis of the modelling work. However, the reported material has very complex features in its structure, as the following, previously reported in Chapter 4 *WC-Cu cermets:*

- Cu phase is usually concentrated (formation of copper regions) – WC particles are not uniformly dispersed;
- The standard deviation for the sizes of both particle groups is very large – simulation of different sized particles;
- The shape of the particles is not close to be spherical or rectangular – bad shape approximation;
- The grain sizes comparing to the modelled slab thickness are irrelevant and the amount of them is very big;
- The sample presents a porosity of 5% - presence of three materials (Cu, WC and air).

These characteristics suggest that a direct mesh would be very complex to generate with accuracy. Moreover, the latter would not consider other important parameters, as the interfacial resistance and the heat losses by radiation.

To achieve a structure with the same thermal response as 75WC_bi, the properties of the latter material required by the heat equation, the thermal conductivity k and the emissivity ε, were entered in a new material.

The value of k was obtained through the relation $k(T) = \alpha(T)\rho(T)\,c_p(T)$, mentioned in equation (6) of point 3.1.5 *Laser flash technique*. Its variables are indicated in *Table 11* with the respective mean value and associated uncertainty. The latter is the combination of the uncertainty of the experimental measurement and of the equipment. The variables are assumed to be independent. Thermal conductivity was assumed to be temperature independent since Figure 27 shows a very small temperature dependence of k of the material 75WC_bi and the interval of temperature for the available data does not comprehend the testing temperatures under LFT. The resulting mean value of k is indicated in the end of the table, along with its combined uncertainty, obtained by the rule of propagation of uncertainty. Air at T_i was also included, for the study done in point 5.3.3 *Effect of porosity*. The properties of the added materials are presented in Table 11.

Table 11 Thermophysical considerations for the simulated materials

Material	Property	$\overline{x}$	Uncertainty
WC-Cu cermet: 75WC_bi	**α (m^2.s^{-1})**	2,56E-05	0,16E-05
	c_p (J.kg^{-1}.°C^{-1})	247,9	4
	ρ (kg.m^{-3})	13186,05	5,01
	k (W.m^{-1}.K^{-1})	**83,7**	**5**
Air		**0,0515**	**-**

In this way, the value for thermal conductivity of 75WC_bi is $\boldsymbol{k = 83,7 \pm 5,0}$ **W.m^{-1}.K^{-1}.**

Boundary conditions

The boundary conditions result from the assumptions in LFT, mentioned before in point 3.1.5 *Laser flash technique.* These are indicated in Table 12 along with the corresponding modelling restrictions.

Table 12 Assumptions of LFT important for the boundary conditions

Assumptions	Modelling restrictions
Infinitely short pulse – no heat flow in the irradiated surface after removal of the thermal load	$t_{energy\ application} = 0.001\ s$
Pulse absorption and its uniform distribution in a very thin layer of the specimen	Condition of heat flux constant along the upper edge
Radius of the laser beam equal to the radius of the sample	
Adiabatic conditions	Null heat flux for the non-directly heated faces

The boundary conditions are the following and are illustrated in Figure 32:

Upper edge (↑) - to simulate the heat flux generated when the laser beam strikes the sample, a constant heat flux, $\vec{\emptyset}_q$, is imposed for a $t \leq 0.001\ s$:

$$\vec{\emptyset}_q = \frac{Q}{\Delta t \cdot A_c} = \frac{35}{0.001 \times 7.854 \times 10^{-5}} = 4.46 \times 10^8\ W.m^{-2}$$

where the heat flux is the energy of the laser beam (Q) per unit area (A_c) per unit time (Δt). The values for energy and time are in the working range of the apparatus. However, the accurate determination of the used time and energy is not possible. These are in Table 13.

Outer (←), inner (→) and rear (↓) edge – a zero heat flux is imposed on the simulation conditions for the non-directly heated faces and for the directions non-parallel to the beam:

$$\vec{\emptyset}_q = 0\ W.m^{-2}$$

Figure 32 Illustration of the boundary conditions where q is energy per unit time (Q/Δt)

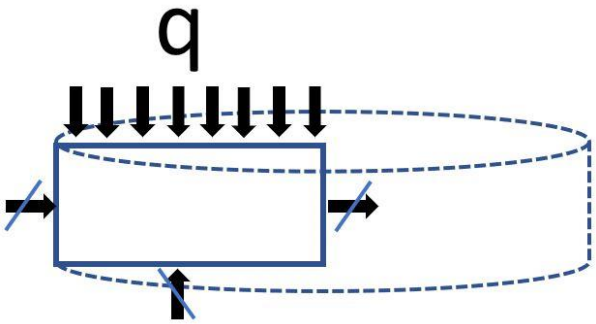

Table 13 Relevant work conditions of the Laser Flash Apparatus, Anter FL – 5000 estimated for the studied sample. Adapted from [61]

LFT general conditions	Value
Laser energy*	~ 35 J
Pulse time*	~ 0,001 s

* parameters considered to be the used ones for the studied sample

5.1.3 System setup

In order to obtain the best fitting to the laser flash experience and also a good solution convergence, the simulation settings must be optimized.

The heat equation involves the temperature varying with the position and time, resulting in a transient state simulation, where the next time iteration depends on the immediately previous computed one.

The time stepping method used is the backward differentiation formula (BDF) with different orders of approximation between 1 and 5.

This method needs a set of parameters to be defined, presented in Table 14 and the chosen values are indicated and justified in Table 15. The setup parameters related to the grid are defined as well. These are self-explanatory.

Table 14 Explanation of the most important parameters not related to the materials

Setup parameters	Definition
BDF	Backward differentiation formula (BDF) is an implicit multistep method allowing the approximation of the derivative of the given function, based on the results of the previous times. The next value of the dependent variable is calculated by taking a weighted average of these multiple previous results based on a Taylor series approximation of the solution. The order refers to the Taylor series approximation A higher order induces more accuracy and stability [85].
Time step Sizes	The size of one timestep
Time step Intervals	The number of timesteps to reach the desired conditions
Output Intervals	The number of time steps between the output of results. A small number implies a curve with more data.
Maximum Output Level	Refers to the quantity of information during simulation.

Table 15 Set up of the parameters for the time method and grid base structure.

Setup parameters	Admitted values	Justification
Simulation Type	Transient	Heat equation involves the temperature varying the position and time
Time stepping method	BDF	The only time stepping method available
Output Intervals	5	A well-defined curve is generated
Timestep Sizes (s	0,001	The laser pulse duration
Timestep Intervals	150	The satisfactory number of timesteps to reach the final temperature stabilization
BDF Order	5	Discussed below
Maximum Output Level	5	Typical value for simple models that uses the heat equation
Coordinate System	Cartesian	Grid with cartesian coordinates, due to quadrilateral divisions
Coordinate Mapping	1 2 3	Allows 1D, 2D and 3D simulations
Post file extension	.vtu	To open the output file in Paraview

A good converging solution and a well-behaved time-temperature curve were obtained, for which the temperature had time to stabilize. The latter two aspects were achieved due to the well-fitted parameters of timestep sizes and intervals, respectively.

The time algorithm BDF has several orders of approximation and Elmer offers to choose between 1 and 5 (see Table 14, first line). The specific formula of the first order of the BDF is the backward Euler method, the second is the Verlet method and the for higher orders is the Runge-Kutta methods [86] For the lower edge of the mesh, its temperature was plotted versus the corresponding time five times with the conditions in Table 15 and boundary conditions, except the BDF order. The five resulting curves are plotted in Figure 33 and their halftime of simulation is pointed on Table 16.

Figure 33 Time vs temperature in the lower edge for the 1st to 5th BDF orders

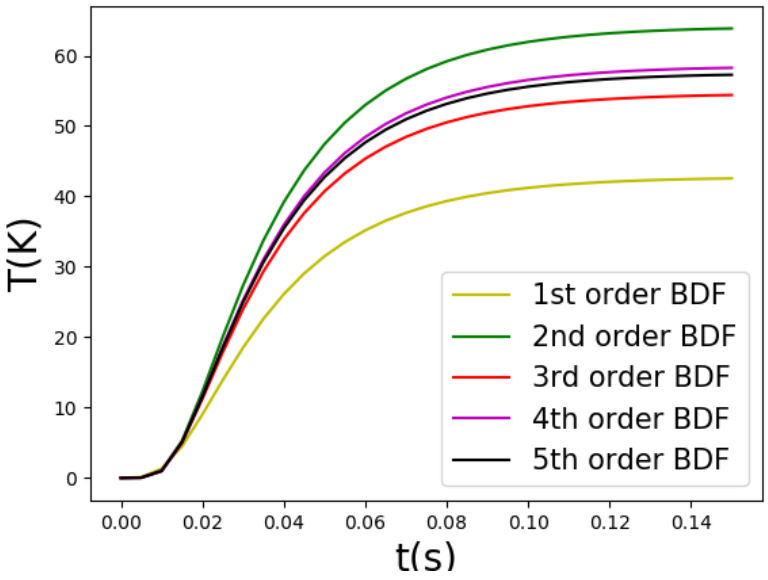

Table 16 BDF order vs halt time of simulation

BDF order	Solver total time (min, s)
1	3' 19''
2	3' 24''
3	3' 26''
4	3' 28''
5	3' 31''

For the first two orders, the convergence is very different from the 5th order. These are not suitable. The fourth and fifth are similar and converge well and the solver time is very close to the times of the lower order BDFs. Hence, the 5th order is chosen.

Kaufmann [59] stated that pulse laser beam duration must be approximately one-hundredth (10^{-2}) of the time needed for the temperature of the rear face to reach 50% ($t_{1/2}$). The $t_{1/2}$ time for the curve with 3rd order BDF corresponds to $t_{1/2} = 3.3 \times 10^{-2}$ s and the pulse of the beam takes 1×10^{-3} s. This results in a ratio of $^{1 \times 10^{-3}}/_{3.3 \times 10^{-2}} = 3 \times 10^{-2}$, where the order of magnitude is the desired one.

5.1.4 Solver method for the heat equation

The solving algorithm for the heat equation used for the previous optimizations was the default one. Nevertheless, the solver has several options for direct, iterative, and multigrid methods, where one should be set for future simulations.

Direct methods are expected to terminate in a finite number of steps, while iterative ones start from an initial guess, forming successive approximations that converge to the exact solution in the limit, only [87]. Multigrid methods are faster but require more memory, so those are used for more complex problems [88]. Iterative methods generate the n-th approximation from the preceding one, so they are

the most appropriate methods. There are seven iterative methods. These were all tested with the same mesh file and solver conditions, except for the solver method. The algorithms “BiCGStabl” and “GCR” did not converge. Among the remaining, all have returned good convergences and very similar convergence times. The method by default, “BiCGStab”, was chosen. The admitted convergence tolerance is 1e-8.

5.1.5 Output data analysis

The output of time and temperature data is normalized under the same normalizing expressions of time and temperature of LFT, expression 21 and 23 of point 3.1.5 *Laser flash technique*, respectively. A V(ω) curve is obtained.

The developed input files, mesh files and corresponding SIF files, are in Annex C to G.

5.2 Model validation

The purpose of this subchapter is to validate the simulation conditions determined in the sub-chapter 5.1 *Model development*. The shape of the obtained modelling curve must be similar and overlapping with the analytical one, obtained by the laser flash test. This will assure that the behaviour of the experimental material is accurately represented.

5.2.1 Reproduction of the TT analytical curve

As discussed in point 3.1.5 *Laser flash technique*, for a laser flash analysis in one-direction only, the equation employed to determine the thermal diffusivity in its dimensionless form is given by:

$$V(\omega) = 1 + 2\sum_{n=1}^{\infty}(-1)^n exp\,(-n^2\omega) \tag{33}$$

Approximations for equation (24) are plotted in Figure 34, considering the dimensionless time ω to range from 0 to 10, which includes the typical values [49], with a step size of 0.1. Different values for the maximum n, n_{max}, were established, to study the curve behaviour and its precise fitting to the analytical curve. Plots were done for n_{max} =2, 4 and 10). n_{max} =10 implies a good approximation to the analytical curve, so that the latter is a suitable value and will be the one used for modelling.

Figure 34 (a) Plot of the analytical solution represented by equation (24) where V= and ω= for n_{max}=2, n_{max}=4 and n_{max}=10; (b) difference detail on the convergence of the solution

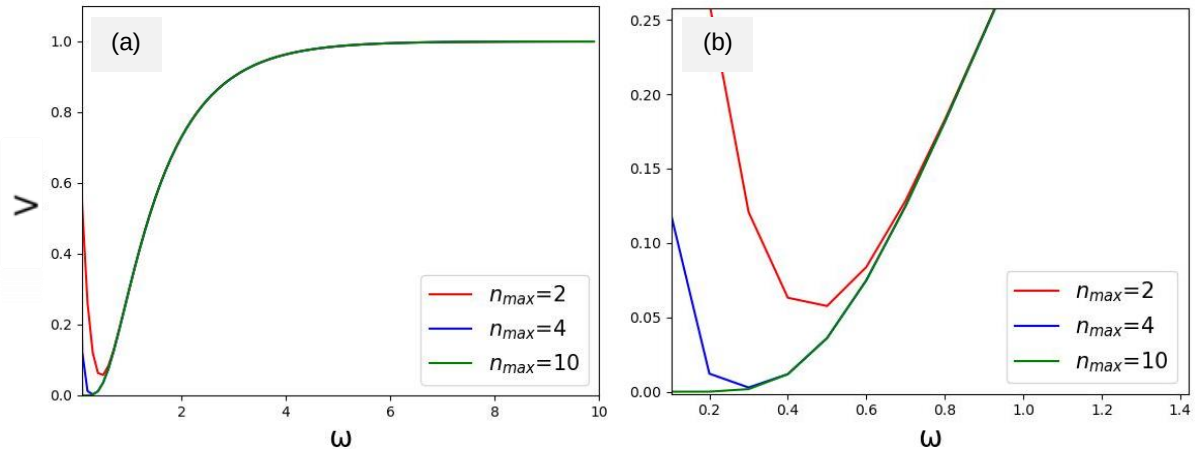

5.2.2 Adimensionalization of experimental and modelling curves

The plots presented in this study are in its adimensional form, regarding the temperature axis, to ease the thermal response comparison. The dimensionless temperature parameter is $V = \frac{T(L,t)-T_i}{T_{L,max}}$, where the maximum temperature is given by $T_{L,max} = \frac{q}{\rho C_p A_c L}$ (deduction in point 3.1.6, sub-section **Governing equations**).

To proceed to time adimensionalization, the value of thermal diffusivity must be calculated, as indicates the time constant $\tau = \frac{L^2}{\pi^2 \boldsymbol{\alpha}}$, which is divided of standard time giving the dimensionless time parameter $\omega = {}^{t}/_{\tau} = \frac{t}{{}^{L^2}/_{\pi^2 \alpha}}$ (deduction in point 3.1.6, sub-section *Governing equations*).The constants necessary for the temperature adimensionalization are resumed in Table 17.

Table 17 Constants for the temperature adimensionalization

$\boldsymbol{\Delta T = T_x - T_i}$	$\boldsymbol{T_i}$ **(K)**	667
$\boldsymbol{T_{L,max} = \frac{Q}{\rho C_p A_c L}}$	$\boldsymbol{Q}$ **(J)**	47
	$\boldsymbol{\rho}$ **(kg.m^{-3})**	13186.05
	$\boldsymbol{C_p}$ **(J.kg^{-1}.°K^{-1})**	247.9
	$\boldsymbol{A_c}$ **(m^2)**	7.854e-5
	$\boldsymbol{L}$ **(m)**	2.5e-3

5.3 Results and discussion

5.3.1 Experimental curve

The analytical curve was fitted to the experimental points obtained by LFT for the 75WC_bi sample, at $T_i = 667\ K$ data. The fitted curve will be used to assess the modelling results. A good overlap of the two curves means that the simulation results would be a good representation of the good material.

The fitting of the analytical curve to the experimental is done by an optimization algorithm from the Scipy library of Python. This algorithm starts from educated guesses of the fitting parameters. For the first fit, a reliable value of $t_{\frac{1}{2}}$ was considered as initial guess, which was extrapolated from the experimental data, seen in Figure 35 (a), in blue. The same plot shows the fitting curve in red, that shows a not good fit in Figure 35 (a), since a displacement in the edges is observed. Based on this first results, a second parameter is included, that represents a shift on the time scale which is another parameter that needs an initial guess to be optimized.

The initial miss-fit in Figure 35 suggests the possibility of a time difference between the temporal evolutions of the temperature of the sample and the temperature recorded by the apparatus. In this way, an increment (∂t) is added to the time factor in the analytical equation (17), where $t \to t + \delta t$. This implies the exponential argument to be

$$\exp(x) \leftrightarrow x = \frac{-0.1388.n^2\pi^2(t+\partial t)}{t_{0,5}}\ or\ \exp(x) \leftrightarrow x = -n^2\ \frac{\pi^2\alpha}{L^2}\ (t+\delta t) \tag{34}$$

For the δt, the initial guess is 0, to consider that no time displacement has really occurred. The returned optimum value for the latter is of -0.0075, suggesting that the measured temperature by the thermocouple is delayed by 0.0075 s (7.5 ms), regarding the time that is set by the apparatus. With this correction, the coefficient of determination (R^2) is 0.9999, proving to be a good fit. The change is noticeable in Figure 35 (b), where a perfect overlap is obtained.

Figure 35 (a) Fitting the analytical curve to the experimental data; (b) with correction factor

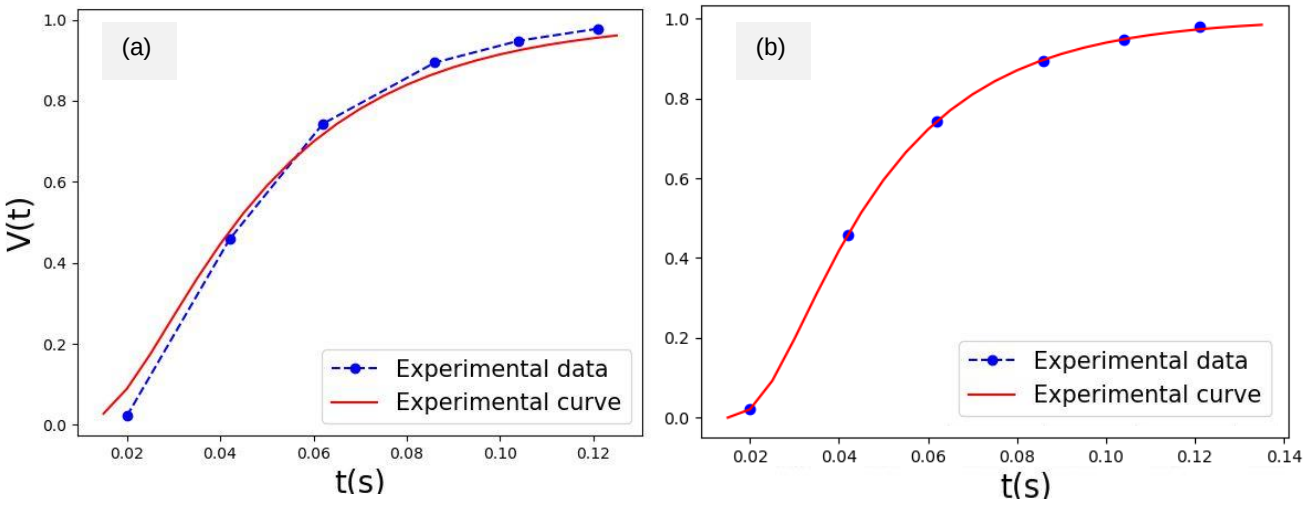

The experimental curve obtained by fitting the analytical expression, plotted in Figure 35 (b) seems to be a good representation of the experimental data. This can be confirmed by comparing the experimental result of α obtained by LFT at $T_i = 667\ K$ and the one resulting from the fitting curve.

The experimental result of α obtained by LFT at $T_i = 667\ K$ has the following average value and standard deviation: $\alpha = 2.562 \times 10^{-5} \pm 0.028 \times 10^{-5}\ m^2.s^{-1}$.

The result of α from the fitting curve, plotted in Figure 35 (b) is determined by equation (26) of point 3.1.5 *Laser flash technique*, $\alpha = 0.1388\frac{L^2}{t_{1/2}}$. The latter depends on the thickness of the modelled slab, L, and the half rise time, $t_{1/2}$. $t_{1/2}$ is directly obtained by Figure 35 (b), where $t_{1/2} = 0.03383\ s$. Thus

$$\alpha = 0.1388\frac{L^2}{t_{1/2}} = 0.1388\frac{(2.5 \times 10^{-3})^2}{0.03383} = 2.56 \times 10^{-5}\ m^2.s^{-1} \quad (35)$$

Finally, the curve in Figure 35 (b) is considered to be an accurate representation of the experimental data, addressed as *experimental curve*.

5.3.2 Standard modelling curve

The simulation conditions for the 3D model originated the thermal behaviour showed in Figure 36, in time, for a total time of 0.15 seconds (150 ms). The temperature in the temperature scale is in Kelvin. In each frame is indicated the corresponding time, in milliseconds.

Figure 36 Thermal behaviour of the 3D model of 75WC_bi under the admitted conditions at (a) 5, (b), 10, (c) 35 and (d) 150 milliseconds

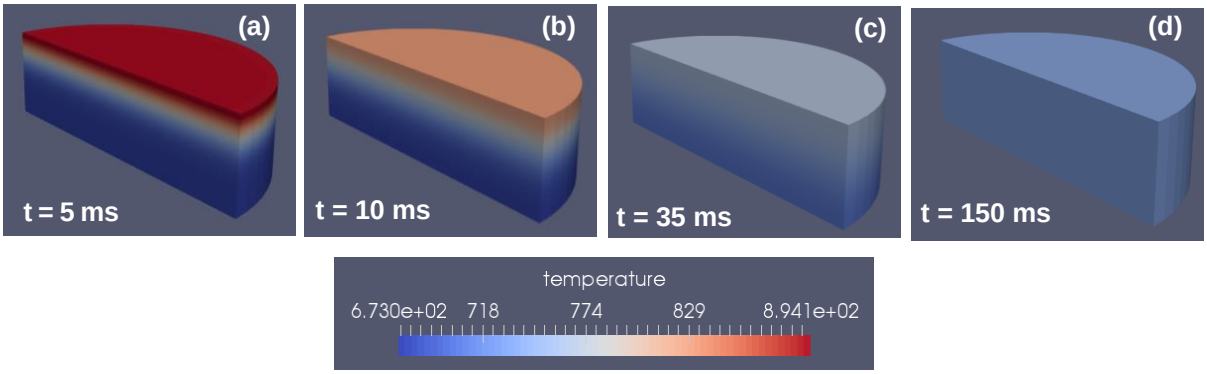

Figure 37 presents the modelling curves resulting of the 2D slab and the 3D disk models. The two models consider the mesh and set up parameters indicated in Table 10 and Table 15, respectively. The curves perfectly overlap, meaning that the 2D model can be used from now on and will be referred as *dense model curve.*

Figure 37 Modelling curves for 2D and 3D models

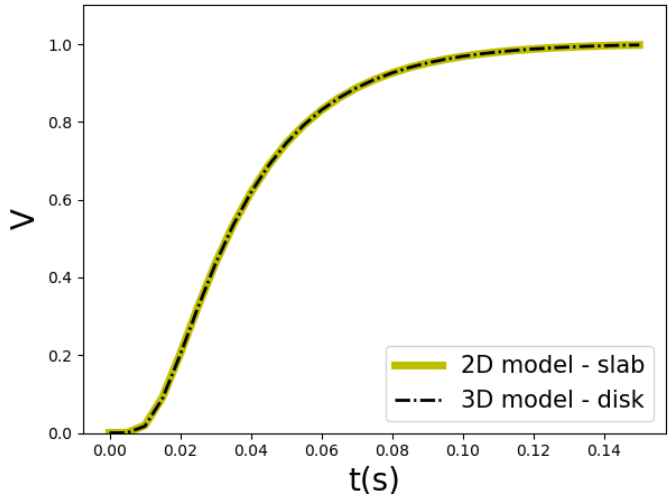

Figure 38 is the $V(t)$ curves resulting of the thermal behaviour demonstrated in Figure 36, coupled with the experimental curve obtained in point 5.3.1 *Experimental curve*. There are three dense model curves due to the uncertainty associated to the obtained value of $\bar{k}$ of the body material, where they correspond to $\bar{k} + error$ and $\bar{k} - error$, respectively and are indicated in Table 11. The value for thermal conductivity of the considered material,75WC_bi, is $k = 83.7 \pm 5.0$ W.m^{-1}.K^{-1},. The average modelling curve seems to successfully overlap the experimental curve. Its corresponding $t_{1/2}$ is 0.03379 s, giving $\alpha = 2.567 \times 10^{-5}\, m^2.s^{-1}$, so the average dense model curve can be used for future thermal studies of the present material.

Figure 38 Modelling curve for the 3D model coupled with the experimental curve

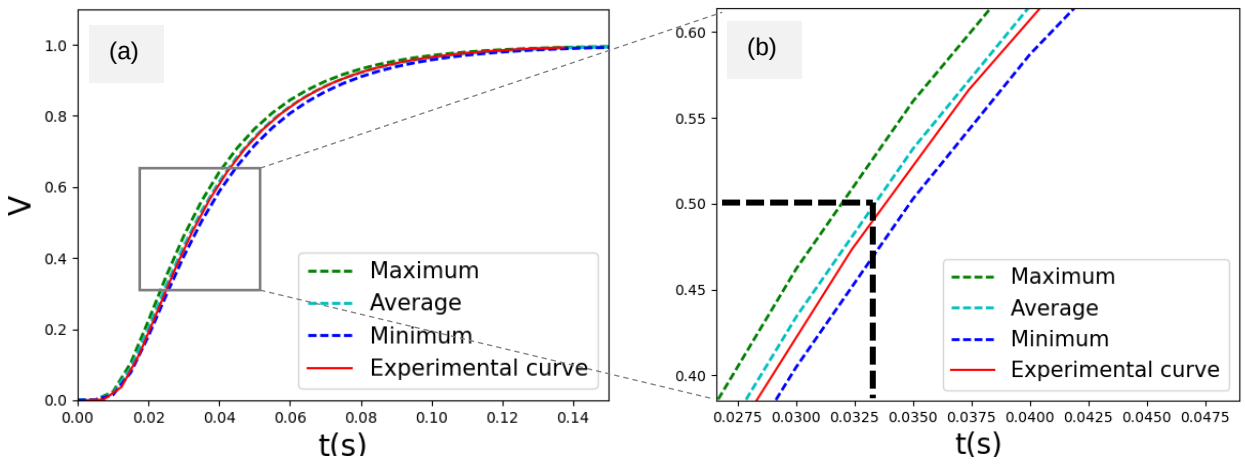

Having the value of α, the normalization of the time axis can be proceeded (see point 5.2.2 *Adimensionalization of experimental and modelling curves*). The dimensionless $V(\omega)$ curve resulting of the thermal behaviour of the dense model is presented in Figure 39.

Figure 39 Dimensionless curve of the dense model

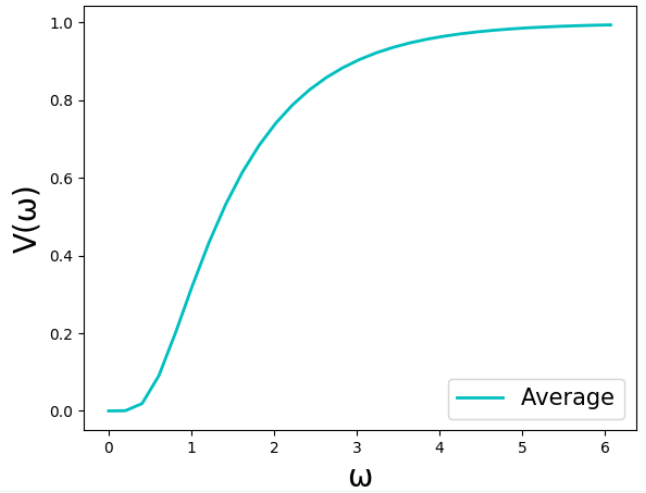

5.3.3 Effect of porosity

After an accurate model is obtained for the 75WC_bi, the effect of porosity is analysed. This can be easily done by introducing a second material to the library of materials and to the mesh file, that will be air.

Homogeneous distribution of pores

Homogeneously dispersed pores with big, medium and small sizes in a matrix of 75WC_bi are modelled.

The area of pores in the 2D model is 5% out of the total area. The possible shapes of the mesh divisions are squares or circles. The previous study was done with squared pores in order to obtain the maximum contact regions with the pore material, within the allowed conditions. The size of the pores varies between big, medium and small pores. Table 18 indicates the mesh specifications and the number of pores that comes from it. Figure 40 shows the resulting meshes for the three variations.

Table 18 Specifications of the mesh divisions for the three cases and resulting number of pores

Number of divisions	Size of one division (10^{-1}mm)	Division shape	Area of pores (%)	Number of pores
$20 \times 10 = 200$	2.5	Squared	5	10
$40 \times 20 = 800$	1			40
$50 \times 25 = 1250$	1			63

Figure 40 Modelled part with (a) 10 pores, (b) 40 pores and (c) 63 pores with the indication of the measurement point of T in the rear face

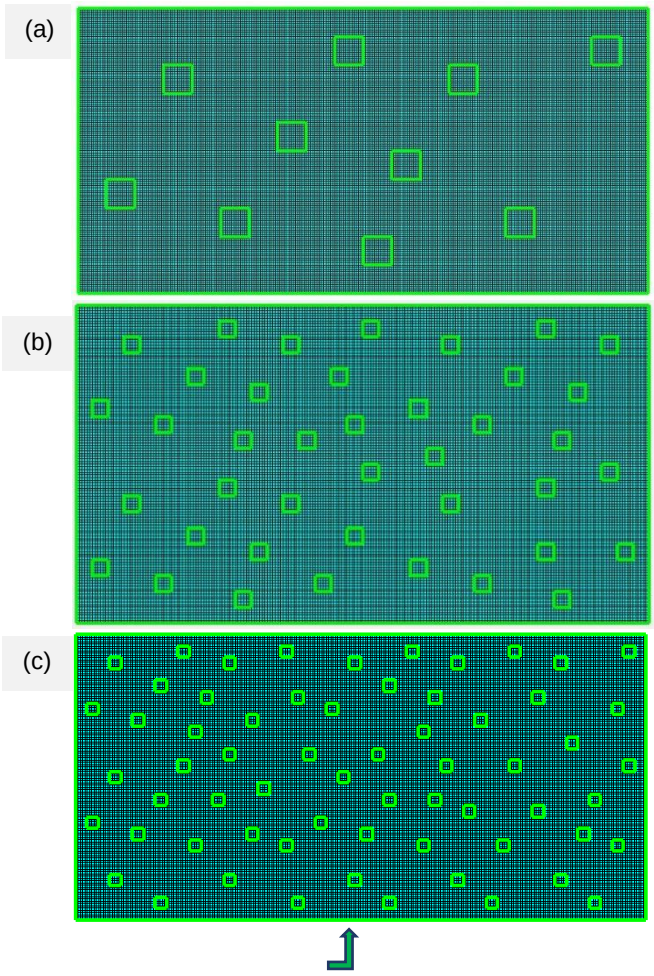

Table 19 presents the resulting α values of the three porous structures, and of the dense material. Values of α for the medium and small pores system show the same result, whereas for the big pores case, the average value of α decreases. The thermal diffusivities of the porous system are lower than the dense one, as expected. Adding pores offers more resistance to the heat flux, since the pores material is air, having a thermal conductivity with three orders of magnitude smaller than the matrix (10^{1} vs 10^{-2}).

The similar values of α for the small and medium pores system might be related to the similar distance at which the first pores are located from the surface, represented in Figure 41.

The system in the middle has medium-sized pores, so, in 1D, the heat flux travels a greater distance through pores material than in the small pores system. However, the first pore is the closest to the surface comparing to the one in the small pores system ($\Delta\ell_m < \Delta\ell_s$). Hence, one effect seems to compensate the other and the resulting thermal diffusivity does not vary. In conclusion, the distance in the direction of the heat flux between the surface and pores has a relevant effect on temperature rise in the rear face, which is measured in the corresponding latitude indicated by the X mark, in the figures.

Even though $\Delta\ell_b$ is the biggest distance, the heat flux travels through bigger pores, roughly with the double length of the small pores, resulting in the lowest thermal diffusivity value.

Table 19 Half rise times and thermal diffusivity values for dense and porous models

Material	$t_{1/2}$ (s)	α ($m^2.s^{-1}$)
WC-Cu w/ big pores	0.03594	2.414×10^{-5}
WC-Cu w/ medium pores	0.03487	2.488×10^{-5}
WC-Cu w/ small pores	0.03487	2.488×10^{-5}
Dense WC-Cu	0.03379	2.567×10^{-5}

Figure 41 Distance from the upper face to the first pore, aligned to the T measurement point (X mark) for the model with medium (left) and small (right) pores

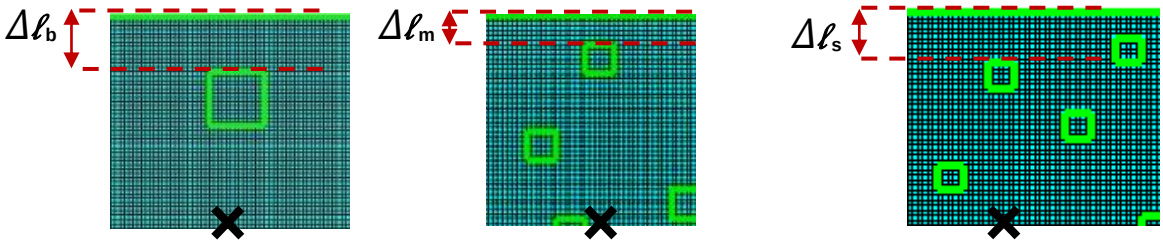

Non-homogeneous distribution of pores

The non-homogeneous distribution of pores along the slab is now studied. The system with big pores is the one used. In the previous study, a small distance between the heat exposed face and the pores seemed to influence the results. Thus, a variation of the distance is now analysed.

Figure 42 presents two different distributions of the porosity. In (a) they are concentrated and close to the heat source and in (b) the pores are also concentrated, but in a more distant position. The arrangement of the pores is mirror-like between the two situations, to have the same amount of contact regions at the same distance to the edges.

Figure 42 Modelled part with 10 pores (a) close and (b) distant to the heat source

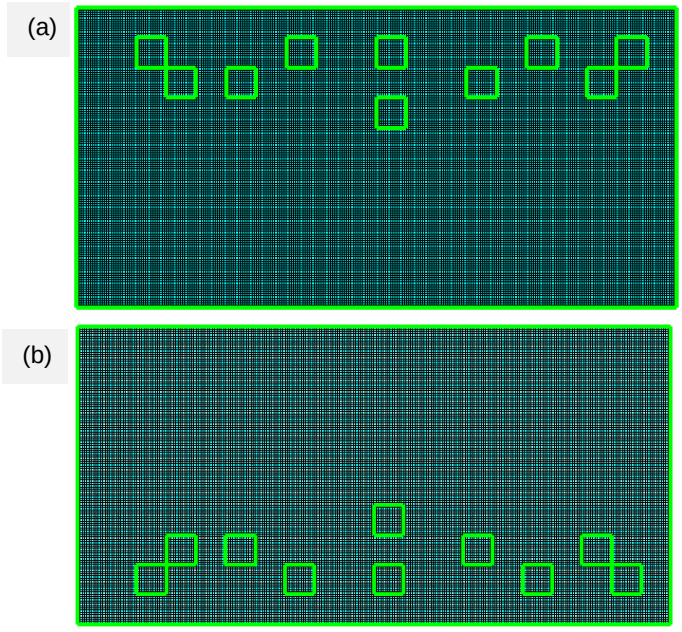

The thermal response of the mentioned models is in Figure 43, where the curves are easily distinguishable, except for the uniform and far away pores distribution. The curve corresponding to the concentrated pores close to the upper face has a temperature rise much slower than the others, since the temperature takes more time to stabilize. This results in a lower value of α. For the system with pores distributed away from the heat source, the behaviour is similar to the case with a uniform distribution, since they have the exact same distance between the upper face and the first pores.

The thermal diffusivities of the models with structures with pores close and away from the heat source are presented in Table 20, in comparison to the structure with a homogeneous dispersion of pores and to the dense model.

Figure 43 Modelling curves for the big sized pores structure with uniform and concentrated pores distribution, coupled with the dense model curve

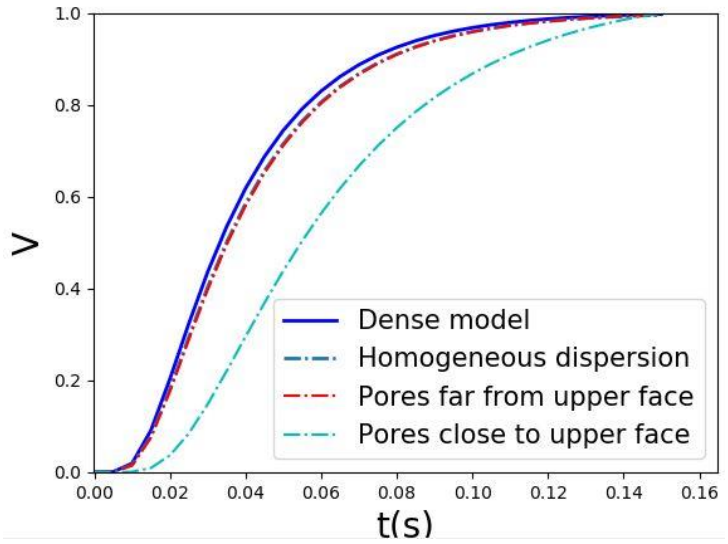

Table 20 Half rise times and thermal diffusivity values for models with structures with pores close and away from the heat source and for the model with uniform pores distribution and dense model

Material	$t_{1/2}$ (s)	α ($m^2.s^{-1}$)
Pores close to the heat source	0.05444	1.565×10^{-5}
Pores far from the heat source	0.03524	2.419×10^{-5}
Uniform dispersion	0.03594	2.414×10^{-5}
Dense WC-Cu	0.03379	2.567×10^{-5}

Nield *et al.* [89] stated that the resulting thermal conductivity of porous media depends on the phases fashion, where for parallel occurrence, k is closer to the weighted arithmetic mean of the conductivities of the solid and gas phases, k_s and k_g, which is $k_A = (1-f)k_s + fk_g$ (Figure 44 and Figure 45). For structures having pores in series, the heat conduction will take place in series, so the overall conductivity is the weighted harmonic mean of the two phases, expressed as k_H, where $1/k_H = (1-f)/k_s + f/k_g$ (Figure 46). The difference of the thermal behaviour resulting from the different arrangement of the pores, at the same height, was not found to be meaningful.

Figure 44 Pores connected by one vertex

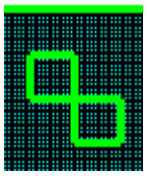

Figure 45 Separated parallel pores

Figure 46 Pores placed in series

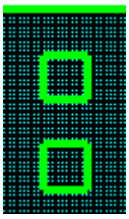

5.3.4 Effect of radiation losses

Another possible studied source of error is the heat losses. The Stefan-Boltzmann Law expresses the heat loss by radiation, per unit time, q, from the heated surface to its cooler surroundings, given by equation (36)

$$q = \varepsilon \sigma (T_b^4 - T_s^4) A_c \quad (36)$$

where ε is the emissivity, representing the ratio of the emitted radiation from the material surface, σ is the Stefan–Boltzmann constant (5.67×10^{-8} W.m^{-2}.K^{-4}) and T_b and T_s are the absolute temperatures for the body and surroundings. If the surrounding temperature is the same for the body, the heat loss by radiation is null, justifying the stabilization of the initial temperature proceeded before each laser strike. The following assumptions are considered: the boundaries are insulated, and the sample does not loose heat by conduction. However, some radiation losses may occur and thus the emission might not be the unit.

To consider the effect of radiation losses under LFT, models were analysed with radiation boundary conditions. In this step, emissivity values of 0.9 and 0.8 were considered on the upper, inner and outer faces, taking in consideration the typical WC emissivity ($\varepsilon_{WC} = 0.85$) [90]. The study was done for dense models. The resulting solutions are indicated in Figure 47. There is showed that the difference among the considered values of emissivity is negligible, where the $t_{1/2}$= 0,03599 s, corresponding to $\alpha = 2.4104 \times 10^{-5}\ m^2.s^{-1}$.

Figure 47 Modelling curve of the dense model, considering surface emission of radiation

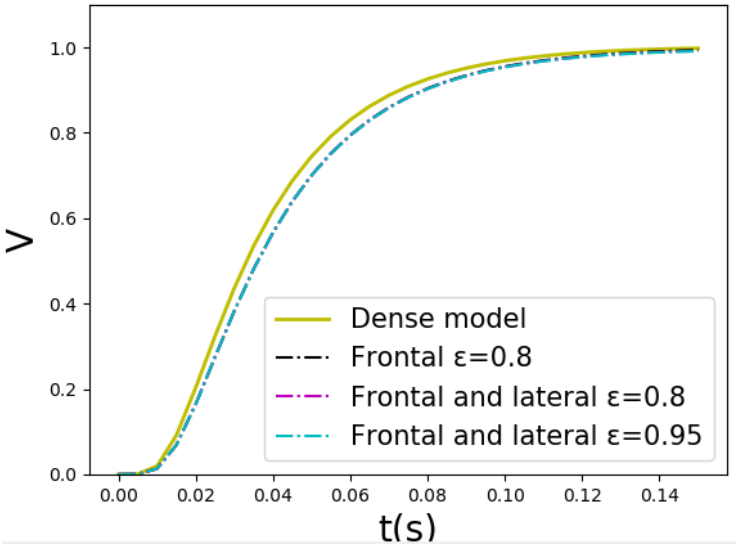

The emissivity effect is found to be less meaningful than the porosity, where the latter has very demarcating effects, namely the localization of the pores regarding the heat source localization.

This page was intentionally left blank

.

Chapter 6 Summary

In this final chapter, the conclusions of the experimental and modelling works are summarized. Suggestions for future work are presented.

6.1 WC-Cu cermets

WC-Cu cermets were produced via liquid state sintering, by hot pressing, with compositions of 25, 50 and 75 vol% of WC. Micrometric powders of WC and Cu (37 µm) were used, where the reinforcement phase was either composed by a bimodal dispersion (1+18 µm) or a monomodal one (18 µm). For the last system the particles were pre-coated.

Due to insolubility between WC and Cu, only adhesive forces are present in the produced composites. The obtained high densification for some of the specimens, above or equal to 95%, was attributed to the capillary force, in the bimodal system. For the monomodal system, high densification occurred due to the faster wetting of the coated WC particles by the matrix, where the same material constitutes both the coating layer and the matrix. However, the majority of samples did not achieve a densification in the higher than 95 %, since the sintering cycles were not adapted to liquid phase sintering. Cermets with a copper-rich composition (25 and 50 vol% WC) struggled to properly consolidate, since copper drained out of the mould, probably due to the high-pressure application (above 22 MPa) combined with the small quantity of WC particles functioning as pinning points to hold the flow of liquid copper. Moreover, this result can be also justified by the large difference between the Cu (37 µm) and the WC particle sizes (1 and 18 µm) that allowed the formation of large Cu regions. The same phenomenon was verified for all the materials with monomodal size dispersion of WC uncoated particles and for the coated system with 75 vol% WC. In the latter, the real amount of Cu present as coating layers must have been lower than the admitted value and, as consequence, the added Cu was not enough to bind the reinforcing particles and achieve a proper consolidated sample.

The results suggested that small sized particles allow a broader coverage of the reinforcing phase throughout the specimen, resulting in increased bulk hardness, where the particles are displaced in the plastically deformed matrix instead of fracturing. On the other hand, particles with a smaller size imply a bigger interfacial area, where the pores tend to allocate.

The Cu coating layer revealed to have a significant impact in increasing the thermal conductivity, due to the decrease in the thermal resistance between WC large particles and Cu matrix. In this way, the formation of pores at the interface was hindered. Moreover, micrographs showed the lower agglomeration of reinforcing particles for the coated system in comparison to both uncoated systems. Particle agglomeration represents a weaker region in the mechanical point of view.

The use of magnetron sputtering to cover the WC particles presented a limitation, since particles with a smaller size than 10 µm have more problems of sticking and cluster formation, hindering the coating process [91]. However, the use of smaller particles does improve the hardness and the adhesion between the matrix and the reinforcing phase, since there is a larger interfacial area in small singular

portions (more anchor points), which are desired features. The composite with a graded composition is at a preliminary stage, where three aspects would need to be studied, namely the pre-sintering of the three sub-layers, their bonding with a fine layer of copper and also the revision of the sintering parameters. These features are suggested for future work.

WC-Cu cermets were envisioned to have lower values of thermal diffusivity than the delimiting layers, W and CuCrZr, which was accomplished. The successfully consolidated cermets have roughly the following thermal diffusivities at 145º C, comparing to W and CuCrZr:

$$0.5(\alpha_{mono}) < 0.7(\alpha_{W}) < 0.9(\alpha_{CuCrZr})\ cm^2.s^{-1}$$

In this way, the WC-Cu cermets are considered to be good candidates to be the content of the interlayer in the next divertor to build, if the neighbouring layers will be CuCrZr and W.

As future work, the sintering maximum pressure of the monomodal system should be revised, since sintering in the liquid phase does not require great pressure applied in the flat contact areas to achieve consolidation [92]. Further characterization of the cermets is required to qualify these materials as interlayer candidates. Properties of interest would be CTE, determined by a dilatometer and Young's modulus which can be determined by tensile tests. The energetic neutrons (14 MeV) resulting for the fusion reaction inside the reactor can penetrate the plasma facing layer and achieve the interlayer. Therefore, neutrons can be simulated using Ar+ irradiation using ion beam techniques.

6.2 Modelling

The thermal behaviour of a WC-Cu cermet was modelled, and simulations tested until the thermal diffusivity and the time-temperature relation were found to be the same of the experimental samples, indicating the best representation of the material by the model. This was achieved, but with a time misfit of 7.5 ms. This time deviation seems to be related to a delay of the measured temperature by the thermocouple in comparison to the beginning of time recording by the apparatus. In addition, the effects of porosity and radiation losses were analysed.

The simulation parameters were optimized to obtain the temperature rise behaviour in the rear face of a specific material, with a known thickness and energy duration of the heat source. In this way, this study works as a preliminary phase of the thermal analysis of a material submitted to a thermal load.

The study of the porosity in the current work showed that producing specimens with porosity can be a way of delaying its thermal response, and that their localization is important to this feature. During a thermal test procedure, the emission might not be total. In this way, lower values of emissivity, 0.8 to 0.95 were assumed. The temperature measurement was negatively affected. In this way the use of the correction factor is important, due to the problem of loss of emissivity.

As future work is suggested the study of the thermal and stress analysis of a complete slab of the monoblock in the divertor, whose outer layer is directly under a thermal load. This should allow the study of structural variations that would lead to a most fitting thermal behaviour for the interlayer, inside the whole monoblock unit, in order to expose the neighbouring layers only at their working temperature ranges.

Chapter 7 References

[1] S. Zinkle, “Advanced materials for fusion technology,” *Fusion Eng. Des.*, vol. 74, no. 1–4, pp. 31–40, 2005.

[2] D. M. Duffy, “Fusion power: a challenge for materials science,” *Philos. Trans. R. Soc. A Math. Phys. Eng. Sci.*, vol. 368, no. 1923, pp. 3315–3328, 2010.

[3] “ITER - Tokamak,” 2017. [Online]. Available: https://www.iter.org/mach/tokamak. [Accessed: 09-Oct-2017].

[4] P. Norajitra, “Divertor Development for a Future Fusion Power Plant,” Karlsruher Institut für Technologie (KIT), 2011.

[5] S. J. Zinkle, “Applicability of copper alloys for DEMO high heat flux components,” *Phys. Scr.*, vol. T167, no. T167, p. 14004, 2016.

[6] G. Pintsuk, S. E. Brünings, J. E. Döring, J. Linke, I. Smid, and L. Xue, “Development of W/Cu-functionally graded materials,” *Fusion Eng. Des.*, vol. 66–68, pp. 237–240, 2003.

[7] M. Li, E. Werner, and J. H. You, “Fracture mechanical analysis of tungsten armour failure of a water-cooled divertor target,” *Fusion Eng. Des.*, vol. 89, no. 11, pp. 2716–2725, 2014.

[8] T. R. Barrett *et al.*, “Enhancing the DEMO divertor target by interlayer engineering,” *Fusion Eng. Des.*, vol. 98–99, pp. 1216–1220, 2015.

[9] A. Hasegawa, M. Fukuda, T. Tanno, and S. Nogami, “Neutron Irradiation Behavior of Tungsten,” *Mater. Trans.*, vol. 54, no. 4, pp. 466–471, 2013.

[10] V. Philipps, “Tungsten as material for plasma-facing components in fusion devices,” *J. Nucl. Mater.*, vol. 415, no. 1 SUPPL, pp. S2–S9, 2011.

[11] M. Galatanua, M. Enculescua, G. Ruiua, B. Popescua, and A. Galatanu, “Cu-based composites as thermal barrier materials in DEMO divertor components,” 2014.

[12] M. Li, M. A. Sokolov, and S. J. Zinkle, “Tensile and fracture toughness properties of neutron-irradiated CuCrZr,” *J. Nucl. Mater.*, vol. 393, no. 1, pp. 36–46, 2009.

[13] J. H. You, “Copper matrix composites as heat sink materials for water-cooled divertor target,” *Nucl. Mater. Energy*, vol. 5, pp. 7–18, 2015.

[14] J. H. You *et al.*, “Conceptual design studies for the European DEMO divertor: Rationale and first results,” *Fusion Eng. Des.*, 2015.

[15] J. H. You *et al.*, “European DEMO divertor target: Operational requirements and material-design interface,” *Nucl. Mater. Energy*, vol. 0, pp. 1–6, 2015.

[16] D. Hancock *et al.*, “Testing candidate interlayers for an enhanced water-cooled divertor target,” *Fusion Eng. Des.*, vol. 98–99, pp. 1323–1327, 2015.

[17] J. Ruokolainen, P. Raback, M. Zenker, and V. Savolainen, *Elmer Models Manual*. 2016.

[18] M. Dias *et al.*, “WC-Cu thermal barriers for fusion applications: thermal and mechanical characterization,” *Surf. Coatings Technol.*, 2017. [Submitted]

[19] F. Guerreiro, “WC-Cu cermet materials : production and characterization,” Universidade de Lisboa, 2015. [Master thesis]

[20] J. M. Molina, E. Piñero, J. Narciso, C. García-Cordovilla, and E. Louis, “Liquid metal infiltration into ceramic particle preforms with bimodal size distributions,” *Curr. Opin. Solid State Mater. Sci.*, vol. 9, no. 4–5, pp. 202–210, 2005.

[21] I. Ibrahim, “Particulate reinforced metal matrix composites - a review,” *J. Mater. Sci.*, vol. 26, pp. 1137–1156, 1991.

[22] Z. Zhou, J. Du, S. Song, Z. Zhong, and C. Ge, “Microstructural characterization of W / Cu functionally graded materials produced by a one-step resistance sintering method,” *J. Alloys Compd.*, vol. 428, pp. 146–150, 2007.

[23] A. S. Kurlov and A. I. Gusev, “Tungsten Carbides and W – C Phase Diagram,” *Inorg. Mater.*, vol. 42, no. 2, pp. 121–127, 2006.

[24] P. R. Subramanian and D. E. Laughlin, “Copper-Tungsten,” in *Phase Diagrams of Binary Tungsten Alloys*, 1991, pp. 76–79.

[25] H. Okamoto, M. E. Schlesinger, and E. M. Mueller, Eds., “Binary Alloy Phase Diagrams,” in *ASM Handbook Volume 3: Alloy Phase Diagrams*, ASM International, Materials Park, 1982, pp. 79–624.

[26] H. Ibrahim, A. Aziz, and A. Rahmat, “Enhanced liquid-phase sintering of W-Cu composites by liquid infiltration,” *Int. J. Refract. Met. Hard Mater.*, vol. 43, pp. 222–226, 2014.

[27] A. R. Kennedy, J. D. Wood, and B. M. Weager, “The wetting and spontaneous infiltration of ceramics by molten copper,” *J. Mater. Sci.*, vol. 35, no. 12, pp. 2909–2912, 2000.

[28] G. P. Martins, D. L. Olson, and G. R. Edwards, “Modeling of infiltration kinetics for liquid metal processing of composites,” *Metall. Trans. B*, vol. 19, no. 1, pp. 95–101, 1988.

[29] A. Chrysanthou and G. Erbaccio, “Production of copper-matrix composites by in situ processing,” *J. Mater. Sci.*, vol. 30, no. 24, pp. 6339–6344, 1995.

[30] V. L. Silva, C. M. Fernandes, and A. M. R. Senos, “Copper wettability on tungsten carbide surfaces,” *Ceram. Int.*, vol. 42, no. 1, pp. 1191–1196, 2016.

[31] J. R. Welty, C. E. Wicks, R. E. Wilson, and G. L. Rorrer, *Fundamentals of Momentum, Heat, and Mass Transfer*. 2008.

[32] S. Nawka, T. Schubert, A. Brendel, A. Zivelonghi, J. You, and B. Kieback, “Synthesis, Characterization and FEM-simulation of W / CuCrZr- Composites for Extreme Thermal Applications,” *Proc. World Powder Metall. Congr. Exhib.*, 2010.

[33] V. . Blank *et al.*, “A new carbon structure formed at MeV neutron irradiation of diamond: structural and spectroscopic investigations,” *Diam. Relat. Mater.*, vol. 8, no. 7, pp. 1285–1290, 1999.

[34] Y. X. Q Li, S Zhao, Z Sun, “Development and application of W/Cu flat-type plasma facing components at ASIPP,” *Phys. Scr.*, vol. 2017, no. T170, 2017.

[35] I. Reimanis, Ed., “Functionally Graded Materials,” in *The Handbook of Advanced Materials: Enabling New Designs*, John Wiley & Sons, Inc., 2004, pp. 466–467.

[36] H. R. Kieback, A. Neubrand, “Processing techniques for functionally graded materials,” *Mater. Sci. Eng. A*, vol. 362, no. 1–2, pp. 81–106, 2003.

[37] W. Callister and D. Rethwisch, “Composites,” in *Materials science and Engineering, an introduction*, 7th ed., Wiley, 1940, pp. 578–605.

[38] D. B. Miracle, “Metal matrix composites - From science to technological significance,” *Compos. Sci. Technol.*, vol. 65, pp. 2526–2540, 2005.

[39] J. P. Stobrawa, Z. M. Rdazawski, W. Głuchowski, and J. Domagała-Dubiel, “Nanocrystalline copper based microcomposites,” *J. Achievments Mater. Manuf. Eng.*, vol. 54, no. 1, pp. 49–57, 2012.

[40] A. M. Evans, C. San Marchi, “Metal Matrix Composites,” in *Metal Matrix Composites in Industry*, Springer, Boston, MA, 2003, pp. 9–38.

[41] R. Faria, M. Rodrigues, I. Esquef, H. Vargas, and M. Filgueira, “On the thermal characterization of a HPHT sintered WC – 15 % wt Co hardmetal alloy,” *Int. J. Refract. Metals Hard Mater.*, vol. 23, pp. 115–118, 2005.

[42] J. Li, H. Zhang, Y. Zhang, Z. Che, and X. Wang, “Microstructure and thermal conductivity of Cu/diamond composites with Ti-coated diamond particles produced by gas pressure infiltration,” *J. Alloys Compd.*, vol. 647, pp. 941–946, 2015.

[43] R. M. German, P. Suri, and S. J. Park, “Review: Liquid phase sintering,” *J. Mater. Sci.*, vol. 44, no. 1, pp. 1–39, 2009.

[44] L. Duan, W. Lin, J. Wang, and G. Yang, “Thermal properties of W – Cu composites manufactured by copper infiltration into tungsten fiber matrix,” *Int . J. Refract. Met. Hard Mater.*, vol. 46, pp. 96–100, 2014.

[45] J. L. Johnson, “Activated liquid phase sintering of W – Cu and Mo – Cu,” *Int . J. Refract. Met. Hard Mater.*, vol. 53 part B, pp. 80–86, 2015.

[46] S. A. Miller and P. R. Roberts, “Forging and Hot Pressing,” *ASM Handbook, Vol 7 Powder Met. Technol. Appl.*, vol. 7, pp. 97–101, 1990.

[47] A. Zivelonghi, A. Brendel, S. Lindig, S. Nawka, B. Kieback, and J. H. You, “Microstructure-based analysis of thermal- and mechanical behaviors of W/CuCrZr composites and porous W coating,” *J. Nucl. Mater.*, vol. 417, no. 1–3, pp. 536–539, 2011.

[48] “OOF: Finite Element Analysis of Microstructures,” *National Institute of Standards and Technology*, 2017. [Online]. Available: https://www.ctcms.nist.gov/oof/oof2/index.html. [Accessed: 20-Sep-2017].

[49] M. A. Sheikh, S. C. Taylor, D. R. Hayhurst, and R. Taylor, “Measurement of thermal diffusivity of isotropic materials using a laser flash method and its validation by finite element analysis,” *Mater. Sci.*, vol. 33, pp. 1536–1550, 2000.

[50] M. Yusoff and Z. Hussain, “Effect of Sintering Parameters on Microstructure and Properties of Mechanically Alloyed Copper-Tungsten Carbide Composite,” *Int. J. Mater. Mech. Manuf.*, vol. 1, no. 3, pp. 283–286, 2013.

[51] M. Roosta, H. Baharvandi, and H. Abdizade, “An experimental investigation on the fabrication of W-Cu composite through hot-press,” *Int. J. Ind. Chem.*, vol. 3, no. 1, p. 10, 2012.

[52] J. Alami, S. Bolz, and K. Sarakinos, “High power pulsed magnetron sputtering: Fundamentals and applications,” *J. Alloys Compd.*, vol. 483, no. 1–2, pp. 30–534, 2009.

[53] J. A. Thornton, “Influence of apparatus geometry and deposition conditions on the structure and topography of thick sputtered coatings,” *J. Vac. Sci. Technol.*, vol. 11, no. 4, pp. 666–670, 1974.

[54] J. Goldstein *et al.*, *Scanning Electron Microscopy and X-Ray Microanalysis*, 3rd ed. 2003.

[55] W. Barker and J. Fournelle, “X-ray Compositional MicroAnalysis: EDS and WDS,” in *Electron Microscopy: Theory and Practice*, 1st ed., University of Wisconsin-Madison, 1996.

[56] W. Callister and D. Rethwisch, “Mechanical Properties of Metals,” in *Materials science and Engineering, an introduction*, 7th ed., Willer, 1949, pp. 155–160.

[57] “Hardness and Microhardness Testing,” *Cranfield University*, 2017. [Online]. Available: https://www.cranfield.ac.uk/facilities/hardness-and-microhardness-testing.

[58] Y. Long, J. Chen, Y. G. Liu, F. D. Nie, and J. S. Sun, “A direct method to calculate thermal conductivity and its application in solid HMX,” *J. Phys. Condens. Matter*, vol. 22, pp. 1–7, 2010.

[59] E. Kaufmann, *Characterization of Materials*, 1st ed. New Jersey: John Wiley & Sons, Inc., 2003.

[60] A. P. F. Albers, T. A. G. Restivo, L. Pagano, and J. B. Baldo, “Effect of testing conditions on the laser flash thermal diffusivity measurements of ceramics,” *Thermochim. Acta*, vol. 370, no. 1–2, pp. 111–118, 2001.

[61] C. N. C. U. Maldrocar, “Measurement of thermal conductivity at high temperatures,” vol. 24, pp. 551–580, 1992.

[62] M. Reading, A. Luget, and R. Wilson, “Modulated differential scanning calorimetry,” *Thermochim. Acta*, vol. 238, no. C, pp. 295–307, 1994.

[63] R. R. Jr., “Principles of Powder Diffraction,” in *Modern Powder Diffraction*, D. Bish and J. Post, Eds. Mineralogical Society of America, 1989, pp. 1–18.

[64] C. D. Technology, “Finite Element Analysis – Predicting the Real World.” [Online]. Available: http://www.cambridge-dt.com/finite-element-analysis-predicting-the-real-world/. [Accessed: 04-Sep-2017].

[65] Struers, “Metallographic preparation of copper and copper alloys,” in *Application Notes*, 2011, p. 49.

[66] CSC - IT Center for Science, “Elmer.” [Online]. Available: https://www.csc.fi/web/elmer/elmer. [Accessed: 13-Feb-2017].

[67] H. K. Hieu and N. N. Ha, “High pressure melting curves of silver, gold and copper,” *AIP Adv.*, vol. 3, no. 11, pp. 112125–8, 2013.

[68] D. W. Rice, P. Peterson, E. B. Rigby, P. B. P. Phipps, R. J. Cappell, and R. Tremoureux, “Atmospheric Corrosion of Copper and Silver,” *J. Electrochem. Soc.*, vol. 128, no. 2, pp. 275–284, 1981.

[69] V. M. Horrigan, “Solubility of oxygen in solid copper,” *Metall. Trans. A*, vol. 8A, pp. 785–787, 1977.

[70] *Modern Developments in Powder Metallurgy*. Springer US, 1971.

[71] J. H. You, A. Brendel, S. Nawka, T. Schubert, and B. Kieback, “Thermal and mechanical properties of infiltrated W/CuCrZr composite materials for functionally graded heat sink application,” *J. Nucl. Mater.*, vol. 438, no. 1–3, pp. 1–6, 2013.

[72] P. H. Sidles and G. C. Danielson, “Thermal Diffusivity of Metals at High Temperatures,” *J. Appl. Phys.*, vol. 25, no. 1, pp. 58–66, 1954.

[73] J. E. Jensen, W. A. Tuttle, R. B. Stewart, H. Brechna, and A. G. Prodell, “Section XV,” in *Cryogenic Data Notebook*, vol. I, 1980.

[74] M. Akoshima, Y. Yamashita, Y. Hishinuma, T. Tanaka, and T. Muroga, “Thermal Diffusivity Measurements

of Candidate Ceramic Materials for Shielding Blankets," *ECTP2014 - 20th European Conference on Thermophysical Properties*. 2014.

[75] M. Fujitsuka, B. Tsuchiya, I. Mutoh, T. Tanabe, and T. Shikama, "Effect of neutron irradiation on thermal diffusivity of tungsten-rhenium alloys," *J. Nucl. Mater.*, vol. 283–287, pp. 1148–1151, 2000.

[76] M. Rohde, F. Hemberger, and T. Bauer, "Intercomparison of thermal diffusivity measurements on CuCrZr and PMMA," *High Temp. Press.*, vol. 42, no. 6, pp. 469–474, 2013.

[77] P. Miranzo *et al.*, "Thermal conductivity enhancement in cutting tools by chemical vapor deposition diamond coating," *Diam. Relat. Mater.*, vol. 11, pp. 703–707, 2002.

[78] "Advanced Energy Technology Group Center for Energy Research - Pure Copper," 2017. [Online]. Available: http://www-ferp.ucsd.edu/LIB/PROPS/PANOS/cu.html. [Accessed: 28-May-2017].

[79] Y. Birol, "Thermal fatigue testing of CuCrZr alloy for high temperature tooling applications," *J. Mater. Sci.*, vol. 45, no. 16, pp. 4501–4506, 2010.

[80] "Efunda - Thermal Conductivity: Tungsten," 2017. [Online]. Available: http://www.efunda.com/materials/elements/TC_Table.cfm?Element_ID=W. [Accessed: 28-May-2017].

[81] SANDVIK Hard Materials, *Understanding Cemented Carbide*. .

[82] H. Wang, T. Webb, and J. W. Bitler, "Study of thermal expansion and thermal conductivity of cemented WC-Co composite," *Int. J. Refract. Met. Hard Mater.*, pp. 1–8, 2014.

[83] S. Cariou, F. J. Ulm, and L. Dormieux, "Hardness-packing density scaling relations for cohesive-frictional porous materials," *J. Mech. Phys. Solids*, vol. 56, no. 3, pp. 924–952, 2008.

[84] J. Khosravi, M. Givi, M. Barmouz, and A. Rahi, "Microstructural, mechanical, and thermophysical characterization of Cu/WC composite layers fabricated via friction stir processing," *Int. J. Addict. Manuf. Technol.*, vol. 74, no. 5–8, pp. 1087–1096, 2014.

[85] J. Martín-Vaquero and J. Vigo-Aguiar, "Adapted BDF algorithms: Higher-order methods and their stability," *J. Sci. Comput.*, vol. 32, no. 2, pp. 287–313, 2007.

[86] J. Butcher, "Runge-Kutta Methods," in *Numerical Methods for Ordinary Differential Equations*, John Wiley & Sons, Inc., 2003, p. 440.

[87] V. Marra, "On Solvers: Multigrid Methods," 2013. [Online]. Available: https://www.comsol.com/blogs/on-solvers-multigrid-methods/.

[88] O. Y. Milyukova and V. F. Tishkin, "A Multigrid Method for a Heat Equation with Discontinuous Coefficients with a Special Choice of Grids," *Mat. Model.*, vol. 27, no. 9, pp. 17–32, 2015.

[89] D. A. Nield and A. Bejan, "Heat Transfer Through a Porous Medium," in *Convection in Porous Media*, 4th ed., 2013, pp. 31–46.

[90] A. Kromka, J. Janík, A. Satka, and J. Pavlov, "Investigation of Carburisation of Tungsten-Carbide Formation By Hot-Filament CVD Technique," *Acta Phys. Slovaca*, vol. 51, no. 6, pp. 359–368, 2001.

[91] G. Schmid and C. Eisenmenger-Sittner, "A method for uniformly coating powdery substrates by magnetron sputtering," *Surf. Coatings Technol.*, vol. 236, pp. 353–360, 2013.

[92] G. Petzow and W. Kaysser, "Basic mechanisms of liquid phase sintering," *Sintered metal–ceramic composites*. pp. 51–70, 1984.

Annex

Annex A: Mass calculation of cermets with sputtered WC particles

Objective: to deal with the calculation of the mass of copper incorporated in a sputtered WC particle. All the considered measures are the mean value obtained by SEM imaging.

The singular covered particles were mounted in a sample, to analyse their coating characteristics. SEM images, in Figure a.1 reveal that the particles do not have all the surface covered by the sputtered copper. The considered thickness of the cover is the average of 20 measures taken in a dozen of particles, the ones possible to get this measure. The obtained values and other derivations, to achieve the copper volume corresponding to the coat are presented, are posted in Table a.1.

Figure a.1. SEM images of some of the covered particles used to estimate the cover thickness

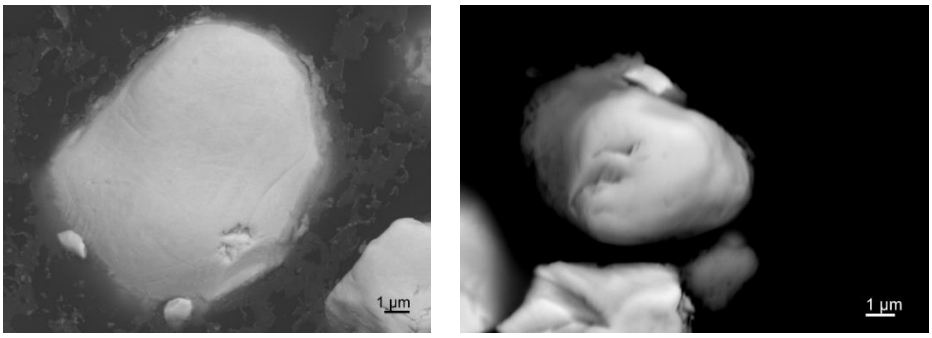

Table a.1 Parameters used in the equations with the respective name, symbol, unit and value

Symbol	Unit	Definition	Value
e	cm	Layer thickness	5.61×10^{-5}
$Ø_p$	cm	Admitted WC particle diameter	1.158×10^{-3}
r_p	cm	Admitted WC particle radius	5.79×10^{-4}
V_p	cm^3	Volume of the particle	8.13×10^{-10}
V_{p+c}	cm^3	Volume of the particle and cover layer	1.073×10^{-9}
φ	-	Volume fraction	0.75754

- Average copper volume of the coating layer, of one WC particle

To determine the amount of volume that copper occupies, in average, per particle, a volume ratio φ was calculated, $\varphi = \frac{V_p}{V_{p+c}}$, where V_p is the volume of the particle and V_{p+c} the volume of the coated particle:

$$V_p = {}^4/_3\,\pi {r_p}^3 \tag{37}$$

$$V_{p+c} = {}^4/_3\,\pi (r_p + e)^3 \tag{38}$$

The resulting ratio is

$$\varphi = \frac{V_p}{V_{p+c}} = 0.76 \tag{39}$$

In this way, an average particle increases $(1 - 0.76 = 0.242)$ 24.2% of its volume after sputtering.

Annex B: Thermal diffusivities

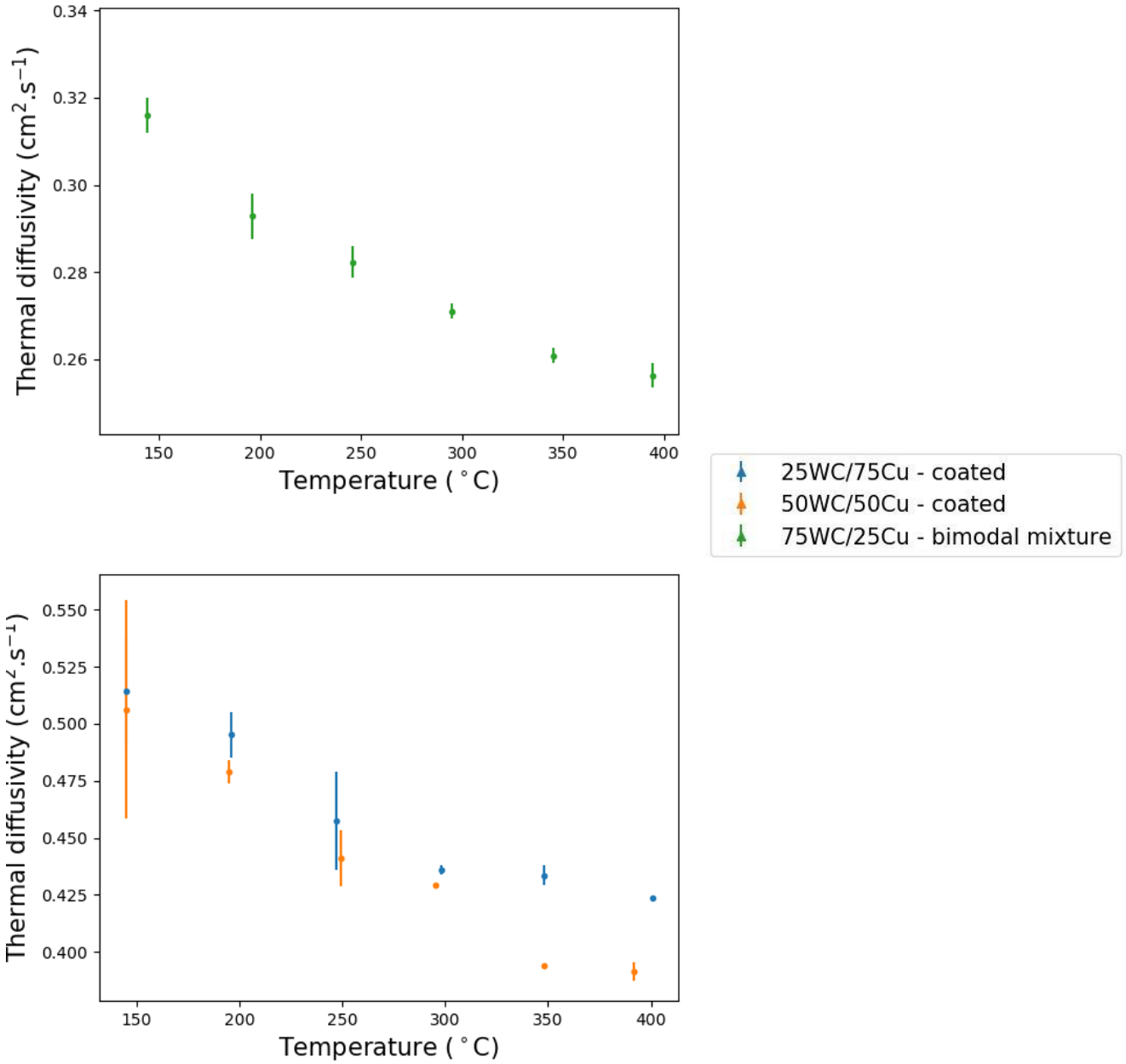

Annex C: Mesh file for the 3D model

```
Coordinate System = Cartesian 3D

Subcell Divisions = 1 1 1

Subcell Sizes 1 = 10e-3
Subcell Sizes 2 = 10e-3
Subcell Sizes 2 = 2.5e-3

Subcell Limits 1 = -5e-3 5e-3
Subcell Limits 2 = -5e-3 5e-3
Subcell Limits 3 = 0 2.5e-3

Material Structure in 3D
  1
End

Materials Interval = 1
Boundary Definitions
! type  out int double  of the boundaries
  1 -4 1 1
  2 -2 1 1
  3 0 -9 1
End

Numbering = Vertical
Element Degree = 1
Surface Elements = 500
Reference Density = 5e-4
Coordinate Ratios = 1 0.25
!CR - refinement of mesh in z direction

Geometry Mappings
!GM - mesh relaxing distance- choose from the centre to the radius
! mode line limits(2) Np params(Np)
    4    0  7.1e-3  7.1e-3 2 0 5e-3
End
```

Annex D: Solver input file for the 3D model

```
Header
  CHECK KEYWORDS Warn
  Mesh DB "." "."
  Include Path ""
  Results Directory "bdf5"
End

Simulation
  Max Output Level = 5
  Coordinate System = Cartesian
  Coordinate Mapping(3) = 1 2 3
  Simulation Type = Transient
  Steady State Max Iterations = 3
  Output Intervals = 5
  Timestepping Method = BDF
  BDF Order = 5
  Timestep intervals = 150
  Timestep Sizes = 0.001
  Solver Input File = case.sif
  Post File = case.vtu
End

Constants
  Gravity(4) = 0 -1 0 9.82
  Stefan Boltzmann = 5.67e-08
  Permittivity of Vacuum = 8.8542e-12
  Boltzmann Constant = 1.3807e-23
  Unit Charge = 1.602e-19
End

Body 1
  Target Bodies(1) = 1
  Name = "Body 1"
  Equation = 1
  Material = 1
  Initial condition = 1
End

Solver 1
  Equation = Heat Equation
  Procedure = "HeatSolve" "HeatSolver"
  Variable = Temperature
  Exec Solver = Always
  Stabilize = True
  Bubbles = False
  Lumped Mass Matrix = False
  Optimize Bandwidth = True
  Steady State Convergence Tolerance = 1.0e-5
  Nonlinear System Convergence Tolerance = 1.0e-7
  Nonlinear System Max Iterations = 20
  Nonlinear System Newton After Iterations = 3
  Nonlinear System Newton After Tolerance = 1.0e-3
  Nonlinear System Relaxation Factor = 1
  Linear System Solver = Iterative
```

```
  Linear System Iterative Method = BiCGStab
  Linear System Max Iterations = 500
  Linear System Convergence Tolerance = 1.0e-10
  BiCGstabl polynomial degree = 2
  Linear System Preconditioning = ILU0
  Linear System ILUT Tolerance = 1.0e-3
  Linear System Abort Not Converged = True
  Linear System Residual Output = 1
  Linear System Precondition Recompute = 1
End

Equation 1
  Name = "Heat Equation"
  Active Solvers(1) = 1
End

Material 1
  Name = "WC-Cu experimental"
  Heat expansion Coefficient = 4e-6
  Heat Conductivity = 83.7
  Heat Capacity = 247.9
  Density = 13186.058
End

Initial Condition 1
  Name = "T initial"
  Temperature = 667
End

Boundary Condition 1
  Target Boundaries(1) = 2
  Name = "upper surface"
  Heat Flux = Variable Time; Real MATC "if (tx<0.002) 4.46e8; else
0"
End

Boundary Condition 2
  Target Boundaries(3) = 3 4 5
  Name = "rear lateral interior"
  Heat Flux = 0
End
```

Annex E: Mesh file for the 2D dense model

```
***** ElmerGrid input file *****
Version = 210903
Coordinate System = Cartesian 2D

Subcell Divisions = 20 10

Subcell Sizes 1 = 2.5e-4 2.5e-4 2.5e-4 2.5e-4 2.5e-4 2.5e-4 2.5e-4
2.5e-4 2.5e-4 2.5e-4 2.5e-4 2.5e-4 2.5e-4 2.5e-4 2.5e-4 2.5e-4 2.5e-
4 2.5e-4 2.5e-4 2.5e-4
Subcell Sizes 2 = 2.5e-4 2.5e-4 2.5e-4 2.5e-4 2.5e-4 2.5e-4 2.5e-4
2.5e-4 2.5e-4 2.5e-4

Material Structure in 2D
  1 1 1 1 1 1 1 1 1 1 1 1 1 1 1 1 1 1 1 1
  1 1 1 1 1 1 1 1 1 1 1 1 1 1 1 1 1 1 1 1
  1 1 1 1 1 1 1 1 1 1 1 1 1 1 1 1 1 1 1 1
  1 1 1 1 1 1 1 1 1 1 1 1 1 1 1 1 1 1 1 1
  1 1 1 1 1 1 1 1 1 1 1 1 1 1 1 1 1 1 1 1
  1 1 1 1 1 1 1 1 1 1 1 1 1 1 1 1 1 1 1 1
  1 1 1 1 1 1 1 1 1 1 1 1 1 1 1 1 1 1 1 1
  1 1 1 1 1 1 1 1 1 1 1 1 1 1 1 1 1 1 1 1
  1 1 1 1 1 1 1 1 1 1 1 1 1 1 1 1 1 1 1 1
  1 1 1 1 1 1 1 1 1 1 1 1 1 1 1 1 1 1 1 1

End

Materials Interval = 1 1
Boundary Definitions
! type  out int double  of the boundaries
  2 -3 1 1
  3 -4 1 1
  5 -2 1 1
  4 -1 1 1

End

Numbering = Vertical
Element Degree = 1
Surface Elements = 1000
Reference Density = 2e-1
Coordinate Ratios = 1 1
```

Annex F: Mesh file for the 2D porous model

```
***** ElmerGrid input file *****
Version = 210903

Coordinate System = Cartesian 2D
Subcell Divisions = 20 10
Subcell Sizes 1 = 2.5 2.5 2.5 2.5 2.5 2.5 2.5 2.5 2.5 2.5 2.5 2.5
2.5 2.5 2.5 2.5 2.5 2.5 2.5 2.5
Subcell Sizes 2 = 2.5 2.5 2.5 2.5 2.5 2.5 2.5 2.5 2.5 2.5

Material Structure in 2D
  1 1 1 1 1 1 1 1 1 1 1 1 1 1 1 1 1 1 1 1
  1 1 1 1 1 1 1 1 1 2 1 1 1 1 1 1 1 1 2 1
  1 1 1 2 1 1 1 1 1 1 1 1 1 2 1 1 1 1 1 1
  1 1 1 1 1 1 1 1 1 1 1 1 1 1 1 1 1 1 1 1
  1 1 1 1 1 1 1 2 1 1 1 1 1 1 1 1 1 1 1 1
  1 1 1 1 1 1 1 1 1 1 1 2 1 1 1 1 1 1 1 1
  1 2 1 1 1 1 1 1 1 1 1 1 1 1 1 1 1 1 1 1
  1 1 1 1 1 2 1 1 1 1 1 1 1 1 2 1 1 1 1 1
  1 1 1 1 1 1 1 1 1 1 2 1 1 1 1 1 1 1 1 1
  1 1 1 1 1 1 1 1 1 1 1 1 1 1 1 1 1 1 1 1

End


Materials Interval = 1 2
Boundary Definitions
! type  out int double  of the boundaries
  1 2 1 1
  2 -3 1 1
  3 -4 1 1
  5 -2 1 1
  4 -1 1 1

End

Numbering = Vertical
Element Degree = 1
Surface Elements = 1000
Reference Density = 2e-1
Coordinate Ratios = 1 1
```

Annex G: Solver input file for the 2D porous model

```
Header
  CHECK KEYWORDS Warn
  Mesh DB "." "."
  Include Path ""
  Results Directory "bdf5"
End

Simulation
  Max Output Level = 5
  Coordinate System = Cartesian
  Coordinate Mapping(3) = 1 2 3
  Simulation Type = Transient
  Steady State Max Iterations = 3
  Output Intervals = 5
  Timestepping Method = BDF
  BDF Order = 5
  Timestep intervals = 150
  Timestep Sizes = 0.001
  Solver Input File = case.sif
  Post File = case.vtu
Coordinate Scaling = 0.0001
End

Constants
  Gravity(4) = 0 -1 0 9.82
  Stefan Boltzmann = 5.67e-08
  Permittivity of Vacuum = 8.8542e-12
  Boltzmann Constant = 1.3807e-23
  Unit Charge = 1.602e-19
End

Body 1
  Target Bodies(1) = 1
  Name = "Body 1"
  Equation = 1
  Material = 1
  Initial condition = 1
End

Body 2
  Target Bodies(1) = 2
  Name = "Body 2"
  Equation = 1
  Material = 2
  Initial condition = 1
End

Solver 1
  Equation = Heat Equation
  Procedure = "HeatSolve" "HeatSolver"
  Variable = Temperature
  Exec Solver = Always
  Stabilize = True
  Bubbles = False
```

```
  Lumped Mass Matrix = False
  Optimize Bandwidth = True
  Steady State Convergence Tolerance = 1.0e-5
  Nonlinear System Convergence Tolerance = 1.0e-7
  Nonlinear System Max Iterations = 20
  Nonlinear System Newton After Iterations = 3
  Nonlinear System Newton After Tolerance = 1.0e-3
  Nonlinear System Relaxation Factor = 1
  Linear System Solver = Iterative
  Linear System Iterative Method = BiCGStab
  Linear System Max Iterations = 500
  Linear System Convergence Tolerance = 1.0e-10
  BiCGstabl polynomial degree = 2
  Linear System Preconditioning = Diagonal
  Linear System ILUT Tolerance = 1.0e-3
  Linear System Abort Not Converged = False
  Linear System Residual Output = 1
  Linear System Precondition Recompute = 1
End

Equation 1
  Name = "heat equation"
  Active Solvers(1) = 1
End

Material 1
  Name = "WC-Cu experimental"
  Heat expansion Coefficient = 4e-6
  Heat Conductivity = 106.85
  Heat Capacity = 316.2
  Density = 13190
End

Material 2
  Name = "Air (T=400C)"
  Viscosity = 62.53e-6
  Heat expansion Coefficient = 1.49e-3
  Heat Conductivity = 0.0515
  Relative Permittivity = 1.00059
  Sound speed = 343.0
  Heat Capacity = 1068.0
  Density = 0.524
End

Initial Condition 1
  Name = "Initial T"
  Temperature = 667
End
Boundary Condition 1
  Target Boundaries(1) = 2
  Name = "upper"
  Heat Flux = Variable Time; Real MATC "if (tx<0.002) 4.46e8; else
0"
End
```